Towards Multi-Channel Inversion of Electromagnetic Sea Ice Surveys

Anne Irvin

A dissertation submited to the faculty of graduate studies in partial fulfillment of the requirements for the degree of Doctor of Philosophy

GRADUATE PROGRAM IN EARTH & SPACE SCIENCE AND ENGINEERING,

LASSONDE SCHOOL OF ENGINEERING,

YORK UNIVERSITY

TORONTO, ONTARIO

November 2018

Abstract

Sea ice is a crucial parameter in climate research as it plays an important role in the interaction between oceans and the atmosphere in polar regions. It is considered a climate indicator and it is critical to observe its development in the context of climate change. While sea ice extent provides a picture of the surface conditions of the ice, ice thickness information is needed to fully understand the overall sea ice conditions.

Frequency domain electromagnetic (EM) induction sounding is a non-invasive remote sensing method to measure sea ice thickness changes on the regional scale as well as provide a means to calibrate and validate satellite ice thickness data. This PhD thesis aims to advance the analysis of airborne and ground based sea ice thickness measurements from frequency domain EM sounding by improving ice thickness retrievals with concurrent use of Inphase and Quadrature instrument responses in a numerical inversion for multi- and single-frequency devices. The developed methods and algorithms include the forward modelling code and GUI ODFEM (One Dimensional Frequency domain Electromagnetic Model) to simulate the EM instrument responses for Inphase and Quadrature for different instrument and model settings. Furthermore, a brute force inversion method was established which can be used in combination with the 1D forward models created with ODFEM to invert single- and multi-frequency EM data into multi-layer ice thicknesses and ice conductivities. The performance of the developed brute force inversion algorithm is demonstrated on a variety of field data sets including an approach on how to resolve the thickness of a slush layer and its conductivity

(wet saline snow) using a five-layer-model and the data of 3 measurement frequencies. Furthermore, how to measure the thickness and determine the conductivity of a sub-ice-platelet-layer commonly observed in Antarctica is demonstrated using an inversion of the two channel output of a single-frequency instrument (Inphase and Quadrature) in combination with in situ drill hole measurements.

The methods and algorithms developed within this thesis provide new and more extended applications for a variety of EM devices for ground based and airborne ice thickness surveys.

I dedicate this thesis to my parents and my husband. For their relentless support in anything I do and their belief that I can accomplish anything.

Acknowledgments

I would like to thank my supervisor Christian Haas for giving me the opportunity to work in polar research and to realise this thesis with his help and guidance. I am thankful for the many oportunities to do research in the field in the Arctic and the life experiences gained from them.

Thanks to John Lobach for taking me under his wing in the beginning and teaching me some of his trade.

I would like to thank my research group at York University. Special thanks to Alec Casey for always having an open ear and our endless discussions as well as for the great times and adventures we had during hours spent surveying sea ice in the Arctic.

Thanks to Marzena Marosz-Wantuch for her effort on collecting the vast amount of ground based EM data that was used for the slush analysis.

I would like to also thank Wolfgang Rack and Christian Haas for the initial idea and data provided for the sub-ice-platelet-layer study.

Thanks to my family and friends that always showed support and believed in me and what I do.

Finally I'd like to thank all the people I haven't mentioned by name but were involved directly or indirectly in me completing this work be it during field campaigns or through discussions.

Contents

List of Tables

List of Figures

1. Introduction

1.1. Motivation

Faced with a global rise in temperatures and the inherent glacier retreat and sea level rise, it is evident that the understanding of processes, feedbacks and effects of global climate change is still limited. The most distinct effects of a global temperature rise can be seen in the polar regions of the Earth. As a result, sea ice has become a crucial parameter in climate research as it plays an important role for the interaction of oceans and atmosphere in the polar regions. While it is subject to strong seasonal changes, it covers on average about 25 million square kilometers of the Earth, which is 2.5 times the area of Canada. When sea ice forms, it forms a relatively thin cover of the ocean surface with thicknesses ranging mostly between a few decimeters to a few meters. Its thickness is a result of the surface energy balance which is dependent on air temperature, radiation, winds and ocean heat flux. When sea ice melts its bright surface gives way to the dark ocean surface, thereby enhancing the absorption of solar radiation and subsequent warming of surface waters. This ice-albedo feedback combined with polar amplification in the form of other small perturbations within the ocean and the atmosphere and a change in the net radiation balance of the planet, can lead to significant changes in the extent or thickness of the polar ice cover and in turn can have a major influence on the state of the ocean and the atmosphere [Hall 2004; Perovich and Polashenski 2012]. Hence, sea ice is considered a climate indicator and it is critical

to observe its development in the context of climate change.

A change in ice conditions, like ice thickness or ice strength, can present a challenge or even hazard to marine operations including shipping and offshore oil and gas operations. They are therefore in need of near real-time information on sea ice extent, drift, ice type and ice thickness. The vast area covered by sea ice in the cryosphere can only be observed by using a combination of different remote sensing techniques, including satellites, and ground based and airborne surveys. The Intergovernmental Panel on Climate Change (IPCC) Fifth Assessment report [Stocker, 2014] discusses the importance of remote sensing for current sea ice research by highlighting five essential findings. These findings include that since 1979: Arctic sea ice extent decreased, Arctic perennial and multi-year-ice decreased, the period of surface melt on Arctic perennial ice lengthened, and Arctic sea ice thickness decreased [Haas et al., 2008; Laxon et al., 2013; NSIDC, 2017]. The observed decline in sea ice extent (see details in Chapter 2.1) is greater than predicted by general climate circulation models. Limited sea ice thickness information, especially in sub grid cell resolution, has been named a major challenge in sea ice modelling [Stroeve et al., 2007, 2012]. To improve parameterization and initialization of sea ice variables and sea ice thickness within these models, and to better understand the role of the sea ice cover in the climate system, continued observations of sea ice properties are imperative. To further improve the accuracy of those observations, and with it local and regional forecasting of sea ice and snow conditions, remote sensing techniques need to be further developed and improved.

1.2. Objective

While sea ice extent provides a picture of the surface conditions of the ice, ice thickness information is needed to fully understand the overall sea ice conditions. Ice thickness generally tends to respond more slowly to variations in climate forcing than sea ice extent and hence is considered a more 'stable' climate indicator [Meier, 2017]. Unlike sea ice concentration and extent which have been monitored with sufficient accuracy by satellites for more than 30 years, determining ice thickness is much more involved. Due to its relative thinness compared to other geological features, sea ice thickness measurements pose a challenge for any remote sensing technique.

The primary focus of this PhD research is to advance the analysis of airborne and ground based sea ice thickness measurements with frequency domain Electromagnetic (EM) sounding. It focuses on improvement of ice thickness retrievals by concurrent use of Inphase and Quadrature components and numerical inversion for multi- and single-frequency devices. A forward model code was developed to simulate the EM instrument responses for Inphase and Quadrature. In combination with a brute force inversion it can be used to calculate multi-layer ice thicknesses and ice conductivities for different EM devices in different configurations and for different applications. The resulting methods provide new and more extended applications for a variety of EM devices for ground based and airborne ice thickness surveys.

1.3. Thesis Overview

The thesis is comprised of 6 main chapters. The first chapter gives a general introduction into the motives and objectives of this thesis as well as a thesis overview.

Chapter 2 discusses sea ice and its relevance in the climate system. It further discusses the formation of sea ice, the different resulting ice types as well as differences between

sea ice in the Arctic and Antarctica and various direct and remote methods of measuring sea ice thickness.

Chapter 3 gives an overview of the theory behind frequency domain electromagnetic induction sounding including 1D model theory. In the following, the sensitivity limitations of different instrument setups are discussed and the instruments used within this thesis described.

In Chapter 4 the developed forward modelling code ODFEM is introduced and the functionality of the GUI surface described. Furthermore, Chapter 4 discusses the theory for the brute force inversion developed as part of this thesis and the validation method used to verify the quality of the inversion output.

Chapter 5 discusses the methods used to invert multi-frequency EM data. It first explains in detail how to calibrate instrument returns from the EM sounder EMP and its benefits for multi-frequency inversion. In the following, multi-frequency inversion for different ice types and different model types are being discussed, resulting in a method to resolve a wet conductive snow layer called slush using 3 frequencies and a five-layer-model.

In Chapter 6 describes the developed method to resolve a sub-ice platelet-layer (SIPL) and its conductivity using a single-frequency EM device in combination with in-situ ice thickness drill hole measurements is being described. Results include a map of regional SIPL distribution as well as an inter-annual comparison between the SIPL distribution in 2011 and 2013.

Finally, Chapter 7 provides a summary of the thesis and its results as well as an outlook for future work to be done.

2. Sea Ice

2.1. Sea Ice In The Climate System

Sea ice acts as an insulator between atmosphere and ocean, hindering the direct exchange of heat, moisture, gases, and aerosols as well as momentum between the two media. Sea ice formation and melt processes affect the heat and the salinity fluxes of the ocean and hence can affect deep ocean convection leading to large scaele implications for the oceanic thermohaline circulation.

The global sea ice area accounts for over a quarter of the total cryospheric surface on Earth, contributing to short feedback cycles that intensify existing natural variations and global warming. Sea ice with a thickness of over 10 cm reflects 70% of the incoming radiation due to a high albedo of 0.7, whereas the dark surface of the open ocean with a low albedo absorbs about 90% of the solar radiation [Perovich, 1996]. Accumulating snow on the sea ice cover can further increase the high surface albedo to 0.75-0.85 [Perovich, 1996] and therefore increase the cooling effect of the sea ice cover on the heat budget of the polar regions.

Strong increases in air temperature have been observed in the Arctic, with the 1995-2005 period being the warmest decade in the Arctic since the 17th century, with temperatures 2°C above the 1951-1990 average. Regions like Alaska and Western Canada show an even bigger increase of 3-4°C [Przybylak, 2007]. This increase of air temperature in

the Arctic not only causes a retreat of the ice and snow cover, but it is also amplified by the reduction in ice cover allowing the ocean surface to absorb more incoming solar radiation [Comiso and Parkinson, 2004]. Furthermore, it leads to higher temperatures and an acceleration of ice melt which in turn reduces sea ice albedo by formation of melt ponds as well as sedimentation of natural and anthropogenic aerosols during the summer season. Remote sensing results show an average summer albedo of 0.5-0.7 in the Arctic, with albedo decreasing by up to 50 % towards the ice edge in the Arctic marginal seas [Laine, 2004].The ice-albedo feedback is a positive climate feedback process where a change in sea ice or snow cover on land, glaciers or oceans, alters the albedo and therefore leads to the albedo reinforcing the initial sea ice area alteration. When atmospheric cooling increases the ice cover and in turn the albedo, less solar radiation gets absorbed by the surface resulting in further cooling. Conversely, warming reduces the ice area and with it the albedo, which results in more absorption of solar energy and in further warming of the surface [Curry et al., 1995]. Therefore, ice-albedo feedback plays a major role in diminishing the Arctic sea ice cover.

Satellite observations dating back to 1979 indicate considerable changes within the Arctic sea ice regime. Over the observation period of more than 25 years (1979-2006) the winter Arctic sea ice extent has decreased at a rate of around 3% per decade [Meier et al., 2007]. In recent years, observations show an even more dramatic reduction in regional ice cover. The Arctic summer minimum extent reached a record low in 2012 of 3.41 million square kilometers, an area coverage 44 % below the 1981-2010 average and 16% below the previous record in 2007. The summer ice extent in 2016 of 4.14 million square kilometers reached a statistical tie with the 2007 minimum [NSIDC, 2017]. Weather conditions in spring and summer can play a major role in the spatial distribution and extent of the ice in the summer and therefore contribute to a possible record low. However regardless of weather patterns, the Arctic summer ice shows a consistent downward trend in extent and thickness [Kwok and Rothrock, 2009; Laxon

et al., 2013; NSIDC, 2017].

Recent results in the Arctic show a loss of 15.1% in multi-year-ice (MYI) extend per decade, which is faster than the overall decrease in sea ice extent [study period 1981-2011, Comiso, 2012]. Ice age data show that the oldest ice, of over 4 years in age, comprised 57% of the Arctic Ocean's winter ice cover in 1987 and that by 2012 most of that old part of the ice cover of the Arctic was gone [Maslanik et al., 2011]. Figure 2.1.1 shows the extreme changes in sea ice age between 1985 and 2017 and the small amount of old ice left in the Arctic today.

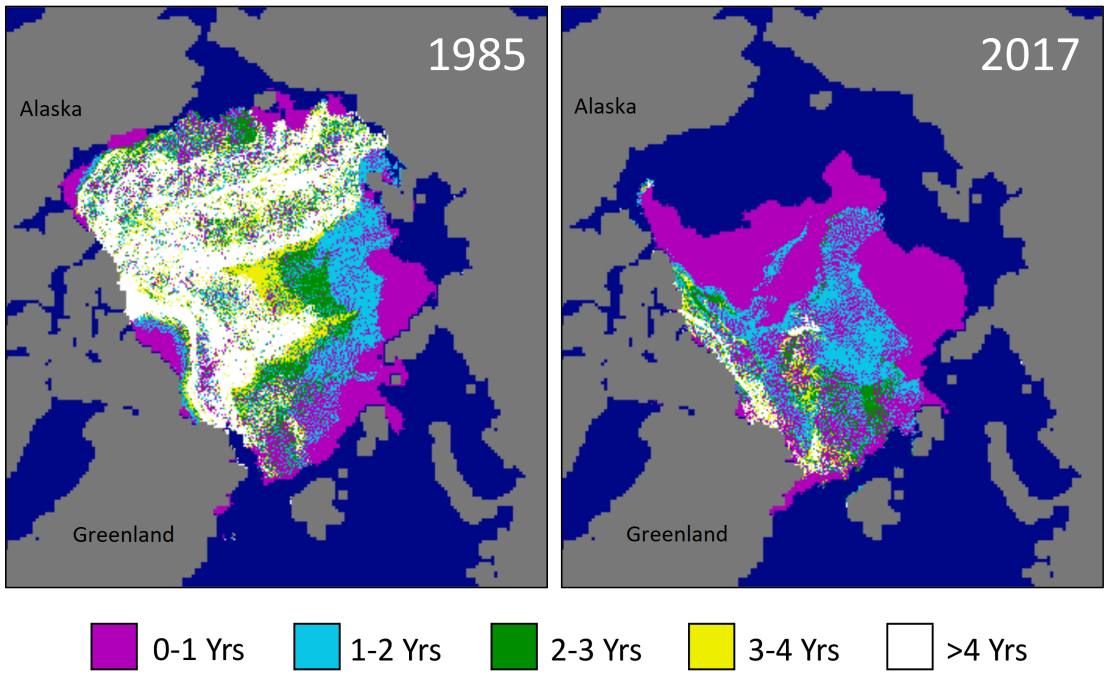

Figure 2.1.1.: Sea ice age distribution at the annual minimum extent in the Arctic for 1985 (left) and 2017 (right) [Tschudi et al., 2016].

Most of the loss of old ice in the Arctic is attributed to increased ice motion due to increased melt and with it, advection out of the Arctic through Fram Strait and the Canadian Archipelago. The old ice is not being replenished because less first-year ice (FYI) is able to survive the summer season. Furthermore, in situ melting, due to warmer ocean waters and increased solar heating of the ocean in the summer, has increased the

loss of MYI in in recent years in the Arctic, especially in the Beaufort and Chukchi seas [Steele et al., 2010; Krishfield et al., 2014]. The loss in sea ice extent in the Arctic is expected to have a significant impact on the ecosystem, including a loss in habitat for ice related fauna such as polar bears and seals. Recent studies show that the impact of sea ice loss on primary producers might be greater and more important than previously assumed [Arrigo et al., 2010; Lange et al., 2017].

2.2. Sea Ice Formation

Sea ice starts forming when the upper ocean is cooled to the freezing point of $-1.8°C$ [Wadhams, 2000]. Due to overturning by wind, ice crystals, known as frazil ice, are kept in suspension until a surface layer of slush ice builds up. With freezing of the interstitial brine from the top downwards, surface slush consolidates into granular ice with randomly oriented crystals. Once the consolidated ice covers the ocean and separates it from the atmosphere, sea ice keeps growing through congelation growth forming columnar ice. Ions are rejected from the ice as the ice-water interface moves downwards into the melt and as a result a thin layer of increasing salinity builds up ahead of the advancing interface. Since the ice-water interface is at the freezing point and the freezing point decreases with increasing salinity, the drop in temperature due to higher salt concentration leads to heat flux from the ocean to the now colder interface. This results in a thin layer ahead of the interface that is cooled below the freezing point of the ocean with a slightly increased salinity, a constitutionally super-cooled layer [Weeks, 2010]. When the ice water interface protrudes into a super-cooled layer, ice growth is promoted due to heat transfer not only being conducted upwards away from the interface but also down into the super-cooled layer. Consequently, the growth pattern of the sea ice changes and ordered patterns of lamellar bulges forming so called columnar sea ice. Brine is trapped between the lammelae and 10 % to 40 % of the ions are retained in

the ice crystals at the bottom of the sea ice [Petrich and Eicken, 2010].

During the winter growth season, the salinity of sea ice constantly changes and is reduced by desalination processes like brine cell migration, brine expulsion, gravity drainage and flushing [Cox and Weeks, 1974], gravity drainage being the most prominent mechanism throughout the winter growth season [Wadhams, 2000]. It occurs when the hydro static pressure head in the brine cells forces the brine downwards draining through the ice using a system of interconnected brine cells in the form of tubes and channels. The pressure head is caused by the density gradient of brine inside the ice below the water surface. The more cold and saline brine near the top of the ice has a higher density than the less saline brine near the warmer bottom of the ice [Weeks, 2010]. During the melt season, when melt water percolates through the brine channels, so called flushing, sea ice can experience further desalination. Up to a quarter of the meltwater produced annually at the surface of the Arctic sea ice can be retained within the ice cover. Meltwater flushing is the most rapid and efficient brine drainage mechanism and leads to desalination throughout the ice and therefore results in a pronounced decrease in bulk salinity over the melt season. Since the mentioned desalination processes occur over time, new and young ice types usually have higher salinities than old ice.

The thickness of thermodynamically grown young sea ice, depends primarily on the surface energy balance, mostly determined by air temperature, radiation, winds, and ocean heat flux. With increasing thickness, the thermal gradient between the warm ocean and the cold atmosphere is reduced and results in a decrease in ice growth. Accumulating snow on the surface can increase that effect and further reduce the thermal gradient. Snow may however be transformed into snow ice with a higher thermal conductivity than snow through melt, flooding or precipitation [Weeks, 2010].

Due to its relative thinness of 0.3 m to 2 m, young FYI is subject to winds and ocean currents and consequentially also grows in thickness dynamically. In regions of convergent ice drift its movement creates rafting and ridging at the boundaries of ice floes and

leads to pressure ridges of piled ice blocks. Divergent motion results in openings in the ice, like leads and polynyas, producing new ice in turn. Figure 2.2.1 shows a summary of the dynamic processes involved in creating different forms of sea ice. By providing a mechanism for ice thickness growth even when thermodynamic growth stalls, deformation of sea ice accounts for the thickest ice observed in the polar oceans. In FYI pressure ridges, keel depth can exceed 10-20 m [Strub-Klein and Sudom, 2012]. Consequently, sea ice floes, in a given region, are composed of larger areas of thermodynamically grown level ice and regions of pressure ridges from deformation processes in between.

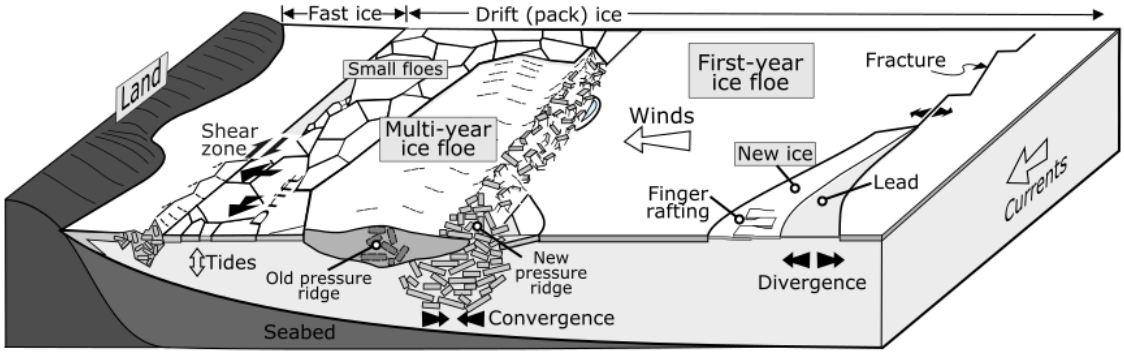

Figure 2.2.1.: Schematic overview of common dynamic sea ice features created through convergence, shear and divergence [adapted by Alec Casey from Lusilier, 2012].

Deformed ice is distinctly different from level ice with regards to mechanical strength, ocean and atmospheric drag, its characteristics as a biological habitat, and melt pond development. For example, ridges and snow drifts building up on their leeward side, provide shelter for seals and result in hunting territories for polar bears.

Over time, snow accumulates on ridges and rafted ice blocks and consolidates into thicker ice. Ice floes with these thicker ice features can survive the melting season and are referred to as multi-year-ice (MYI). MYI is characteristic for its rolling hummocky surface resulting from increased melt of inclined features devoid of snow, like ridges and ice blocks, as well as melt ponds [Weeks, 2010]. While MYI ages, every melt season contributes to a more distinguished hummocky topography that clearly differentiates it

from FYI as shown in Figure 2.2.2. Furthermore, these two ice types can be differentiated by other characteristics like salt content and its vertical distribution in the ice, crystal structure and layers, and total thickness. Additionally, MYI may have layers of snow-ice, superimposed ice, and sediment indicating former surfaces of the old ice.

Typically, sea ice is afloat and drifting and must be distinguished from stationary sea ice occurring along shore lines. Fast-ice is sea ice that is attached to the shore or shallow sea bottom areas and therefore not moving with normal pack ice. Fast-ice is often very flat and only deformed at grounding points. As can be seen in Figure 2.2.2, the edge of the fast ice forms an advanced coastline with its edge being characterized by intense deformation and shear or open water, leads, and polynyas.

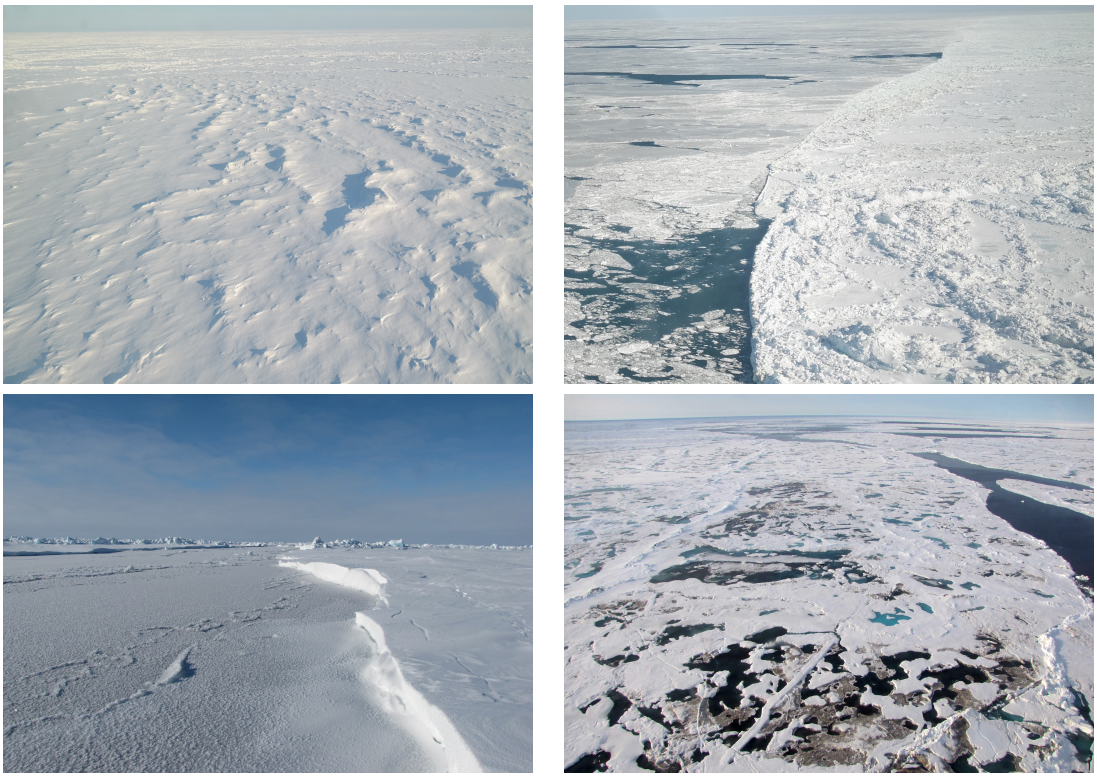

Figure 2.2.2.: Photos of different ice regimes. Upper Left: hummocky multi-year-ice flow; Upper Right: boundary between ridged landfast ice and young pack ice; Lower Left: refrozen polynia next to first-year ice floe; Lower Right: melt ponds and sedimentation on first-year ice. (photos by Anne Irvin)

2.2.1. Sea Ice in Antarctica

The Antarctic is the geographic opposite of the Arctic with a vast glaciated polar continent surrounded by the Southern Ocean. A major portion of this ocean becomes covered by seasonal sea ice ($\sim$16 million km^2) every year and only a fraction of it is covered by sea ice ($\sim$ 3 million km^2) that persists throughout all seasons [Stammerjohn and Maksym, 2017]. In contrast, the Arctic is a polar ocean and surrounded by continents and has double the amount of perennial sea ice cover and close to half as much seasonal sea ice. Antarctic sea ice encompasses lower latitudes of (60-75°S) and is subject to some of the highest winds and waves on Earth.

While congelation growth of sea ice with columnar texture usually dominates sea ice formation in the Arctic, the dynamic conditions of the marginal ice zone of the Southern Ocean result in the prevalence of granular ice types. Higher wind speeds and the effects of ocean swell, as well as a larger number of openings in the pack ice, favor the formations of frazil ice, which can constitute 60-80% of the total ice thickness. The dynamic ice growth of frazil ice in the uppermost meters of the ocean results in the predominance of pancake ice. Pancake ice forms through the accretion of clusters of frazil ice crystals into centimeter sized floes which in turn accrete into decimeter sized pans of ice. Those pans then bump and grind against one another and build a semi-consolidated ice cover composed of ice discs. The pancakes eventually consolidate through a combination of frazil growth and freezing of congelation ice, resulting in ice thicknesses of up to 0.5 m [Wadhams et al., 1987].

In contrast to the marginal ice zone, granular ice plays a minor role in the composition of landfast sea ice of Antarctica possibly due to less dynamic conditions near the Antarctic main land. For example contribution of granular ice to the McMurdo Sound fast ice have found to be under 3% [Jeffries et al., 1993; Gow et al., 1998] with the prevalent ice type being columnar ice [Gow et al., 1998; Smith et al., 2001]. In the vicinity of

ice shelves, which cover up to 44% of the Antarctic coastline [Drewry et al., 1982], ice shelf to ocean interactions promote the formation of platelet ice crystals within the water column. On the underside of ice shelves basal melting creates a body of cool and fresh water. Due to low density compared to the surrounding water it rises and with releasing pressure the freezing point rises resulting in supercooled water [Foldvik and Kvinge, 1974]. Ice crystals grow in the water column relieving supercooling resulting in increased local buoyancy and forming an Ice-Shelf-Water (ISW) plume [Smedsrud and Jenkins, 2004]. Freely drifting platelet ice crystals have been observed right below the base of the sea ice or suspended at depth of down to 250 m [Penrose et al., 1994]. The platelet crystals eventually settle and accumulate in a porous layer at the base of the sea ice, being incorporated into the ice cover while growing at the ice water interface. Such layers, referred to as the Sub-Ice-Platelet-Layer (SIPL), have been observed in the in the Ross Sea near the Hells Gate Ice Shelf [Tison et al., 2013], the Weddell Sea [Eicken and Lange, 1989] as well as McMurdo Sound [Gow et al., 1998; Leonard et al., 2006].

Thicknesses of the SIPL in McMurdo Sound have been observed to be several meters thick with values exceeding 7 m [Price et al., 2014]. Platelet ice increases the inherent thickness of sea ice [Smith et al., 2012; Hoppmann et al., 2015] . In winter, about 10 % of the ice thickness of FYI that forms in the vicinity of ice shelves can be atributed to heat loss to the ocean rather than the atmosphere [Gough et al., 2012]. Furthermore, platelet ice contributed to the thickness of the landfast MYI attached to the Mertz Glacier tongue, estimated to be 10 m to 55 m thick [Massom et al., 2010]. Langhorne et al. (2015) have shown that the inclusion of platelet ice into FYI is an annual process in response to export of supercooled water as part sub-ice shelf circulation pattern, indicating the volume of supercooled Ice Shelf Waters at the ocean surface as well as the amount of heat loss to the ocean. Chapter 6 provides further details of the SIPL and sea ice thickness distribution in McMurdo Sound in November 2011 and 2013.

2.3. Sea Ice Thickness Observation Methods

Ice thickness is defined as the distance between the underside of the ice or the ice-water interface and the ice surface or the snow-ice surface interface. Snow thickness is defined as the distance between the snow surface and the snow-ice interface. The sum of both ice thickness and snow thickness is referred to as the total thickness of the ice. Sea ice thickness observations also commonly include the measurement of snow freeboard and ice freeboard which is the height of the snow or ice surface above the water level, as well as the draft of the ice which is the depth of ice below the water level. These variables which can all be measured by using drill holes through the ice, give information about the total thickness of the ice while additionally providing opportunity for the calculation of the density of the ice and snow using the laws of isostasy [Eicken, 2009]. Drill-hole measurements include drilling a hole into the ice with either a motor-driven ice auger, a powerdrill-driven ice auger or a hot water drill. Thickness is measured with a tape measure that has a so called T-Anchor at its base.

There are a variety of different other methods to measure the thickness of sea ice, with different capabilities for measuring the above-mentioned variables. While drill-hole measurements are the method with the highest resolution and accuracy, drilling has high limits in feasibility when it comes to access to the ice, spatial coverage and its destructive nature. Drill holes can disturb the hydro static equilibrium and with that the thermodynamic balance in long-term ice thickness change studies. They can form artificial drainage channels during the melt season or cause flooding in areas where the snow load leads to negative freeboard with the snow-ice interface below the water level [Eicken, 2009]. Figure 2.3.1 shows the most important measurement variables with respect to ice thickness.

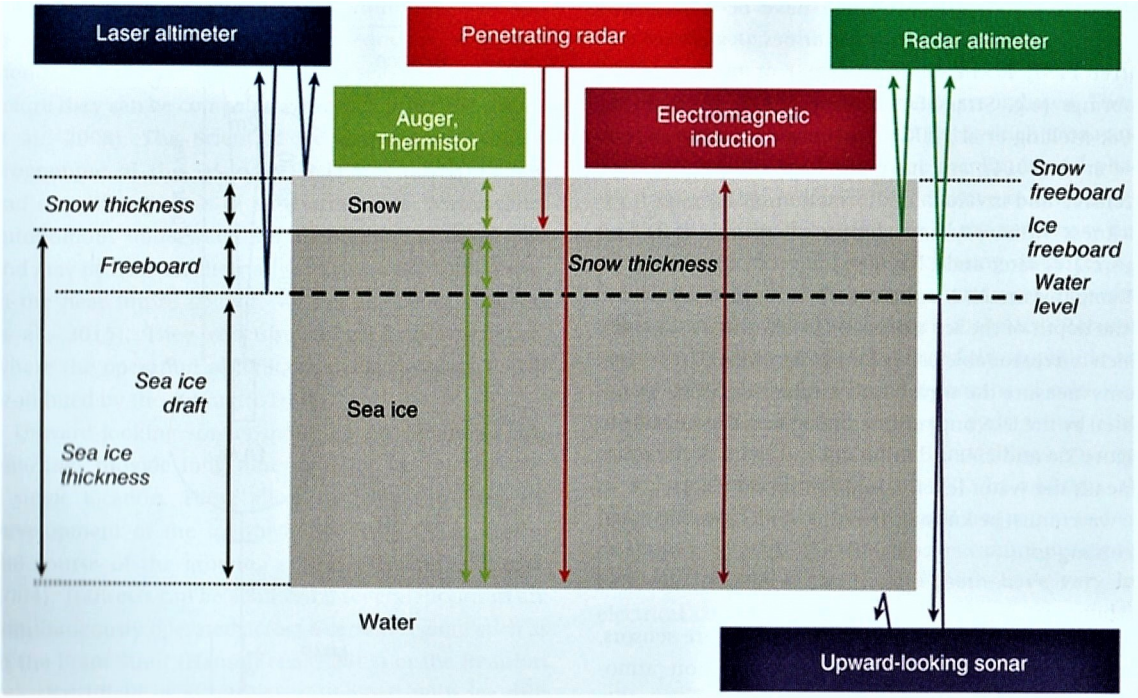

Figure 2.3.1.: Methods of sea ice thickness observation and their penetration profiles of snow and ice layers superimposed on ice floe cross-section with definitions of snow and ice terms and parameters. [Haas, 2017]

2.3.1. Remote Sensing of Sea Ice

Most early noninvasive observations of sea ice thickness come from military nuclear submarines or from scientific ocean moorings mounted to the ocean floor, with ice thickness being determined by means of upward – looking sonar [Wadhams 2000; Thomas and Dieckmann 2003].Only since the 1980s has American and Canadian work established the use of electromagnetic (EM) induction sounding for regional sea ice thickness mapping [Kovacs et al. 1987; Kovacs and Holladay 1990]. Further efforts in Finland and Germany [Haas et al. 2009; Multala et al. 1996] led to the operational use of airborne EM and ground based EM as the most accurate and efficient method for sea ice thickness mapping in the Arctic and Antarctic today. This method is discussed in more detail in Chapter 3.

Although sea ice extent and concentration can be measured with sufficient accuracy by

satellites, there exists to date, no space-borne sensor capable of measuring ice thickness reliably. Most satellite sensors observe surface characteristics of the ice and don't have the ability to 'see' into or through the ice. The major properties that influence the radar remote sensing signature of sea ice are dielectric properties (material) and the scattering (geometrical) properties of the ice and its snow cover. The dielectric permittivity of a material describes the manner in which electromagnetic waves are reflected and transmitted when they are incident at the surface. This is related to the ability of the material to polarize in response to an electric field.

Earth-observing satellite systems with imaging radar instruments operate in the microwave range of the electromagnetic spectrum (300 GHz - 300MHz) and measure the backscatter characteristics of the illuminated surface. Backscatter is the portion of the transmitted radiation, that is redirected, through reflection and scattering, back towards the sensor. Sea ice reflectance is dependent on the sum of scattering and reflectance at the surface and the absorption and scattering of the electromagnetic field in the ice volume. As a function of instrument wavelength, polarization, and incident angle, the scattering of radar waves from sea ice is determined by the combined effect of the dielectric constants of ice and snow, the presence of dielectric discontinuities or discrete scatterers within the ice volume (i.e. gas inclusions), the surface roughness, and the geometry of the surface features relative to the angle of the sensor [Eicken, 2009].

At a temperature of -5°C radar waves can penetrate more than a meter into low saline MYI, while the penetration depth in saline FYI is only up to a few centimeters. Under those conditions and with a cold, dry, and homogenous snow cover some general assumptions can be made for radar image interpretation. Ice surface scattering is dominant in FYI and radar backscatter coefficients are largely determined by ice surface roughness. For Arctic MYI, volume scattering from gas bubbles and brine inclusions is predominant in radar backscatter signatures. This leads to a relatively high backscatter

coefficient, which results in a brighter target in radar imagery for MYI compared to FYI [Eicken, 2009].Under these dry cold conditions this contrast results in good distinguishability between Arctic FYI and MYI in radar imagery which can be used to track certain ice features.

The backscatter signature of sea ice is very different in the Southern Ocean, where backscatter properties of first-year-ice and multi-year-ice are similar. Since the aging sea ice in Antarctica rarely encounters brine flushing by downward percolating meltwater, the backscatter contrast between MYI and FYI relies on differences in snow cover and surface roughness. Rough sea ice surfaces typically act as diffuse reflectors, resulting in high backscatter and a bright radar target. On the other hand, smooth surfaces like open water and newly formed sea ice act as specular reflectors and reflect a significant proportion of radiation away from the direction of illumination, which results in a low backscatter and thus darker target. Therefore, radar imagery is also being used to determine sea ice extent.

The interpretation of radar imagery is made more difficult by snow that gives a variable contribution to the observed remote sensing signature. There are large differences in the dielectric constant depending on snow temperature and liquid water content, which lead to a high dielectric loss. The penetration depth then decreases because of higher absorption and surface scattering becomes dominant.

As a result, satellites with Synthetic Aperture Radars (SAR), like the European ENVISAT and the Canadian RADARSAT, can be used for sea ice area coverage, the tracking of sea ice features, and to provide estimates on the relative amounts of thin FYI and thick MYI. However, the techniques are not sufficiently developed to give quantitative thickness information [Thomas and Dieckmann 2003].

Other satellite missions like NASA's ICEsat (operational 2003 to 2009) and ESA's CryoSat2 (operational since 2010) are using laser and radar altimetry to derive ice thickness estimates by measuring the height of the sea ice relative to the ocean surface

(sea ice freeboard). In both methods the altimeters send out an EM pulse in the nadir direction to the Earth surface, that is reflected back by the surface. The returned amplitude of the power is recorded over a defined window of time. The shape of the amplitude over time is indicative of the surface reflecting the pulse i.e. smooth sea water or rough sea ice. One of the challenges in determining the freeboard of sea ice is the existence and identification of open water in the form of leads or polynias in the surveyed area [Meier, 2017]. They serve as a reference point for the sea surface height which varies with respect to the geoid due to tides, ocean currents and atmospheric pressure. Once the freeboard height is determined relative to the sea surface, it can be converted to ice thickness under the assumption of isostatic balance of the ice floes in the water. To calculate the isostatic balance, knowledge about the density of the ice and snow is required. Therefore, due to difficulties determining snow depth, snow density and other factors, those sea ice thickness estimates can have low accuracies [Kwok, 2004; Kern and Spreen, 2015], which improve with spacial averaging and low resolution. However, the development of sea ice thickness retrieval from altimeter-based satellite observations is ongoing and better sea ice thickness estimates from improved validation and new sensors like ICESat-2 (to be launched 2018) can be expected in the future.

Due to different scattering and emission properties between the saline young ice and less saline older ice, sea ice age can be estimated using microwave satellite data. During the winter period it is possible to distinguish between FYI and MYI by means of passive microwave or active scatterometer imagery. Ice age can also be estimated by using tracking techniques that are a combination of passive microwave, visible, and infrared imaging as well as in-situ buoys [Meier, 2017], leading to a more detailed categorization of ice age in years (see Figure 2.1.1). Sea ice age can be used as a strictly observational proxy for sea ice thickness, since over large scales older ice in most cases indicates thicker ice. Although thicker ice can also be produced through dynamic processes like

ridging and rafting of young ice, sea ice age as an estimator for sea ice thickness is still generally valid on large scale observations [Meier, 2017].

3. Electromagnetic Induction Sounding

3.1. Electrical Conductivity of Sea Ice and Sea Water

Sea ice is a composite of ice crystals, brine and air. While pure ice characteristically has a very low conductivity, brine is a very good conductor. The electrical bulk conductivity of sea ice is dependent on the electrical conductivity of the brine and the porosity of the sea ice. The conductivity of the brine, which is dependent on temperature and salt content, can reach values of up to 7 S/m. Measurements of ice cores in the Arctic show that sea ice bulk conductivities can range from 0.02 - 0.05 S/m [Haas et al., 1997]. Sea ice conductivity is not just dependent on the brine volume included, but also on the distribution connection and alignment of pores like brine cells and drainage channels. Connected pores lead to a higher electrical bulk conductivity of the sea ice matrix than isolated pores. A vertical orientation of both brine cells and drainage channels within the ice leads to pronounced conductivity anisotropy in the sea ice, with bulk conductivity in the vertical direction being higher than in the horizontal direction [Kohnen, 1976; Timco, 1979; Reid et al., 2006]. Reid et al. (2006) used direct current measurements on East Antarctic pack ice and determined the average horizontal and vertical conductivities of 0.017 S/m and 0.073 S/m respectively. Therefore, sea ice conductivities are two orders of magnitudes smaller than the electrical conductivity of the sea water. Sea

water conductivity is dependent on temperature and salt content. Near the ocean surface sea water conductivities determined by direct in situ Conductivity, Temperature, and Depth (CTD) measurements in the polar oceans lie between 2.2 S/m and 2.9 S/m [Coachman and Aagaard, 1974].

3.2. Electromagnetic Induction Sounding of Sea Ice

In the early nineteenth century Coulomb, Oersted, Ampere, Gauss and Faraday made the first observations of electrical and magnetic phenomena, which were unifiedly described in 1873 by the Scottish mathematical physicist James Clerk Maxwell. He proposed the theory of the electromagnetic field, classifying light as an electromagnetic phenomenon in the same sense as electricity and magnetism, which ultimately led to the recognition of the wave nature of matter. Nowadays all derivations in electromagnetism begin with the Maxwell equations. Faraday's law states that when an electric field in a conductor increases, so that the charge is accelerated, its changing velocity produces a changing magnetic field, which in turn induces a secondary electric field in the conductor [Lowrie (2007)]. Electromagnetism describes this coupling of an electric field **E** and a magnetic field **H**. In an electromagnetic wave **E** and **H** vary with the frequency of the oscillator and are oriented at right angles to each other in the plane perpendicular to the direction of propagation. One of the constants of nature is that electromagnetic waves travel at the speed of light in a vacuum.

The propagation of harmonic electromagnetic fields is described by the following two Maxwell Equations as [Grant and West, 1965]:

$$\nabla^2\mathbf{E} = j\sigma\mu\omega\mathbf{E} - \varepsilon\mu\omega^{\mathbf{2}}\mathbf{E} \tag{3.2.1}$$

$$\nabla^2\mathbf{H} = j\sigma\mu\omega\mathbf{H} - \varepsilon\mu\omega^{\mathbf{2}}\mathbf{H} \tag{3.2.2}$$

with $\omega = 2\pi f$ being the angular frequency,ε the dielectric constant, σ the conductivity, $j = \sqrt{-1}$, and μ the magnetic permeability.

Frequency-domain electromagnetic (EM) induction sounding uses low frequency EM signals of 1 to 100 kHz to survey the distribution of electrical conductivity in the subsurface. Because of the low frequencies and low dielectric constants for sea ice and sea water the second terms of the Maxwell Equations are negligibly small. This quasi-static approximation means that only the direct current conductivity of a media is relevant for the description of low frequency EM. In the following the word 'conductivity' will always refer to the direct current conductivity of the media.

The EM induction method is based on measuring the change in mutual impedance between a pair of coils above the earth's surface. EM instruments have a minimum of 2 coils, which are electrically connected and separated by a fixed distance r. EM induction takes advantage of the variable conductivity characteristics of sea ice and sea water. The transmitting coil of an EM system generates a primary electromagnetic field at a set frequency, that can penetrate the sea ice almost unaffected while it generates eddy currents in the sea water below the ice. These eddy currents induce a secondary EM field, which along with the primary field can be measured with the receiving coil

R_x of the EM system (see Figure 3.2.1).

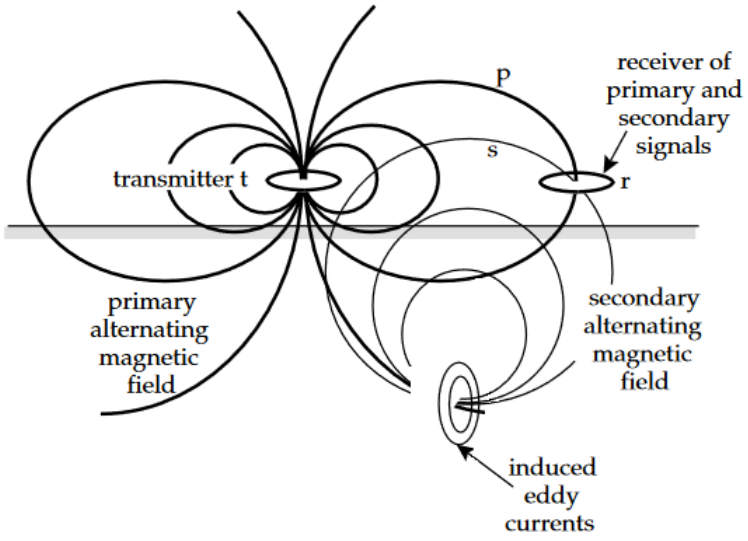

Figure 3.2.1.: Representation of primary and secondary field distribution for the electromagnetic induction method with a horizontal coil orientation adapted from [Lowrie, 2007].

As Figure 3.2.2 shows the secondary field has a shift in amplitude and phase relative to the primary field.

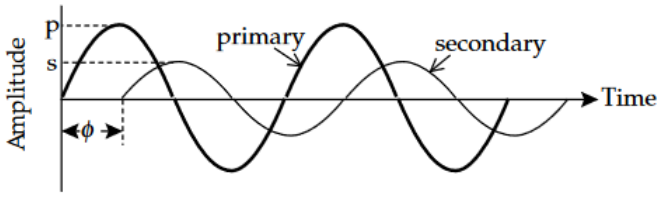

Figure 3.2.2.: Amplitude and phase of the primary (p) and secondary (s) fields with the phase shift $\phi$from [Lowrie, 2007].

The total magnetic field H_t at the receiver is the sum of the primary and secondary magnetic fields and defined as:

$$H_t = H_P^R + H_S^R \tag{3.2.3}$$

EM instruments make relative measurements of the strength of the secondary field in parts per million (ppm) of the actively transmitted primary magnetic field. The response of the measuring system is expressed as the ratio between primary and secondary magnetic field with:

$$\frac{H_s}{H_p} = I + j \cdot Q \tag{3.2.4}$$

The magnitude of the secondary field is broken down into two orthogonal components, the Inphase and Quadrature. The in-phase ratio of the secondary to primary magnetic field response is referred to as the Inphase I. It is the real part of the instrument response and has the same phase as the primary signal. The imaginary part Q is 90° out of phase with the primary signal and referred to as the Quadrature component of the response. Because of its direct relation to the apparent conductivity of the measured subsurface, some frequency based EM instruments only provide the Inphase and the apparent conductivity as instrument returns. The apparent conductivity σ_a of the subsurface can be calculated as:

$$\sigma_a = \frac{4}{\omega \mu_0 r^2} \cdot Q \tag{3.2.5}$$

where μ_0 is the magnetic permeability in a classical vacuum and r being the coil dis-

tance [McNeill, 1980; Haas et al., 1997]. For low and moderate conductivities of homogeneous half-spaces, the magnitude of the Quadrature component of the secondary field is linearly proportional to the apparent conductivity. However, because of high conductivities of the sea water, in the case of sea ice thickness measurements, this correlation doesn't hold true and the relation between between apparent conductivity and true conductivity becomes highly non-linear.

Since sea ice has such low conductivities, only a small fraction of the induced secondary field gets affected by the ice. Therefore the strength of the secondary field is directly related to the distance between the coils, the distance to the sea water surface, and the conductivity of the sea water. With a known height of the EM system above the snow or ice surface and known conductivities, ice thickness or the sum of ice and snow thickness can be estimated by the difference between electromagnetically determined height above ice water interface, described in the model by the combination of instrument height, snow and sea ice thickness, and instrument height above the ice and snow surface. This type of ice thickness estimation is possible as long as sea ice conductivities are low and work especially well with thermodynamically grown ice.

3.2.1. 1 D Model Theory

The ratio between primary and secondary field can be calculated for a subsurface of infinitely laterally extended homogeneous layers with different conductivities and thicknesses as shown in Figure 3.2.3.

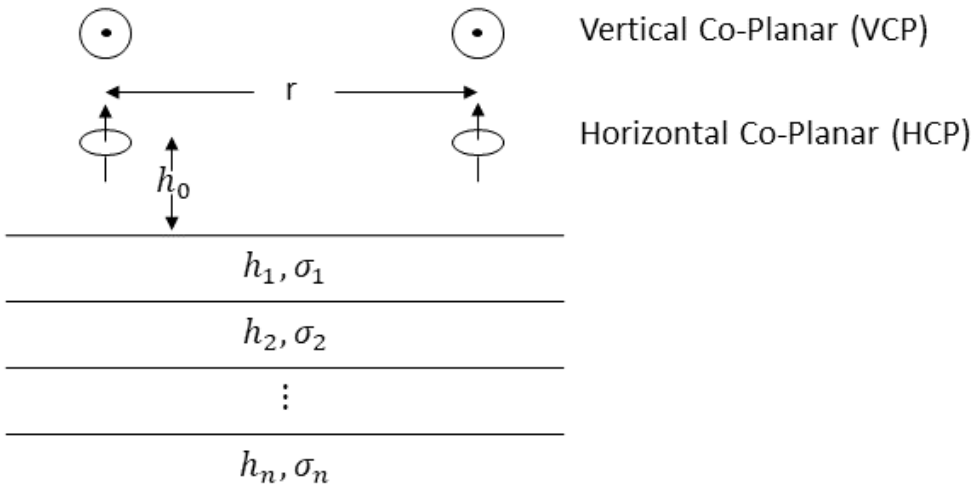

Figure 3.2.3.: Schematic representation of n-layered 1D model with HCP and VCP coil orientations for calculating an EM instrument responses after equation 3.2.6 adapted from [Haas, 1997].

The relation between the transmitted primary field and received secondary field is defined by [Mundry, 1984]:

$$\frac{H_s}{H_p} = -r^2 \int_0^\infty \lambda R_1 \cdot e^{-2\lambda h_0} \cdot g\left(\lambda r\right) d\lambda \tag{3.2.6}$$

with λ being the integration constant and h_0 the instrument height above the ice or snow surface. The function $g\left(\lambda r\right)$ is dependent on the coil orientation of the instrument and with it the orientation of the dipole created. The transmitting and receiving coils of an EM measurement system can have different orientations relative to each other and the subsurface [Frischknecht et al., 1991]. The most commonly used orientations

for sea ice thickness sounding with dual loop EM systems are the horizontal co-planar (HCP) mode with the coils oriented horizontal to the subsurface and vertical co-planar (VCP) mode with the coils vertical to the subsurface. The difference between the two modes is displayed in Figure (3.2.3).

For HCP and VCP coil orientations g is defined as:

$$g\left(\lambda r\right) = \begin{cases} \lambda r\, J_0(\lambda r) & \text{HCP} \\ \\ J_1(\lambda r) & \text{VCP} \end{cases} \tag{3.2.7}$$

with J_0 and J_1 being Bessel functions of the first kind and order 0 and 1 respectively. The function g is proportional to the coil seperation distance r, which makes makes the response of the measured signal dependent on the third power of the coil distance. R_1 is a recursive function of the subsurface parameters like the layer thicknesses h_i and layer conductivities σ_i over the layers $i = 0, 1...n$, for which is defined as:

$$R_{i-1} = \frac{K_{i-1} + R_i u_i}{1 + K_{i-1} + R_i u_i} \tag{3.2.8}$$

with

$$u_i = e^{-2h_i v_i} \tag{3.2.9}$$

$$v_i = \sqrt{\lambda^2 + i\omega\mu_0\sigma_i} \tag{3.2.10}$$

$$K_i = \frac{v_i - v_i + 1}{v_i + v_i + 1} \tag{3.2.11}$$

where $u_n \to 0$ for $h_n \to \infty$ results in: $R_{n-1} = K_{n-1}$.

The Hankel transform in equation 3.2.6 can only be solved by using digital filters as described by Anderson (1979) or Guptasarma and Singh (1997). Examples for the implementation of a Hankel transform and further details can be seen in chapter 4.

The most widely used airborne and ground based frequency domain EM systems use one measurement frequency to determine the apparent conductivity of the subsurface. Ice thickness estimates can be retrieved using either the Quadrature or Inphase component, assuming a simple 1 dimensional three-layer-ice-model: air, sea ice (including snow) and sea water with given conductivities for every layer. This is a very good approach for thermodynamically grown young first-year-ice with ice thickness retrievals showing just small deviations of up to 0.1 m [Haas et al. 2009]. However older ice is often thicker and partly grown through deformation processes which can lead to sea water inclusions within the ice resulting in channeling effects of the electrical currents, preventing a deeper penetration of the EM field.

Such abnormalities within the footprint of the EM device can lead to 3D effects. Accordingly, a 1D assumption can't always resolve sea ice thickness proficiently for thick and deformed ice, and can lead to an underestimation of sea ice thicknesses. For airborne data of those ice types it can lead to underestimation by up to 50% [Haas et al. 2009]. Furthermore those basic three-layer-models are not sufficient to represent more complex ice conditions that require more differentiated models with more layers. Four-layer-models are needed to represent a conductive slush layer on top of the ice where the snow was flushed by sea water, or the conductive sub-ice-platelet-layer underneath the consolidated ice prominent near ice shelfs commonly occurring in Antarctica. Those

special cases and how to resolve them using a brute force inversion will be addressed in the following chapters of this thesis.

3.2.2. Sensitivity for different Instrument Settings

Three of the major instrument settings influencing the sensitivity range of frequency based EM measurements are the measurement frequency, coil distance, and coil orientation of the measurement device. The coil distance in combination with the frequency and the height of the instrument directly influence the penetration depth as well as the area of lateral influence, where 90% of the induction takes place is called the Footprint of the EM system [Reid et al., 2006b]. The effective penetration depth, referred to as skin depth, is also dependent on the apparent conductivity of the subsurface. The horizontally progressing eddy currents in the conductive layer limit a deeper penetration of the primary field into the subsurface. At the skin depth δ the magnetic field is attenuated to $e^{-1}(\sim 37\%)$ of its value outside the conductor. The skin depth is dependent on the conductivity of the body and the frequency of the field. It is defined by [Lowrie, 2007]:

$$\delta = \sqrt{\frac{2}{\mu_0 \sigma \omega}} \tag{3.2.12}$$

The skin depth is not the maximum depth of penetration of the magnetic field but rather indicates how rapidly the field attenuates. The horizontal extent of the eddy currents is a measure of quality for the lateral resolution of the method. Multi-frequency devices make use of the changes in skin depth with measurement frequency and the resulting measurement resolution. Higher frequencies with smaller wavelengths provide a higher sensitivity for smaller scale conductivity changes in near surface layers while lower frequencies provide less sensitivity to small scale changes but at the same time enable

deeper penetration of the field and resolution of conductivity changes at greater depth.

Another way to improve or change the sensitivity for different depth penetration is a change in coil orientation. Different coil orientations create different responses in the secondary coil and with it different Inphase and Quadrature behaviors. Figure 3.2.4 and Figure 3.2.5 show the expected Quadrature and Inphase responses at HCP and VCP coil orientations for 1.21 m and 3.66 m coil distances of an instrument height of 10 cm and a frequency of 9800 Hz. The results were produced for a three-layer-model (air, ice, sea water) with changing ice thicknesses at a conductivity of 0 S/m over an endless half space of sea water with a conductivity of 2.5 S/m. The coil distances chosen are comparable to the instrument settings of EM31 and EMP devices (see section 3.3 for further detail).

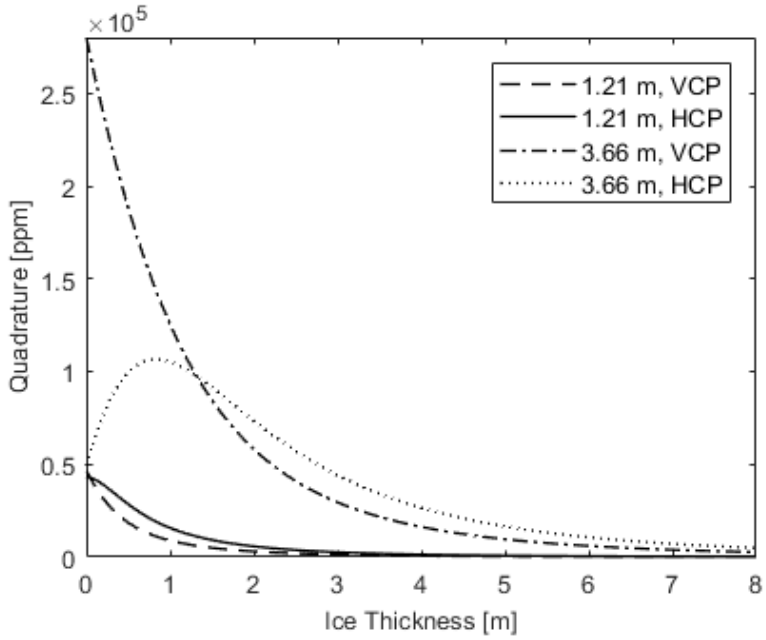

Figure 3.2.4.: Quadrature responses over ice thickness for HCP and VCP orientations at coil distances of 1.21 m and 3.66 m. Based on three-layer-model: instrument height of 10 cm, ice thickness conductivity of 0 mS/m and a water conductivity of 2500 mS/m.

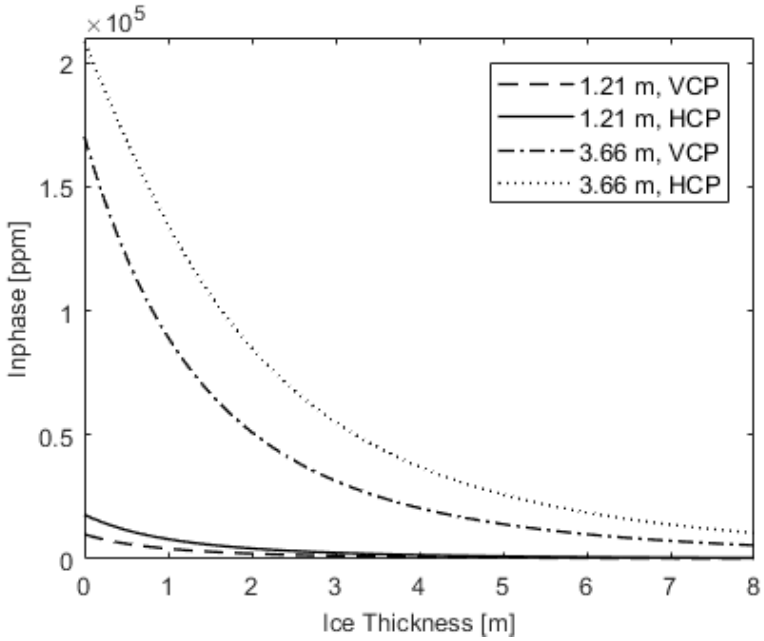

Figure 3.2.5.: Inphase responses over ice thickness for HCP and VCP orientations at coil distances of 1.21 m and 3.66 m. Based on three-layer-model: instrument height of 10 cm, ice thickness conductivity of 0 mS/m and a water conductivity of 2500 mS/m.

Both Figures illustrate that the larger coil distance results in significantly larger instrument returns. A larger coil distance leads to a deeper field penetration and in this case a stronger influence of the conductive sea water underneath the ice which results in a higher Quadrature and Inphase. Furthermore this demonstrates the limitations of sensitivity for instruments with a short coil distance of 1.21 m, since the signal returns are reduced significantly with increasing ice thickness and flatten out at ice thicknesses of over 4 m.

Figure 3.2.4 shows a maximum in the HCP curve for 3.66 m coil distance at 0.8 m ice thickness which creates an ambiguity in the Quadrature results. These instrument settings can therefore only be used for ice thickness measurements when only ice thicknesses of under or over 0.8 m are to be expected. The HCP curve crosses the VCP curve at 1.3 m with higher Quadrature values for larger ice thicknesses for the instru-

ment in HCP orientation. In both the Quadrature and Inphase responses it is evident that an HCP orientation results in higher instrument returns for larger ice thicknesses independent from the coil distance. Therefore an HCP orientation and large coil distances are favored for measuring in areas with expected ice thicknesses of over 10 m and a minimum ice thickness of 0.8 m. In contrast VCP orientations provide a steeper curve for Inphase and Quadrature returns especially in the 0-2 m ice thickness range. This results in a better signal to noise ratio, in turn providing a higher resolvability of thickness changes down to a few cm. Hence VCP orientation are commonly chosen to measure smaller ice thicknesses.

While longer instruments provide stronger signal returns and deeper penetration, shorter instrument are often much easier to handle and can be sufficient to measure sea ice within a certain thickness range. As the previous section has shown, instrument parameters like coil orientation, coil distance as well as measurement frequency should be chosen with the targeted subsurface in mind to optimize measurement results.

3.3. Instrumentation

EM ice thickness measurements are not just efficient and have a high accuracy level, but also are non destructive and do not require any additional contact with the ice or snow. Nondestructive measurements are a requirement for when drill holes could disturb the hydro static equilibrium of the ice and with it the thermodynamic balance in long term studies of ice thickness change. Since EM measurements do not require contact with the surface, EM induction sounders can be easily deployed on a sledge or kayak and towed by hand or with a snowmobile, while being protected from various surfaces like melt ponds. Furthermore, it allows deployment of EM sounders from any kind of platform including icebreakers, hovercraft or even airborne deployments on helicopters and airplanes [Eicken, 2009]. Applications on helicopters and planes are referred to as airborne EM measurements.

Different ground based frequency EM systems were used for this thesis. As mentioned in section 3.2, EM instruments with larger coil distances have larger skin depth and provide better sensitivity for deep layers, whereas short instruments are often easier to handle and provide higher resolution for near surface targets. Multi-frequency devices generally offer more information with high frequencies being sensitive to shallow layers and conductivity changes, and lower frequencies with larger wavelength providing information about deeper layers at the same time. Accordingly the right instrument and coil orientation has to be chosen to have a sufficient resolution for the desired target. For sea ice thickness measurements within this thesis, EM instruments were mounted on a sledge or toboggan and towed by hand or behind a snow mobile.

3.3.0.1. EM31

The EM31 from Geonics runs with a single operating frequency of 9.8 kHz and exists in two versions: EM31-MK2 having a 3.66 m coil distance and EM31-SH with a 2.0 m coil distance. The measurement return includes apparent conductivity in mS/m as well as Inphase in parts per thousand (ppt) with a measurement accuracy of $\pm 5\%$ at 20 mS/m. The noise levels are given with 0.1 mS/m for the conductivity and 0.03 ppt for the Inphase ["Geonics EM31-MK2 | EM31-SH".,2013]. While the conductivity measurements of the EM31 are well calibrated, the Inphase results have to be adjusted for the measurement conditions. For comparison with the modelled instrument returns the Inphase is therefore transferred into part per million (ppm) and an offset as well as a gain are applied to the signal (see chapter 5 for more detail). For the application of the inversion and model comparisons conductivity measurements are transferred into Quadrature results (ppm) [McNeill, 1980].

These instruments have been used extensively for sea ice thickness measurements in the Arctic and Antarctic under summer and winter conditions [Kovacs and Morey, 1991; Haas et al., 1997, 2008]. Figure 3.3.1 shows the setup of an EM31-SH powered by a car battery on a sledge being towed behind a snow mobile. The EM31 measurement responses are given for the Inphase in parts per thousand (ppt) and the apparent conductivity of the subsurface in mS/m. The EM31 is the most widely used EM instrument for sea ice thickness measurements and can be operated in both HCP and VCP mode.

Figure 3.3.1.: EM31-SH setup on sledge towed behind a snow mobile.

3.3.0.2. EMP

The Profiler EMP-400 from GSSI with a coil distance of 1.21 m is much smaller and lighter device than the short version of the EM31. It can be run simultaneously at 3 operating frequencies between 1 kHz and 16 kHz in both HCP and VCP mode with a sampling rate of 0.5 sec ["Profiler TM Profiler EMP-400 Manual".,GSSI, 2017]. Measurement outputs are given as Inphase and Quadrature in ppm as well as the apparent conductivity in mS/m. It offers well calibrated conductivity and Quadrature outputs. However, the Inphase returns have to be adjusted to the measurement setup. The calibration of the Inphase for the EMP-400 is discussed in further detail in Chapter 6. Figure 3.3.1 displays the setup of the EMP-400 on a toboggan towed by hand.

Figure 3.3.2.: EMP- 400 fixated on a toboggan.

The EMP-400 so far has not been widely used for sea ice thickness measurements but more for soil measurements and archaeological prospecting. Chapter 6 discusses the benefits and limitations of the instrument with regards to a variety of sea ice thickness measurements.

4. 1D Forward Model and Inversion

The following chapter will discuss the details of the 1D forward modelling code and inversion scheme that were developed for this thesis. Furthermore, it will describe the GUI (graphical user interface) that was created to calculate 1D EM forward models for a variety of instruments. As part of the inversion other analytical tools used, like best fit and RMSE, will be addressed.

4.1. Forward Model

Equation 3.2.6 is a so called Hankel integral transform of the type:

$$K(b) = \int_0^\infty k(\lambda)\, J_n(b\lambda)\, d\lambda$$

where J_n is a Bessel function of the first kind and order n and $k(\lambda)$ is the function being transformed, a so called kernel function. A Hankel transform can be computed by using digital filters, designed for use with a specific kernel function such as J_0 and J_1as described by Guptasarma and Singh (1997) and Anderson (1979). For the data analysis done within this thesis, the forward modelling scheme ODFEM (One Dimensional Frequency domain Electromagnetic Model) was developed with MATLAB© that is based on the digital filters for Hankel J_0 and J_1 transforms described by Guptasarma

and Singh (1997). These filters used for ODFEM show a better error performance and allow for faster computing times than older filters available for these transforms from Anderson (1979), which are much longer and have a higher sampling density using 16 digit weights compared to the 12-digit weights used by Guptasarma and Singh, 1997. All model calculations done in this thesis use the short digital filter coefficients from Guptasarma and Singh (1997) since the use of the long coefficients increases processing time and doesn't improve accuracy of the results when the noise level of common EM instruments is taken into account.

To test the accuracy of the new 1D forward modelling code, modelling results of Inphase and Quadrature components for the coil configurations HCP and VCP were compared with EM responses calculated by Haas et al. (1997). The models calculated by Haas et al. (1997) were implemented using FORTRAN and based on Anderson (1979) transform filters. For the quality test a set of receiver responses has been modeled for a 1D case with the following parameters: a coil distance of $r = 2.67m$, a frequency of $f = 4060Hz$, changing values for instrument height above the halfspace of $h_m = 0 - 4.9\,m$ in 10 cm intervals, as well as a changing halfspace conductivity of $\sigma_2 = 0.3 - 4.9\,S/m$ in $0.1\,S/m$ intervals. These model parameters were chosen according to the model results available from Haas et al. (1997).

For comparison of the two modelling codes, the absolute difference between Inphase and Quadrature responses was calculated in ppm of the transmitted field . The resulting values displayed in Figure 4.1.1 and Figure 4.1.2 show the absolute difference between the receiver responses of ODFEM and the model after Haas et al. (1997).

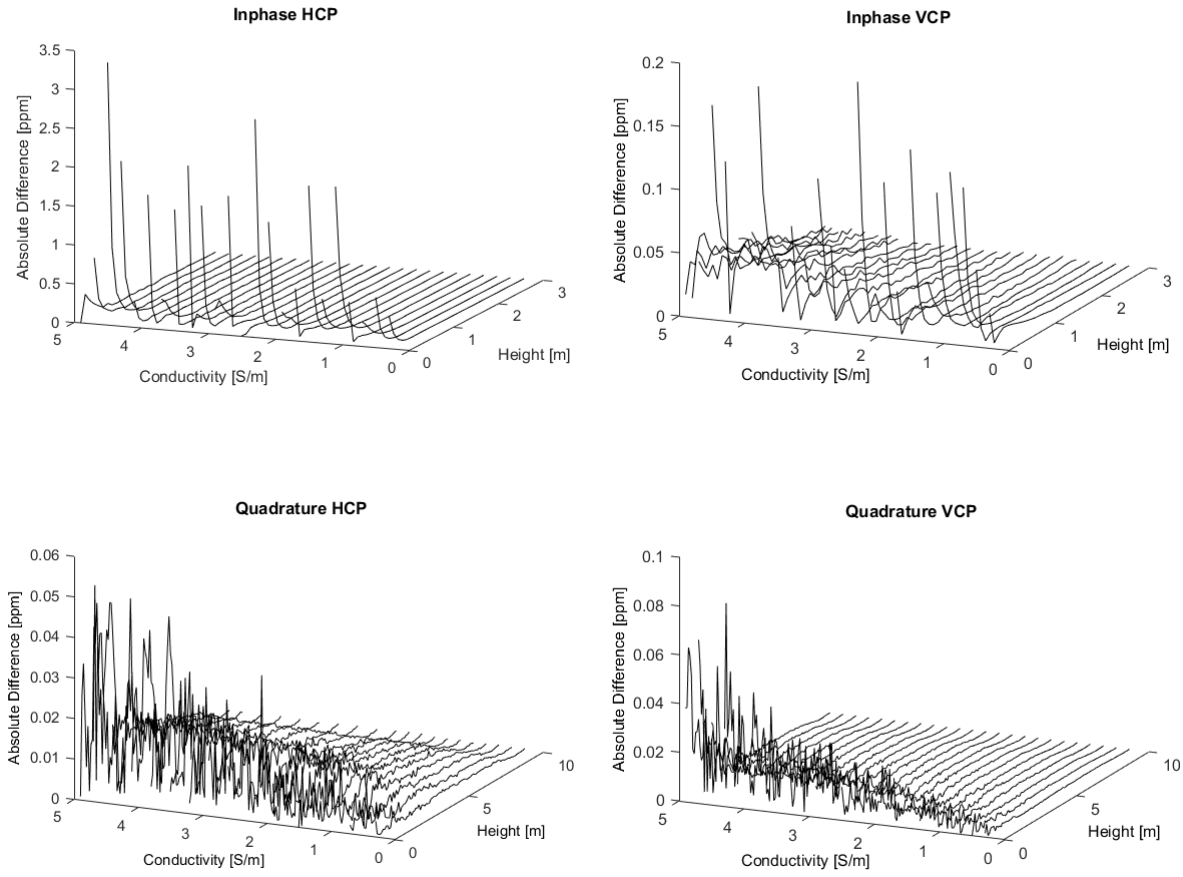

Figure 4.1.1.: 3D view of absolute differences of model response between ODFEM and Haas (1997) in ppm for Inphase (top) and Quadrature (bottom) for HCP and VCP coil orientations. Results are displayed with different y-axes and x-axes ranges for optimal visibility of the error values. In the given model halfspace conductivities range from $\sigma_2 = 0.3 - 4.9\,S/m$ and instrument heights of $h_m = 0 - 4.9\,m$.

Figure 4.1.1 displays the range of difference in Inphase and Quadrature responses and the change over increasing halfspace conductivity. Figure 4.1.2 provides a 2D view of Figure 4.1.1 at varying instrument heights. Variations in the Inphase and Quadrature between the two modelling codes are negligible over most instrument heights. Increased differences between the models can be observed for small instrument height of under 1 m for the Inphase and under 3 m for the Quadrature. It shows that the Inphase responses have a higher offset between the models than the Quadrature responses. In

this case the Inphase components for a HCP orientation differ by up to 3.4 ppm for an instrument height of 0 cm. That effect is greatly reduced by increasing the instrument height to over 10 cm. However, at any height of the instrument the difference in model codes is still well below the noise level of common EM instruments i.e the EM31 with 5% instrument noise being around 50 ppm. The designed model code is therefore suitable for airborne and ground based frequency EM analysis.

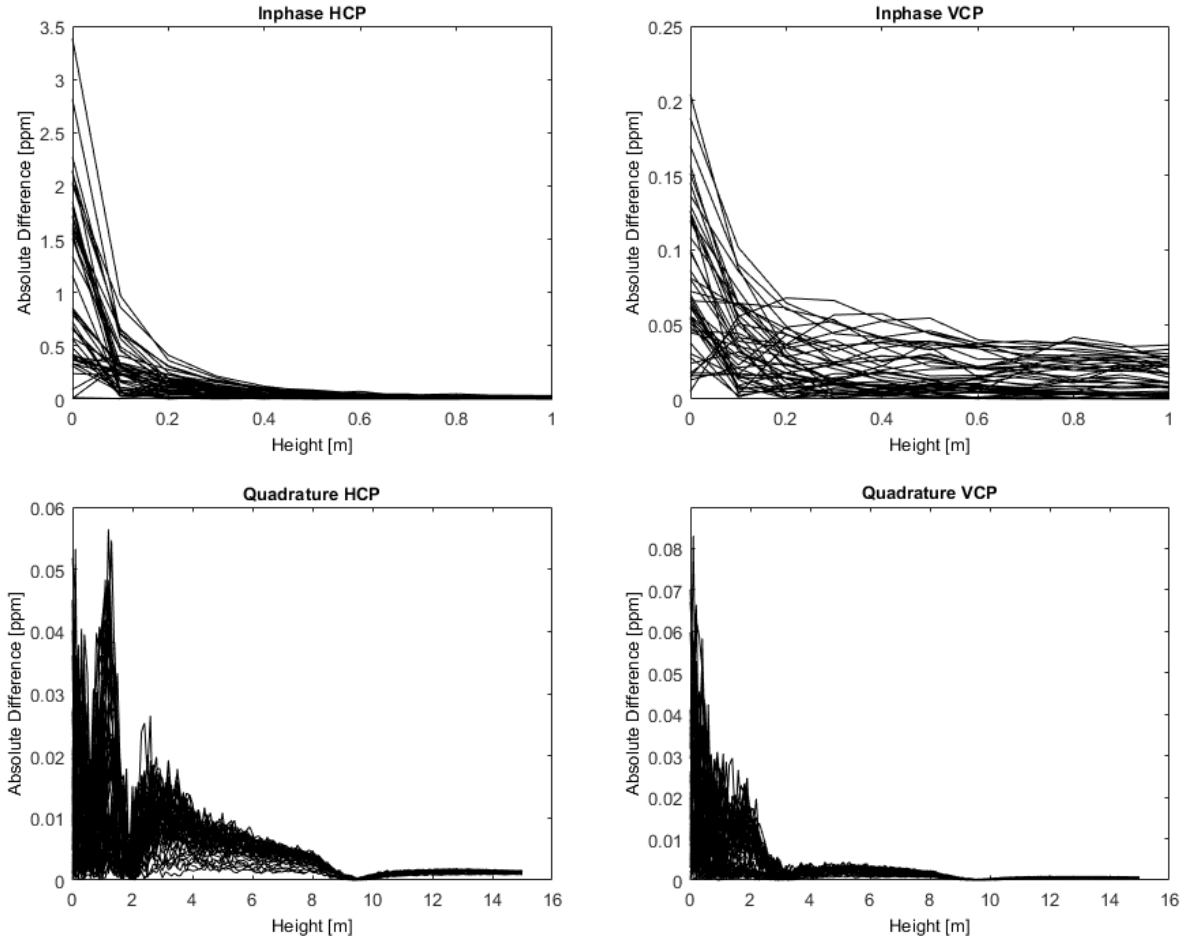

Figure 4.1.2.: 2D view of absolute differences of model responses between ODFEM and Haas (1997) in ppm for Inphase (top) and Quadrature (bottom) for HCP and VCP coil orientations. Results are displayed with different y-axes and x-axes ranges for optimal visibility of the error values. In the given model halfspace conductivities range from $\sigma_2 = 0.3 - 4.9\,S/m$ and instrument heights of $h_m = 0 - 4.9\,m$.

4.2. ODFEM GUI

To enable easy access and use of ODFEM (One Dimensional Frequency domain Electromagnetic Model) for users without coding experience, a GUI (graphical user interface) was created as part of this thesis. The GUI provides three main interfaces shown in Figures 4.2.1, 4.2.2 and 4.2.3 that allow the user a great degree of customization to calculate 1D models that fit their needs.

The first interface displayed in Figure 4.2.1 allows the user to set the instrument parameters of their EM device. It is possible to either choose a preset of instrument settings, customize your own instrument settings, or a combination of both. The user can choose to calculate models for up to 3 frequencies at a time.

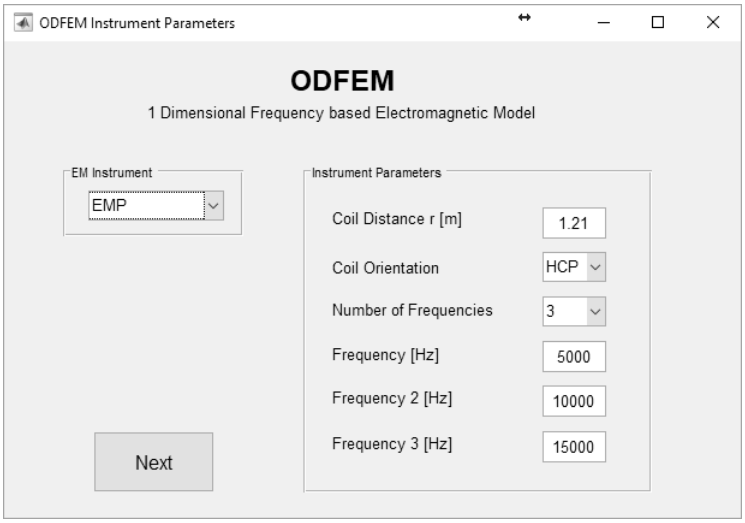

Figure 4.2.1.: ODFEM program GUI interface for instrument parameter settings.

Model parameters are being set on the second interface. The user can choose the number of layers and their resolution, as well as the conductivity and thickness limitations of each layer. The top layer is set as the instrument height and the conductivity of this layer is by default set to 0 mS/m. The minimum number of layers for sea ice applications

should therefore be 3, with the top layer being air, the second layer being ice and snow, and the third layer being sea water. Within this application the maximum number of possible layers is 5 with the thickness of the last layer being set to infinity by default. Thicknesses ranges for the layers can be chosen by setting the minimum and maximum thickness. A layers thickness can be set to a constant value by setting minimum and maximum thickness to the same value.

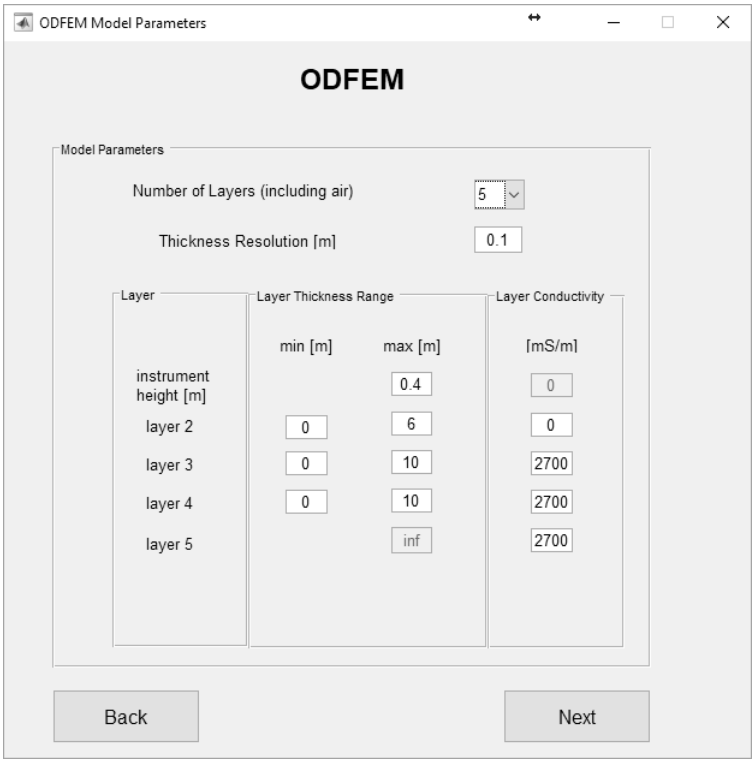

Figure 4.2.2.: ODFEM program GUI interface for model parameter settings.

The third interface offers options on how to save your model. The user can choose between .mat format, which is a MATLAB exclusive format, a general tab delimited ASCII .dat file, or both. The directory and filename can be selected, and once the directory is set the model can be run. Beware that computing time will increase with an increasing amount of layers and frequencies as well as with bigger thickness ranges on those layers in combination with a small resolution.

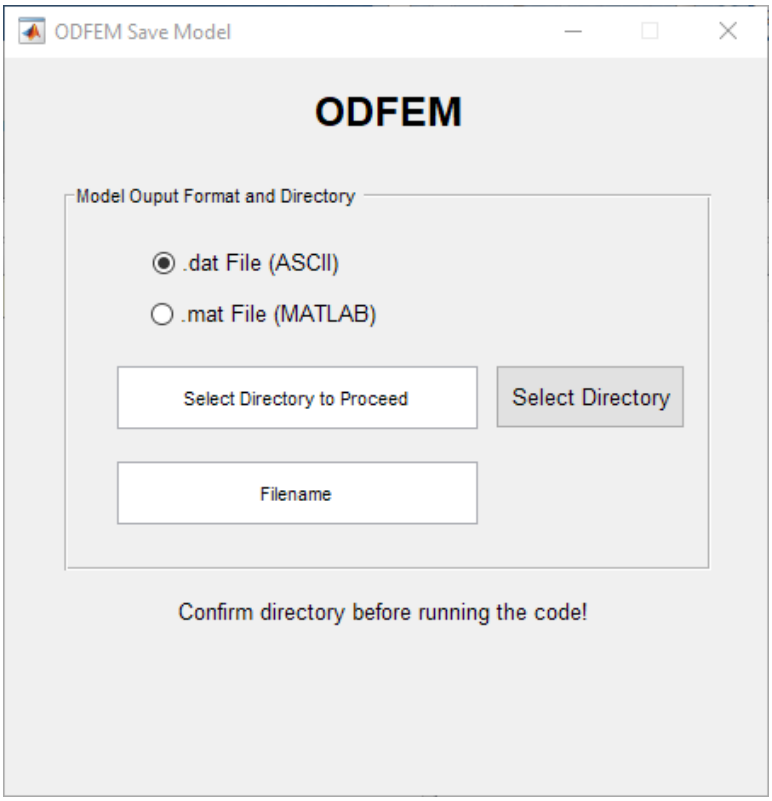

Figure 4.2.3.: ODFEM program GUI interface for model output format and directory.

After the model is calculated and saved in the desired format, the last interface lets you start over to calculate a new model or exit the program. The saved files contain all the chosen parameter settings as well as the calculated Inphase and Quadrature values. Details on the file format for the output files can be found in Appendix A. The installation package for ODFEM can be found under: `https://github.com/anneirvin/ODFEM` as well as on the Pangea.de data publisher.

4.3. Inversion

Inverse solutions are key problems in many natural sciences. Whenever data are collected and the intent is the extraction of information from it, the physical laws that define this data, have to be taken into account. In geophysics deriving properties of the earth, or instead a model of the earth, from the observed data that have been affected by the variations in properties of the earth, constitutes an inverse problem. To understand how the data are affected by the model, the forward problem solution, which describes the mathematical relation between theoretical data and the assumed Earth model, has to be determined first. The method of reconstructing the properties of the earth (i.e. conductivity and thickness of an ice layer) from the observed data , is referred to as the inverse problem solution. Inversion is therefore a way of transforming the data into more easily interpretable physical quantities [Sen and Stoffa, 2013].

Solving the inverse problem involves finding the whole set of model responses that can explain the observed data. Inversion methods can be classified into two categories: direct or operator based inversion methods and model-based inversion methods [Sen and Stoffa, 2013]. Direct inversion methods must be formulated based on the physics of the forward problem by designing a mathematical operator that is applied to the observed data to derive a model or physical properties of the earth. Whereas, model-based inversion methods involve generating synthetic data from an assumed model and comparing it with the observed data. Within geophysics the observed data always contains a certain amount of error created by noise. Therefore, the data never exactly fits the modelled geophysical data and as a result the goal is to obtain a quasi-solution of the inverse problem with a model that provides the closest-fit to the observed data [Zhdanov, 2002].

To solve an inversion problem three main conditions have to be met: existence, stability, and uniqueness of the solution. The solution of the inverse problem has to exist. Stabil-

ity is an indicator on how error in the data propagates into the model. A stable solution is therefore insensitive to small errors in the data values [Sen and Stoffa, 2013]. A solution is said to be unique if, when changing a model m_A to m_B, the data also change from D_A to D_B. In a case where the solution is not unique, several models would explain the data equally well. One of the necessary conditions for a unique solution is that there are as many equations, or measured data, as the number of unknown model parameters. Such a problem is called an even-determined problem. In an under-determined problem there are fewer data than the number of model parameters, which is a common case in geophysical problems [Sen and Stoffa, 2013]. An under-determined problem leads to non-unique solutions. The problem can be reduced to an even-determined or even over-determined case by discretization (i.e dividing the subsurface into a finite number of layers to be resolved) which reduces the number of model parameters. An over-determined system, with more data than model parameters, can reduce the effect of noise on the inverse solution and is therefore the desired case [Zhdanov, 2002].

The majority of forward problems are not linear: these are thereby described as non-linear. There is no general method to solve nonlinear inverse problems. There are some solutions that work for individual problems, like forward modeling, brute force inversion of the forward problem, and linearization, an approximation of the nonlinear forward problem with a linear equation [Aster et al., 2013]. All these methods are model based and thus include an optimization process in which a model is sought that explains the observations best [Sen and Stoffa, 2013]. As part of this thesis a model-based brute force inversion was developed to solve the non linear problem of EM induction sounding for sea ice.

4.3.1. Brute Force Inversion

A brute force search or exhaustive search is defined as an algorithm that systematically enumerates all candidates for a solution while checking whether each candidate fulfills the problems statement. The brute force inversion developed for this thesis is a model based grid-search inversion method for which synthetic data are calculated and compared with the observed data. If the match between the observed data and the synthetic data is acceptable, the model is accepted as the solution [Zhdanov, 2002]. Otherwise the model is changed, the synthetic data are recomputed, and compared again until an acceptable match is obtained between data and synthetic data. Since the observed data always includes some noise there will never be a perfect match, however, there is a model which provides synthetic data 'close enough' to the observed data. The inversion problem therefore is being reduced to determine the model that minimizes the difference between observed and synthetic data. In this case the difference is determined as distance in between two elements in a metric space [Zhdanov, 2002].

An acceptable match for the sea ice case depends on the sensitivity of the instrument and the thickness of the ice layer observed. For EM sea ice measurements usually an error of about 10 % or less can be assumed for level first year ice. However, as mentioned in the previous chapter, airborne EM measurements can have an underestimation of up to 50% for large ice thicknesses. Therefore, each case of what constitutes an acceptable match has to be evaluated independently and all contributing factors like other noise sources or penetration depth of the instrument have to be considered. More case specific limitations for ice thickness resolutions with certain instrument settings can be found in Chapter 5 and 6.

Within this inversion, ice thicknesses are inverted by searching the output of the forward models for the pair of computed Inphase and Quadrature values that most closely agree with the measured values. In this "brute force" inversion, the complete model space of

pre-computed instrument responses is being searched to find the Inphase, Quadrature pair with the global minimum distance d between model and observations as described in Figure 4.3.1.

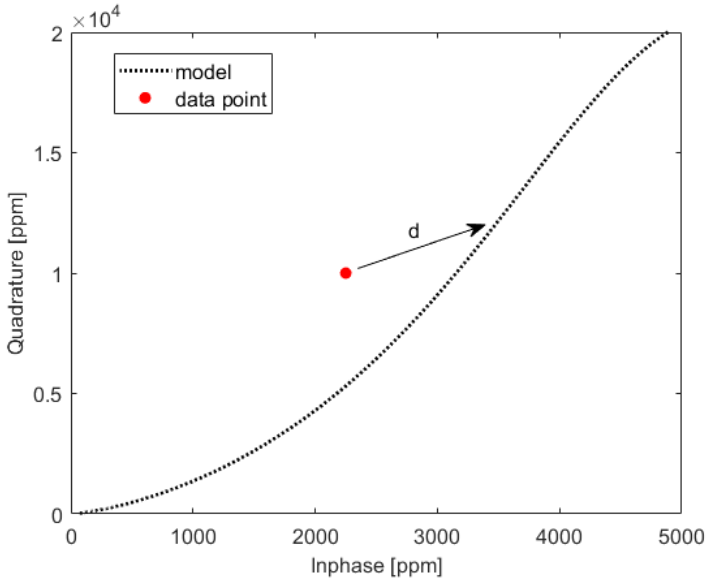

Figure 4.3.1.: Example for calculating minimum distance d between model and observed data for Inphase and Quadrature pairs.

The calculated distance is dependent on the number of observations (i.e number of frequencies and instrument responses) used within the inversion. More parameters used in the distance calulation can decrease the effect of noise on the inversion and therefore lead to a more stable and accurate result.

For one frequency the optimal Inphase and Quadrature pair is found using the minimum of the distance d between the data sets after [Zhdanov, 2002]:

$$d = \sqrt{(I_{obs} - I_e)^2 + (Q_{obs} - Q_e)^2}, \tag{4.3.1}$$

where I_{obs} and Q_{obs} are the observed instrument returns and I_e and Q_e the expected modelled returns. This allows for the determination of the thickness of the changing

layers with the resolution chosen in the forward modeling.

The instrument EMP-400 is a multi frequency EM device and measurements can be made of up to 3 frequencies at a time. Since an over-determined system produces a more stable inverse problem solution, the instrument returns of all 3 frequencies are being used for the inversion. When 3 frequencies are being used the minimum for d is found by calculating the sum of the distance for all Inphase pairs and all Quadrature pairs according to:

$$d = d_I + d_Q \tag{4.3.2}$$

$$d_I = \sqrt{(I_{obs,f_1} - I_{e,f_1})^2 + (I_{obs,f_2} - I_{e,f_2})^2 + (I_{obs,f_3} - I_{e,f_3})^2} \tag{4.3.3}$$

$$d_Q = \sqrt{(Q_{obs,f_1} - Q_{e,f_1})^2 + (Q_{obs,f_2} - Q_{e,f_2})^2 + (Q_{obs,f_3} - Q_{e,f_3})^2}, \tag{4.3.4}$$

with f_i standing for the frequency number. This approach was chosen so d can easily be calculated for just the Quadrature or the Inphase. The Inphase return of an instrument is often not sufficiently calibrated. To use the data anyways d can be calculated with Quadrature returns using only Equation 4.3.4.

4.3.1.1. Validation of the Inversion

To validate the quality of the inversion, the Root Mean Square Error (RMSE) between the observed thickness data (drill holes) and the inverted layer thickness can be determined. This is only possible when ice thickness measurements and EM measurements at the drill sites are available. The RMSE is a common statistical measure for the differences between the values predicted by a model and observed values [Barnston, 1992]. In this study RMSE is calculated as an average RMSE for the different changing layers, like sea ice and snow, within the model. The average is used since layers like snow and ice can have very different thickness ranges. While snow usually changes in the tenth of centimeter range, ice thickness can change in the meter range. This helps avoid the bias created within the RMSE calculation towards big differences in data value [Murphy and Epstein, 1989; Willmott and Matsuura, 2005]. Furthermore, RMSE values for each layer can be calculated and can possibly show the difference in sensitivity to resolve one specific layer. The RMSE for each model is calculated using:

$$RMSE = \frac{1}{NL}\left\{\sqrt{\frac{1}{N}\sum_{i=1}^{N}\left(LT1_{m,i} - LT1_{obs,i}\right)^2} + \sqrt{\frac{1}{N}\sum_{i=1}^{N}\left(LT2_{m,i} - LT2_{obs,i}\right)^2}\right. \tag{4.3.5}$$
$$\left. + \ldots + \sqrt{\frac{1}{N}\sum_{i=1}^{N}\left(LTNL_{m,i} - LTNL_{obs,i}\right)^2}\right\},$$

with $LT1_{m,i}$ and $LT1_{obs,i}$ being the layer thickness of layer 1 for modelled and observed values respectively and i = 1,2,...,N being the number of data values. The RMSE is calculated as an average of NL, the number of changing layers.

Once the RMSE for each model has been determined it can additionally be used to

resolve other contributing factors like layer conductivity or the calibration of the Inphase. As described in Chapter 5 and 6, to determine a layer conductivity, results are obtained by searching for the minimum RMSE among a set of different model runs with changing conductivities for one layer.

In the case of Inphase calibration the same model is used but instead a changing gain is applied to the measured Inphase values. The smallest RMSE then determines the gain applied on the Inphase. The Inphase calibration is dependent both the instrument and the models used. Therefore, a more detailed description on Inphase calibration and the use of RMSE for different instruments can be found in Chapter 5 and Chapter 6.

5. Inversion of Multi Frequency Data

This chapter will discuss a method of retrieving conductivities and thicknesses of more than one sea ice layer using a brute force inversion of multi-frequency data. Multiple frequencies or measurement parameters offer the possibility of jointly resolving more than one model parameter like sea ice thickness or conductivity. The following describes in detail how using 3 measurement frequencies enables the resolution of a snow and slush layer, a wet saline snow layer, on top of the ice. The field data used in this chapter were acquired using the Profiler EMP-400 from GSSI (more details in Chapter 3)

5.1. Measurements and Field Campaigns

The data used within this chapter were collected during two separate field campaigns in the Arctic in 2013 and 2017. The first data set was collected in a field campaign conducted from Alert, Nunavut Canada with measurement sites located in the Lincoln Sea north of Ellesmere Island, Canada. For this campaign the EMP was mounted on a toboggan at 10 cm height with an HCP orientation and towed by hand as shown in Figure 3.3.2. Measurements were collected on 8 different ice floes (2 FYI and 6 MYI sites) with up to 5 drill hole measurements per site. A general description of drill hole measurements can be found in chapter 2 section 2.3. For this study 37 drill hole measurements were used and concurrent EM data were collected at 3 frequencies: 4 kHz, 9 kHz and 15 kHz (see Appendix B.2) .

The data set used for the second study was collected during a field campaign conducted in April and May 2017 from Qikiqtarjuaq near Broughton Island , part of the Davis Strait, at the east coast of Baffin Island in Nunavut, Canada. EM surveys and drill-hole measurements were carried out on landfast sea ice west and south of Broughton Island. During this field campaign measurements of sea ice thickness, slush, and snow depth were collected along more than 200 km of survey tracks traversed on skies and snowmobile. The EMP was pulled behind a snowmobile or the skier on a toboggan at an instrument height of 10 cm above the snow surface with EM data being obtained at 3 frequencies: 5 kHz, 10 kHz and 15 kHz. For this study 85 drill hole ice, snow, and slush thickness measurements within the footprint range of the EM instrument were used (see Appendix B.1).

5.2. Assessment of Data Quality

The EMP has not been widely used for sea ice measurements. Weissling et al. (2011) produced an internal report on data quality and feasibility of this device for sea ice thickness measurements. However the EMP is a multi-frequency device that is lightweight and small and therefore easily usable. Furthermore, the analysis applied on EMP data in the following and all of chapter 5 is generally applicable to other ground-based-multi-frequency and airborne EM devices.

5.2.1. Forward Model vs Exponential Fit for Simple Sea Ice Thickness Inversions

Ice thickness analysis for single-frequency devices as described by Haas et al. (1997) commonly includes a statistical analysis of drill hole measurements by means of fitting an exponential function to the measured instrument response in ppm versus the ice thickness . This resulting exponential function is then used to calculate ice thicknesses. The benefit of this method is that outside influences (for example an offset in the signal due to install of the instrument on a sled that affects the magnetic field through metal components) on the signal are irrelevant as long as all of the signal is equally affected. This method is however limited to very 'simple' single-layer sea ice conditions with the model assumption that sea ice and snow are seen as one layer. Thanks to the limitations of the assumed ice structure, it is often sufficient to just use one instrument response parameter, i.e. Inphase or Quadrature, which allows the user to choose the instrument return with the best signal quality and highest signal to noise ratio. In comparison to the exponential fit method, using a forward model in combination with an inversion has the benefit of enabling the resolution of more than one subsurface parameter i.e. sea ice thickness as well as conductivity or thicknesses of more than one layer.

Figure 5.2.1 shows an example of the exponential fit of EM drill hole data from the

Alert 2013 campaign's Quadrature. It also includes the estimated instrument returns for Quadrature from the 1D models for the frequencies calculated with ODFEM (see chapter 4 for more details). The models created for 3 frequencies: 4 kHz, 9kHz and 15 kHz, assume a simple three-layer case of air, sea ice and sea water with a sea ice conductivity of 0 mS/m and a water conductivity of 2400mS/m at a layer thickness resolution of 1 cm.

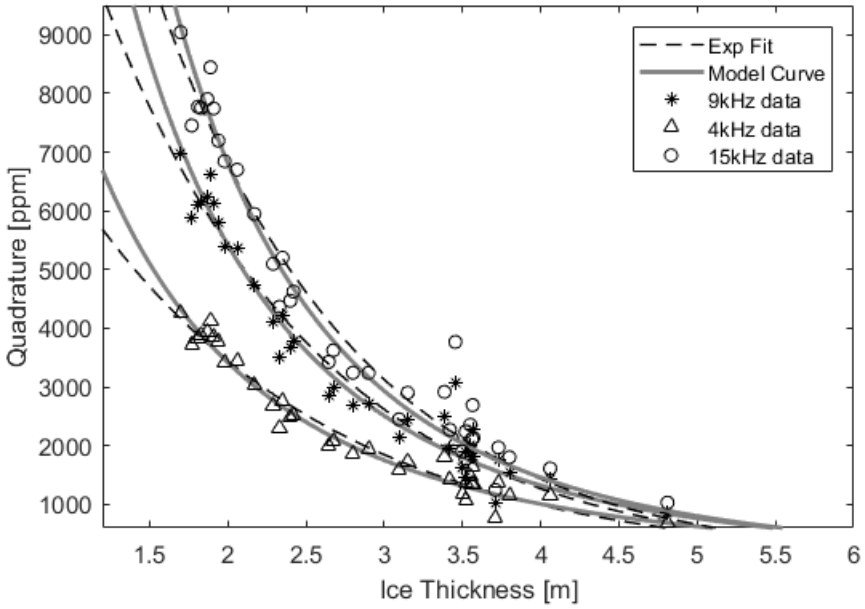

Figure 5.2.1.: EM data at drill sites for Quadrature values at 4 kHz, 9 kHz and 15 kHz versus ice thickness in comparison to model curves and exponential fits for each frequency.

As can be seen the model is as good a representation of the data as the exponential fit analysis. However, the forward model provides a better representation of the instrument response for ice thickness values beyond the range of thicknesses measured at the drill sites. In a cases where the ice thickness range at the drill sites is limited and for example only includes measurements between 1 m and 2 m ice thickness, the exponential fit can be vastly different from the model and not explain large thickness values sufficiently.

5.2.2. Inphase Calibration using Inversion

Real sea ice is often more complex than only one layer of snow and ice with negligible conductivity. To account for a more differentiated and realistic sea ice structure more complex models are needed. However, to invert those models with multiple layers of different conductivities and thicknesses without having an undetermined system (less measurement parameters than model parameters to be resolved, i.e. conductivities and thicknesses of sea ice layers), more measurement parameters are needed. Therefore, it is important to use every measurement parameter available.

While the Quadrature output of the EMP is calibrated and immediately fits the model, the Inphase is not. A behaviour frequently observed with a variety ground based EM instruments. To use the Inphase output for ice thickness inversion, it first has to be calibrated to be comparable with the pre-calculated models. Since the Inphase calibration can be different for each EM instrument , therefore, only the calibration for the EMP-400 is discussed here. Since the behaviour of the Inphase versus ice thickness is non-linear and different for every frequency, the Inphase is calibrated separately for each frequency by applying a gain g on the Inphase data from the drill sites according to:

$$I_{f,c} = g \cdot I_f \,, \tag{5.2.1}$$

with I_f as the Inphase for each frequency f and $I_{f,c}$ as the calibrated Inphase for f.

Figure 5.2.2 displays the steps taken as part of the calibration of the Inphase. Model and EM drill hole data are entered into a loop, in which the gain applied on the Inphase is being changed and the inversion repeated as well as the RMSE calculated for each gain used. Then the minimum RMSE is determined and the according gain chosen as the final gain for the calibration of the Inphase.

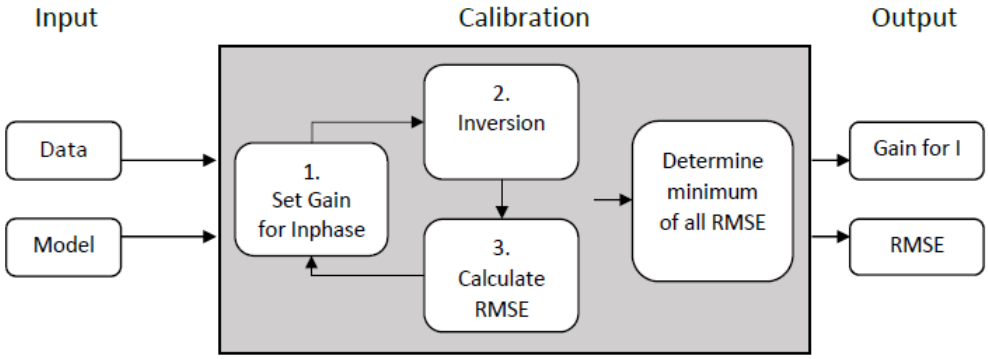

Figure 5.2.2.: Flowchart displaying the steps involved in the calibration of the Inphase. EM data from the drill sites and a model are input into the calibration loop, that adjusts the gain g applied on the Inphase, inverts ice thickness values and calculates the RMSE for each g applied. Then the minimum RMSE between data and model is determined, resulting in the output of the optimal gain and the RMSE between modelled and measured thickness values.

The inversion, which is done as part of the Inphase calibration uses the minimum distance calculation according to Equation 4.3.1 which includes Inphase and Quadrature. Depending on instrument characteristics, like coil distance and frequency as well as thickness measurement range, the Quadrature component can be more than twice as large as the Inphase i.e the Quadrature at an ice thickness of 1.4 m is 10000 while the Inphase at the same thickness is only 5000. Therefore the Quadrature can potentially distort the results of the Inphase calibration towards finding the best fit between measured and modelled ice thicknesses for the Quadrature rather than the Inphase. This effect can be reduced by applying a weight w on the Quadrature part of the distance calculation being used in the Inversion.

The distance d is then estimated with the gain g applied on the Inphase data and the weight w on the Quadrature as:

$$d = \sqrt{(g \cdot I_{obs} - I_e)^2 + w \cdot (Q_{obs} - Q_e)^2}. \tag{5.2.2}$$

As explained in Chapter 3, the inversion then finds the minimum of d by searching the complete model space and determines the with I_e and Q_e paired ice thickness values for each data point. Furthermore, the RMSE is calculated according to Equation 4.3.5 (Chapter 4) for each gain applied. The models used for the Inphase calibration are simple three-layer-models: air, sea ice, and sea water, with sea ice thickness being the only changing parameter. Therefore, Equation 4.3.5 only has to be calculated for LT1 with NL=1 to determine the RMSE.

The gain which results in the smallest RMSE is then chosen as a calibration factor for the Inphase of that frequency and the model used and can be applied to all Inphase measurements of that frequency. The gain for all models was varied from 0 to 2 in 0.01 increments. It is worth noting that the gain of the Inphase is specific to the model its being calibrated with, so each model will cause a different resulting gain and RMSE.

To determine the weight w applied on the Quadrature components within the distance equation several steps were taken. First the average sea ice thickness (here combined sea ice and snow thickness) for the drill hole data was calculated. Then the ppm values at that average thickness for Inphase and Quadrature were determined from the model being used for calibration. Finally, the weight is determined as the ratio between those average Inphase and Quadrature ppm values. Table 5.2.1 shows an overview of the values calculated for the mentioned steps and other calibration values determined for the Alert data set.

Frequency	I_f(2.96 m) [ppm]	Q_f(2.96 m) [ppm]	$w = \frac{I_f}{Q_f}$	RMSE [m]	g for I_f
4 kHz	1190	1795	0.66	0.2418	0.75
9 kHz	2331	2581	0.90	0.2898	1.24
15 kHz (<3.5 m)	3333	3024	1.10	0.2363	1.47

Table 5.2.1.: RMSE results and gain as well as weights applied for Inphase calibration of Alert 2013 data set.Weights applied on Q during Inphase calibration are calculated based on I and Q model values for average ice thickness of drill hole data set for frequencies of 4 kHz ,9kHz and 15 kHz. For the calibration of the 15 kHz data set only drill sites with ice thicknesses < 3.5 m were used.

As mentioned before, weights and gains as part of the Inphase calibration have to be determined separately for each frequency. Figure 5.2.3 show the RMSE and resulting g calculated as part of the Inphase calibration of the 9kHz data of the Alert data set.

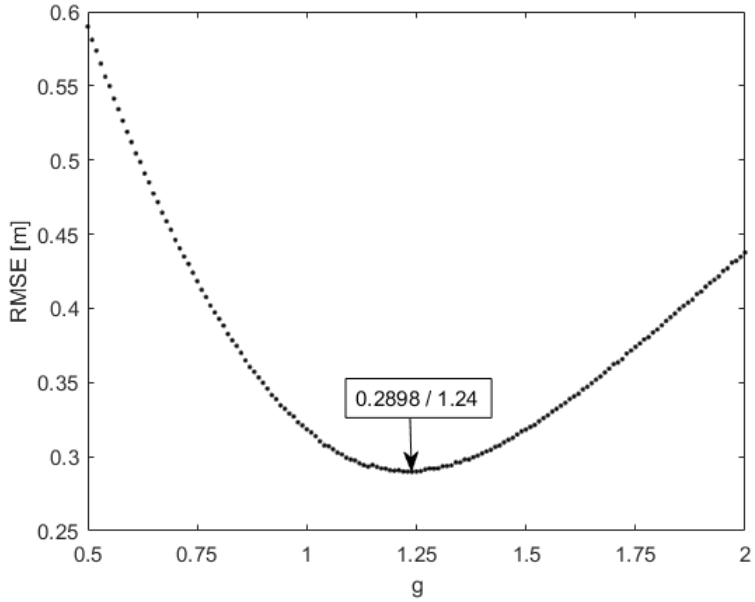

Figure 5.2.3.: RMSE versus gain g values for Inphase calibration of 9 kHz Alert EM data. The final gain g of 1.24 is chosen from the minimum RMSE of 0.2898 m.

Figure 5.2.4 displays the Alert Inphase drill hole data before and after calibration in comparison to the expected Inphase model values. The Models for all three frequencies

have a changing ice layer with a conductivity of 0 mS/m and a sea water conductivity of 2400 mS/m at a resolution of 1 cm. This model was chosen because of its good fit with the Quadrature, as can be observed in Figure 5.2.1.

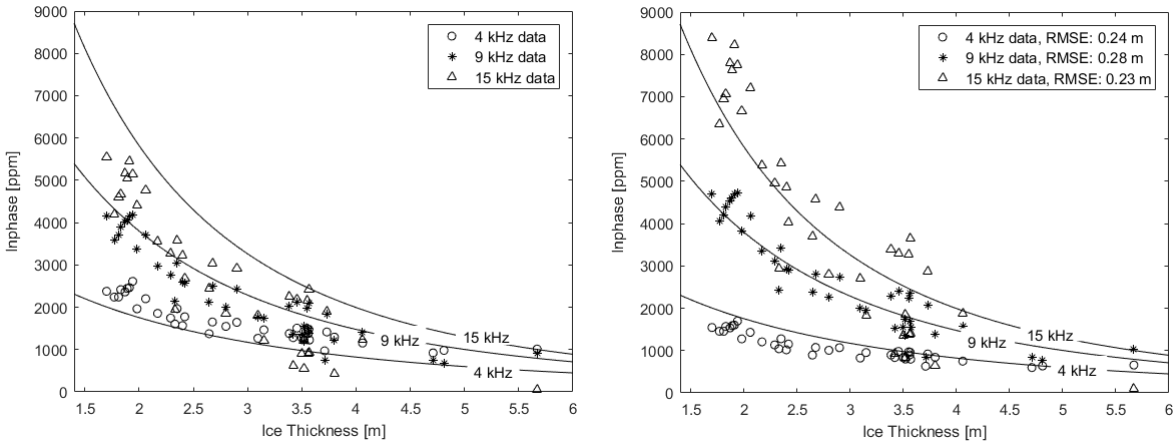

Figure 5.2.4.: Alert EM Inphase data measured at drill sites in comparison to 1D model Inphase for 4 kHz, 9kHz and 15 kHz in solid lines before (left) and after (right) calibration of Inphase.

The data from Alert is dominated by MYI with relatively high ice thickness values and an average thickness of 2.89 m. Therefore, the 15kHz data proved to be difficult to calibrate when using the full drill hole data set and no satisfactory calibration could be achieved. At a thickness of over 3.5 m the data becomes very noisy and sensitivity limits are reached. This is due to the Inphase and Quadrature decreasing exponentially with increasing thickness (see Figure 5.2.1 and 5.2.4) and differences in ppm values getting smaller and the noise to signal ratio getting bigger. Therefore, only data values for thicknesses of under 3.5 m were used for the Inphase calibration of the 15kHz data set.

For the calibration of the Inphase of the Qikiqtarjuaq data set one extra step had to be taken. Since this data set was collected over thin first year ice with a wet snow cover, it can be assumed that the conductivity of the ice and snow layer is above 0 mS/m [Haas et al., 1997]. Therefore, to calibrate the Inphase the model that fits the Quadrature data best has to be found. As a result, the inversion of the Quadrature

data was done for a set of models with different snow and ice layer conductivities. Here the Quadrature data of all frequencies is inverted together as explained in the next section of this chapter. Table 5.2.2 shows an overview of the RMSE resulting from the Inversion of the Quadrature data for three-layer 1D models with an instrument height of 10 cm, changing sea ice plus snow conductivity between 0 mS/m and 70 mS/m using a a sea water conductivity of 2500 mS/m. 44 drill hole measurements were used only including sites which showed snow and ice layers and no slush.

Sea Ice Conductivity [mS/m]	RMSE [m]
0	0.1076
10	0.0977
20	0.0892
30	0.0825
40	0.0766
50	**0.0731**
60	0.0741
70	0.0791

Table 5.2.2.: RMSE results for inversion of Qikiqtarjuaq data using models with conductivities for the ice and snow layer ranging from 0 - 70 mS/m.

The model with a sea ice plus snow conductivity of 50 mS/m results in the lowest RMSE and therefore the best fit with the Quadrature data was then used for the calibration of the Inphase. The weights applied on the Quadrature during the inversion step of the calibration are based on the chosen model. The average total thickness of ice and snow (TT) for 44 drill holes used was 1.42 m with values ranging from 1.1 m to 1.7 m. Resulting weights for the Quadrature as well as gains for the Inphase and according RMSE values are displayed in Table 5.2.3.

Frequency	I_f(1.42 m) [ppm]	Q_f(1.42 m) [ppm]	$w = \frac{I_f}{Q_f}$	RMSE [m]	g for I_f
5 kHz	3094	6973	0.44	0.0715	0.69
10 kHz	6261	10850	0.58	0.0693	0.7
15 kHz	9113	13580	0.67	0.0701	0.71

Table 5.2.3.: RMSE results and gain as well as weights applied for Inphase calibration of Qikiqtarjuaq 2017 data set.Weights applied on Q during Inphase calibration are calculated based on I and Q model values for average ice thickness of drill hole data set for frequencies of 5 kHz ,10 kHz and 15 kHz.

The Qikiqtarjuaq data were collected over thin FYI while the Alert data were collected mostly over thicker MYI, therefor the Inphase and Quadrature values of the Qikiqtarjuaq data set are much higher than from the Alert data set (compare Table 5.2.3 and Table 5.2.1). The data from Qikiqtarjuaq with thinner sea ice also has higher Inphase and Quadrature values than the Alert data, with the Quadrature being about two times as big as the Inphase. Since there is a great difference between the Quadrature and Inphase values and therefore, the error range connected to both, the weight applied on the Quadrature within the minimum distance calculated after Equation 5.2.2 for the Qikiqtarjuaq data was necessary in order to get a reasonable result for the Inphase calibration. Figure 5.2.5 shows the Qikiqtarjuaq Inphase data at the drill sites before and after calibration in comparison to the 1D model Inphase returns with an ice layer conductivity of 50 mS/m and a sea water conductivity of 2500 mS/m for the 3 measurement frequencies of 5kHz, 10 kHz and 15kHz. This model therefore uses higher sea ice and sea water conductivities than the one used for the calibration of the Alert data set as shown in Figure 5.2.4 and Table 5.2.1 with a sea ice conductivity of 0 mS/m and sea water conductivity of 2400 mS/m.

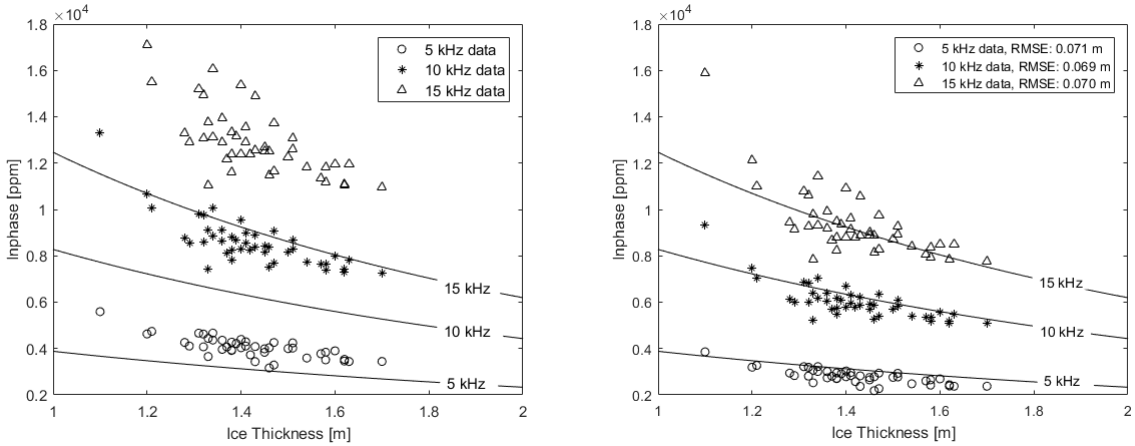

Figure 5.2.5.: Qikiqtarjuaq EM Inphase data measured at drill sites in comparison to 1D model Inphase for 5 kHz, 10 kHz and 15 kHz in solid lines before (left) and after (right) calibration of Inphase.

Since all measured uncalibrated Inphase values shown in Figure 5.2.5 lie above the modelled values, the gain to be applied on the Inphase must be below 1. As Table 5.2.3 shows all the resulting calculated gains end up as expected as values close to 0.7.

The weight values shown in Table 5.2.3 lie all around 0.5. To test the sensitivity of the calibration to the ratio between Inphase and Quadrature used as weight on the Quadrature component, the calibration was run for all frequencies with the weights set to 0.5. Results displayed in Appendix C.1 show that although the RMSE values are slightly better for the real calculated I/Q ratio, the resulting gains for the Inphase are still the same. This in turn means as long as the weights lie within the right range they do not necessarily have to be calculated as accurately as shown in Table 5.2.3 and Table 5.2.1 to determine the correct calibration factor for the Inphase. Small changes in the weight factor have therefore no significant impact on the calibration results.

5.3. Multi Frequency Inversion

To resolve the thickness or conductivity of more than one layer the Quadrature and Inphase data of all three frequencies are used within a multi frequency brute force inversion. Since the Inphase is not always calibrated the Inversion can be done by only using the Quadrature data of all three frequencies. The Inversion is then run by finding the minimum of distance d after Equation 4.3.4 and with it the best fit between modelled and measured data. When the Inphase data are calibrated, they can be used as part of the Inversion and then Equation 4.3.2 is used to calculate d using Inphase and Quadrature measurements for all frequencies.

The inversion can reproduce ice thicknesses 100% when supplied with clean forward model data, but real data is usually not clean and has some instrument noise, meaning the inversion is only an approximation of the true sea ice conditions. To test the performance of the inversion with noisy data several model studies were conducted in the following to show how well ice thickness and snow data can be resolved at a certain instrument noise level.

While the Alert data were collected over MYI and thick FYI with an average total ice and snow thickness of 2.89 m and dry snow, the Qikiqtarjuaq data were collected over young FYI covered with wet snow and slush and an average total snow and ice thickness of 1.11 m. Since the two data sets used in this chapter show very different sea ice properties, model studies were done for each case accounting for the different sea ice conditions. The results and quality of the resolution of the different sea ice and snow layers can therfore vary dependant on the consditions.

5.3.1. Three-Layer-Model Results

The three-layer-model as shown in Figure 5.3.1 assumes a model space with the 3 layers air, sea ice and sea water. In this case snow is regarded as part of the sea ice layer. The thickness of the sea ice plus snow layer is in the following referred to as total thickness (TT). In the three-layer case the sea ice thickness is the only changing model parameter.

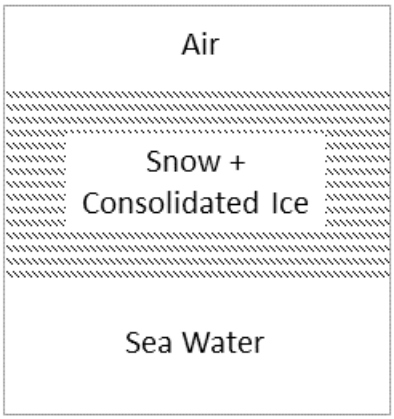

Figure 5.3.1.: Three-layer 1D model with the 3 layers air, sea ice and sea water. Snow is regarded as part of the consolidated ice layer. Within ODFEM the air layer is set as instrument height. The only layer changing in thickness is the snow plus consolidated ice layer.

5.3.1.1. Results for thick rough MYI

Figure 5.3.2 shows the results of the inversion of 10,000 modelled Inphase and Quadrature returns with a randomly created artificial noise of 5% for 3 frequencies of 4 kHz, 9 kHz, and 15kHz. The models represent the ice conditions prominent in the Alert sea ice campaign, with 3 layers of air, ice and sea water. The conductivity for ice and snow were set to 0 mS/m, sea water conductivity was set to 2400 mS/m. Instrument height was set to 10 cm and ice thickness was varied from 0 to 12 m at a resolution of 0.01 m. The inversion was done once with only using Quadrature for all 3 frequencies and once with both Inphase and Quadrature for all frequencies.

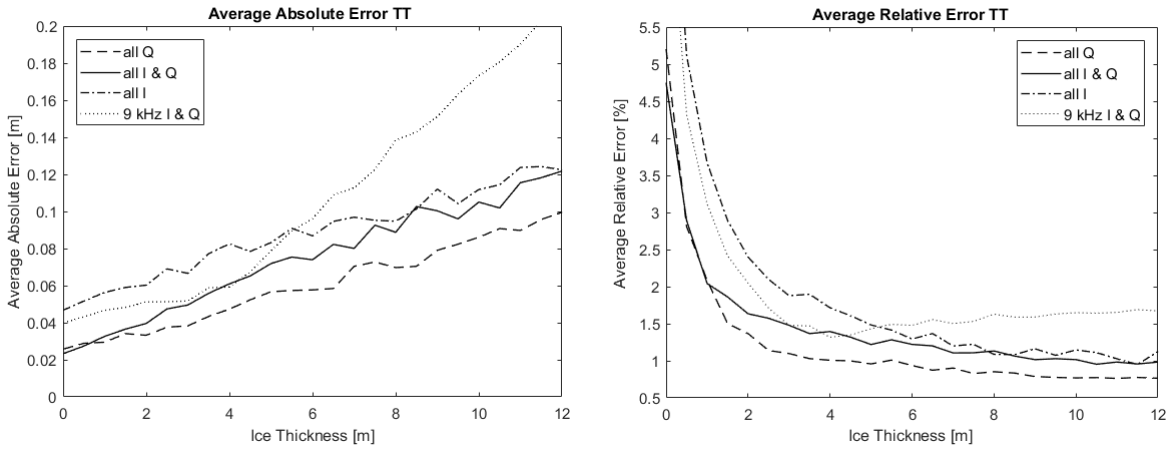

Figure 5.3.2.: Error study on three-layer-model inversion results of 10,000 modelled Inphase and Quadrature values with 5% noise applied. Displayed are the average differences over 0.5 m increments between modelled and inverted total ice thicknesses (TT) for inversions with different input parameters for the 3 frequencies 4 kHz, 9 kHz and 15 kHz. Left: absolute errors, Right: relative errors. Input model parameters include an instrument height of 10 cm, sea water conductivity of 2400 mS/m and sea ice conductivity of 0 mS/m at a resolution of 1 cm.

The results of the error study for the three-layer case in Figure 5.3.2 shows both average absolute and relative differences between the input and inverted values. Since the model used has a very clear sharp conductivity contrast between 0 mS/m for the ice and 2400 mS/m for the sea water, the multi frequency inversion allows for very accurate resolution of the ice thickness with the absolute error staying under 0.2 m at an instrument noise level of 5%. It can be seen that the Inphase is more effected by the noise than the Quadrature and therefore,in this specific case, produces the worst results. That also has the effect that using both Inphase and Quadrature within the inversion leads to worse results in comparison to only using Quadrature. Figure 5.3.2 also shows that the multi-frequency inversion results are better than single-frequency results. That effect is more prominent at larger ice thicknesses.

Real instrument measurements can have other noise sources than just instrument noise, like uneven terrain resulting in instrument roll and pitch or metal within the vicinity if the instrument from operator or snowmobiles. Errors can also be introduced by

more complex ice conditions like sea water inclusions in ice pockets of deformed ice. Figure 5.3.3 displays the results of the inversion of the Alert drill hole data using both Quadrature and calibrated Inphase values in comparison to the in situ measured thickness values.

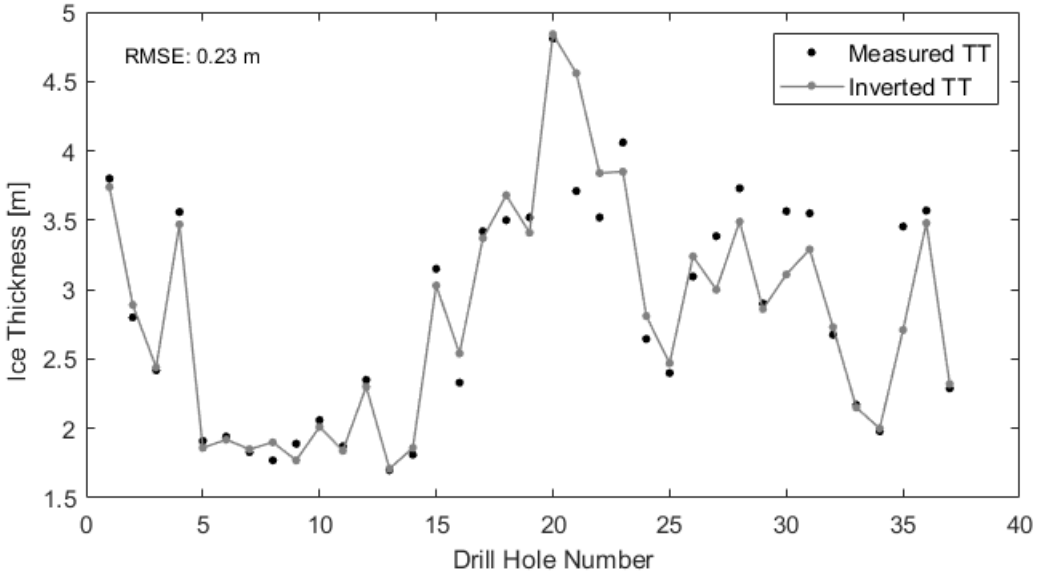

Figure 5.3.3.: Total ice thickness (TT) results of three-layer-model inversion using I and Q of 4 kHz, 9 kHz and 15 kHz Alert data compared to drill hole total ice thickness measurements. Model parameters include an instrument height of 10 cm, sea water conductivity of 2400 mS/m and sea ice conductivity of 0 mS/m at a resolution of 1 cm.

Overall the inversion is able to reproduce the drill hole data well at an RMSE of 0.23 m for the total ice thickness. Disagreement between measured thicknesses and inverted thickness values increases at larger ice thicknesses of over 3 m. Once the quality of inverted ice thicknesses has been determined as for the drill sites using the RMSE, the inversion can be applied on any EM data set collected under the same conditions and in the same area.

Inverted ice thickness results from a multi-frequency inversion using only Quadrature (RMSE = 0.22 m) for the Alert data set have been successfully used in a study about algea growth under multi-year ice by Lange et al. (2017). The ice thickness results were

instrumental in showing that the role of thick sea ice as a biological habitat for algea growth have been previously underestimated.

5.3.1.2. Results for thin level FYI

The sea ice near Qikiqtarjuaq is first year landfast ice and thinner than at Alert. As explained in Section 5.2.2, a model with a conductive snow and ice layer of 50 mS/m fits the data best. An error study was performed using models with a sea ice conductivity of 50 mS/m, sea water conductivity of 2500 mS/m at an instrument height of 10 cm and a resolution of 1 cm. These models were calculated for the three measurement frequencies of 5 kHz, 10 kHz and 15kHz. Figure 5.3.4 shows the absolute and relative differences between the expected ice thicknesses and inverted ice thicknesses from modelled values with an artificial noise of 5%. Displayed are the average errors calculated from 10,000 data points for the inversion using only Quadrature and using both Quadrature and Inphase of all frequencies.

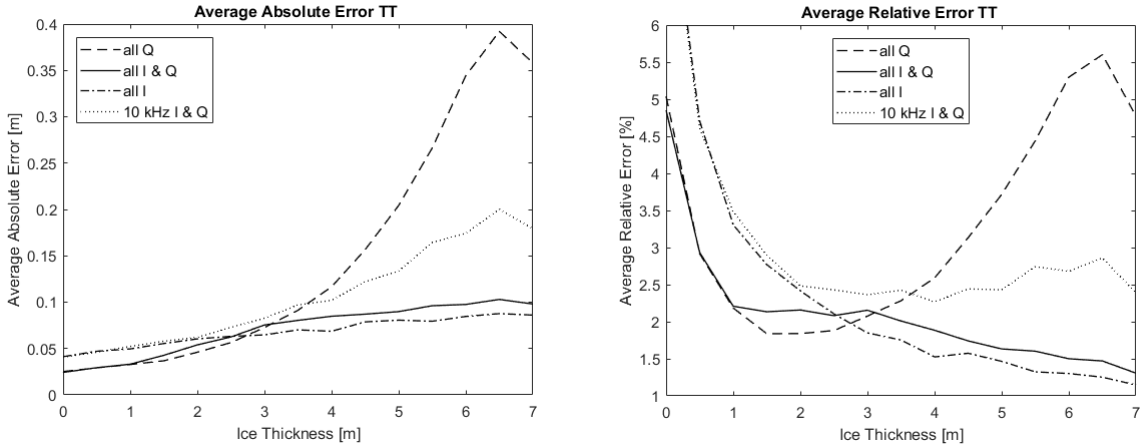

Figure 5.3.4.: Error study on three-layer-model inversion results of 10,000 modelled Inphase and Quadrature values with 5% noise applied. Displayed are the average differences over 0.5 m increments between modelled and inverted total ice thicknesses (TT) for inversions with different input parameters for the 3 frequencies 4 kHz, 9 kHz and 15 kHz. Left: absolute errors, Right: relative errors. Input model parameters include an instrument height of 10 cm, water conductivity of 2500 mS/m and sea ice conductivity of 50 mS/m at a resolution of 1 cm

The results of the error study in Figure 5.3.4 show an increase in error at 3.5 m ice thickness when only using Quadrature for the multi-frequency inversion since in this case the Quadrature is more sensitive to noise than the Inphase in that thickness range. However, including the Inphase in the inversion can greatly reduce the influence of noise on the inverted ice thickness. Multi frequency results show an overall better performance than single-frequency results when using both Inphase and Quadrature in the inversion.

Results of the inversion of the drill hole data set with the same model as the one used for the error study in Figure 5.3.4 using both the Quadrature and calibrated Inphase, are displayed in Figure 5.3.5.

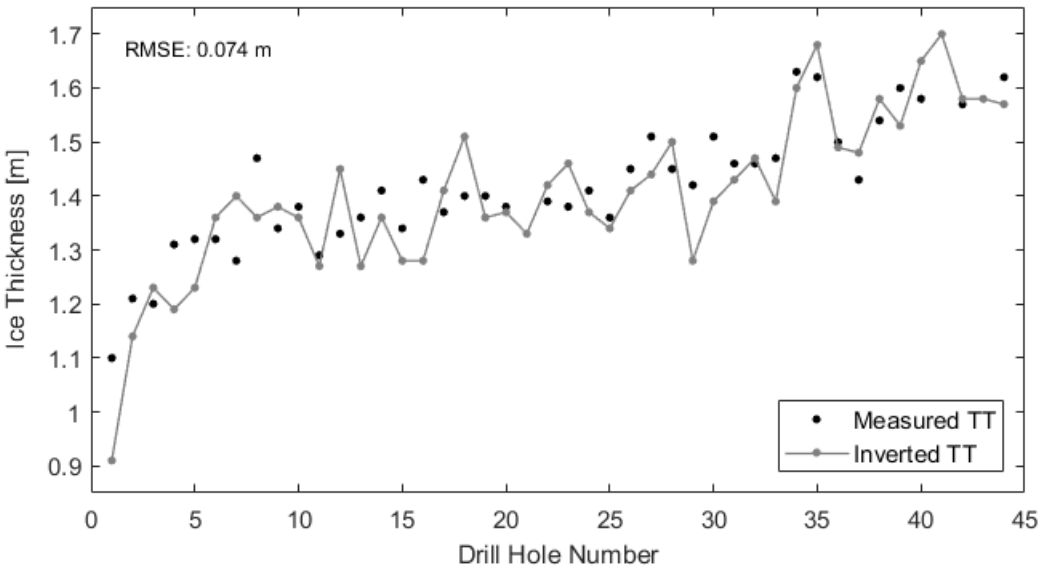

Figure 5.3.5.: Total ice thickness (TT) results of three-layer-model inversion using I and Q of 5 kHz, 10 kHz and 15 kHz Qikiqtarjuaq data compared to drill hole total ice thickness measurements. Model parameters include an instrument height of 10 cm, water conductivity of 2400 mS/m and ice conductivity of 50 mS/m at a resolution of 1 cm

The inversion reproduces the data well with an RMSE of 0.0742 m for the total ice thickness. For this inversion 44 drill hole locations were used that didn't visibly show any slush.

5.4. Using Multi-Frequency Inversion to Resolve a Slush Layer

A big part of the sea ice in the study area near Qikiqtarjuaq was covered by a prominent slush layer, which is a saline and saturated moist basal snow layer. This porous, slushy layer is commonly observed in Antarctica but has been observed in the Arctic as well. Slush is composed of a mixture of brine and ice crystals and can contain a high proportion of fluid of 50% or greater [Fritsen et al., 2001]. Slush layers can be caused by flooding of snow at the snow/ice interface due to high snow loading, ridging and rafting of ice floes or by the melting of near-surface sea ice due to inverted summertime temperature gradients as has been observed in Antarctica [Ackley et al., 2008]. However, EM induction wouldn't be sensitive to the latter type of slush. The brine on the surface of the ice can over time be wicked up further into the snow by capillary suction [Massom et al., 1998, 2001]. Brine and seawater supply are determined by snow depth, ice deformation as well as ice temperature and salinity [Golden et al., 1998; Massom et al., 2001].

Slush layers play a significant ecological role in the Southern Ocean, providing a habitat for sea ice algea [Saenz and Arrigo, 2012]. Furthermore, the freezing of slush layers results in rejection of dense brine which induces convection within the ice, replacing rejected brine with nutrient- rich sea water from the upper ocean [Lytle and Ackley, 1996], in turn increasing algea growth in sea ice algea communities during freeze up [Fritsen et al., 1994].

A direct impact of slush and wet snow is a change in the dielectric and microwave scattering properties (including albedo) of the snow surface which leads to strong microwave attenuation within the snow volume, significantly reducing radar penetration. Additionally with heavy snow loads the freeboard of the ice becomes 0 or even negative so that the isostatic concept cannot be applied to calculate sea ice thickness from free-

board. These effects complicate sea ice thickness measurements using remote sensing methods applied on satellites like CryoSat-2 [Nandan et al., 2017].

The slush observed around Qikiqtarjuaq was mostly caused by sea water flooding caused by heavy snow loads. Within this area it directly effects the local population since traveling over slush on sea ice becomes significantly more difficult and dangerous. People traveling by means of snow mobile can easily get stuck in the deep wet layer and can take hours to days to get out of it. This not just delays travel but also poses an unpredictable hazard when people have to stay outside for unpredictable amounts of time and possibly without sufficient supplies or provisions.

Establishing a remote sensing method for measuring slush will therefore be a big step towards further researching the satellite signature of snow as well as the ecological and direct impact of slush.

5.4.1. Four-Layer-Model Results

The first approach chosen to resolve the slush layer on top of sea ice, was based on a four-layer-model with a combined snow and slush layer on top of the sea ice as shown in Figure 5.4.1. The models used for the inversion included an instrument height of 10 cm, a combined slush and snow layer with changing conductivities over several model runs, a consolidated sea ice layer with a conductivity of 50 mS/m, and a sea water layer with a conductivity of 2500 mS/m at a resolution of 1 cm for the 3 frequencies of 5 kHz, 10 kHz and 15kHz.

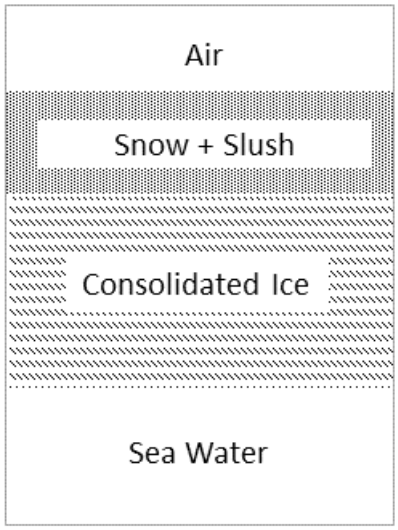

Figure 5.4.1.: four-layer 1D model with the 4 layers air, snow, sea ice and sea water. Slush is regarded as part of the snow layer. Within ODFEM the air layer is set as instrument height. The snow plus slush layer as well as the consolidated ice layer are changing in thickness within this model.

To determine the model parameters and for the validation of the inversion with the four-layer-model 85 drill hole values were used of which 41 had a slush layer and 44 had no noticeable slush. The inversion was done for a set of 1D models with slush conductivities changing from 500 - 1900 mS/m by using only Quadrature responses as well as a combination of Quadrature and calibrated Inphase. The gains used on the Inphase were determined by the three-layer-model Inphase calibration for a sea ice conductivity of 50 mS/m as displayed in Table 5.2.3 using a data set in which slush wasn't present. RMSE results of the inversion using only Quadrature returns for the total slush and ice thickness (TT) as well as RMSE for slush and consolidated ice for all model runs can be found in Table 5.4.1 and according RMSE results for using both Inphase and Quadrature are displayed in Appendix C.2. For the total ice thickness all RMSE values lie around 0.3 m, representing a minimum of 15% error considering all total thicknesses of the drill hole data set are below 2 m at an average thickness of 1.11 m .

σ_{Slush} [mS/m]	RMSE TT [m]	RMSE Slush [m]	RMSE Snow [m]
500	0.3292	0.3345	0.3240
600	0.3303	0.3355	0.3251
700	0.3309	0.3370	0.3249
800	0.3324	0.3387	0.3260
900	0.3313	0.3373	0.3253
1000	0.3315	0.3374	0.3257
1100	0.3359	0.3420	0.3298
1200	0.3360	0.3432	0.3287
1300	0.3365	0.3426	0.3305
1400	0.3423	0.3524	0.3323
1500	0.3313	0.3373	0.3253
1600	0.3398	0.3479	0.3316
1700	0.3402	0.3481	0.3323
1800	0.3394	0.3461	0.3327
1900	0.3406	0.3460	0.3352

Table 5.4.1.: RMSE results for inversions with four-layer-model with changing snow plus slush layer conductivity σ_{Slush} of Qikiqtarjuaq drill hole EM data using only Q of 5 kHz, 10 kHz and 15 kHz data. Model parameters include an instrument height of 10 cm, water conductivity of 2500 mS/m and ice conductivity of 50 mS/m at a resolution of 1 cm.

Figure 5.4.2 shows the inverted total thickness using only Quadrature for a four-layer slush model with a slush conductivity of 900 mS/m in comparison to the drill hole measurements.

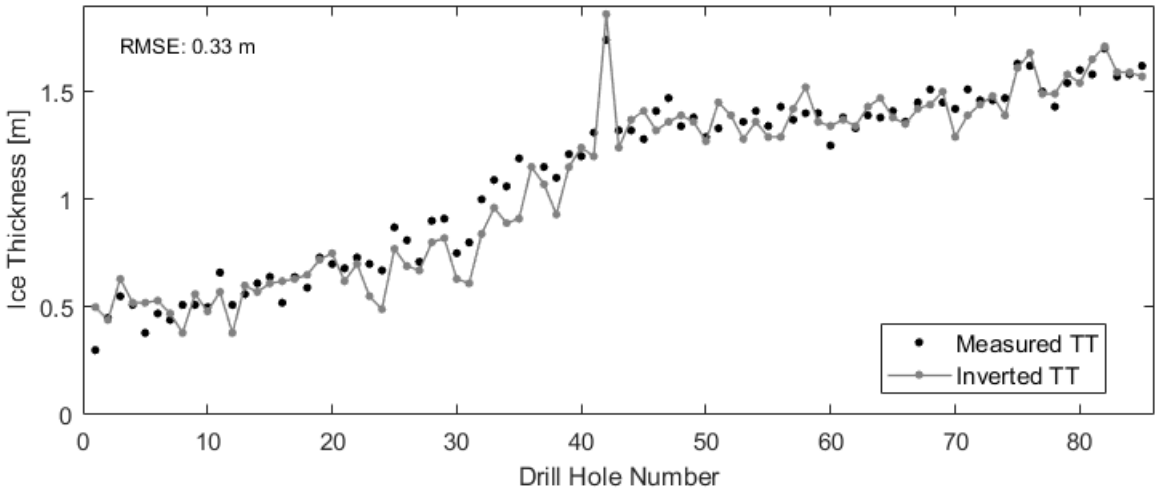

Figure 5.4.2.: Total ice thickness (TT) results of four-layer-model inversion using only Q of 5 kHz, 10 kHz and 15 kHz Qikiqtarjuaq data compared to drill hole total ice thickness measurements. Model parameters include an instrument height of 10 cm, water conductivity of 2500 mS/m and ice conductivity of 50 mS/m and a snow plus slush conductivity of 900 mS/m at a resolution of 1 cm.

The RMSE for the total thickness in Figure 5.4.2 is 0.33 m and as can be seen in Figure 5.4.3 the RMSE value for the snow and slush layer also lies at 0.33 m. For the slush plus snow layer with an average thickness of the drill hole data of 0.36 m that RMSE is very high and indicates deviations between inverted and measured values of up to 100 %.

Figure 5.4.3 displays the inverted slush plus snow layer thickness in comparison to the measured combined slush and snow drill hole values, as well as to the observed slush values from the drill sites. It clearly shows that the inverted layer supposed to resolve the combined snow and slush thickness more resembles the measured slush layer but doesn't reflect the amount of snow on top of it. This indicates that the data set is sensitive to an existing slush layer, but also that a four-layer-model representation with a combined snow and slush layer is not the right solution to invert the given data sufficiently. The resulting bulk conductivity for the snow plus slush layer lies way below the expected slush layer conductivity which is due to snow commonly having a very

low conductivity. Under the assumption that there is a big spread between snow and slush layer conductivities, inversion results for the bulk conductivity of the snow plus slush layer highly depend on the amount of snow on top of the slush and therefore, cannot be resolved reliably with a four-layer-model. A more complex five-layer-model is therefore needed to resolve snow and slush layer thicknesses as well as the slush layer conductivity separately.

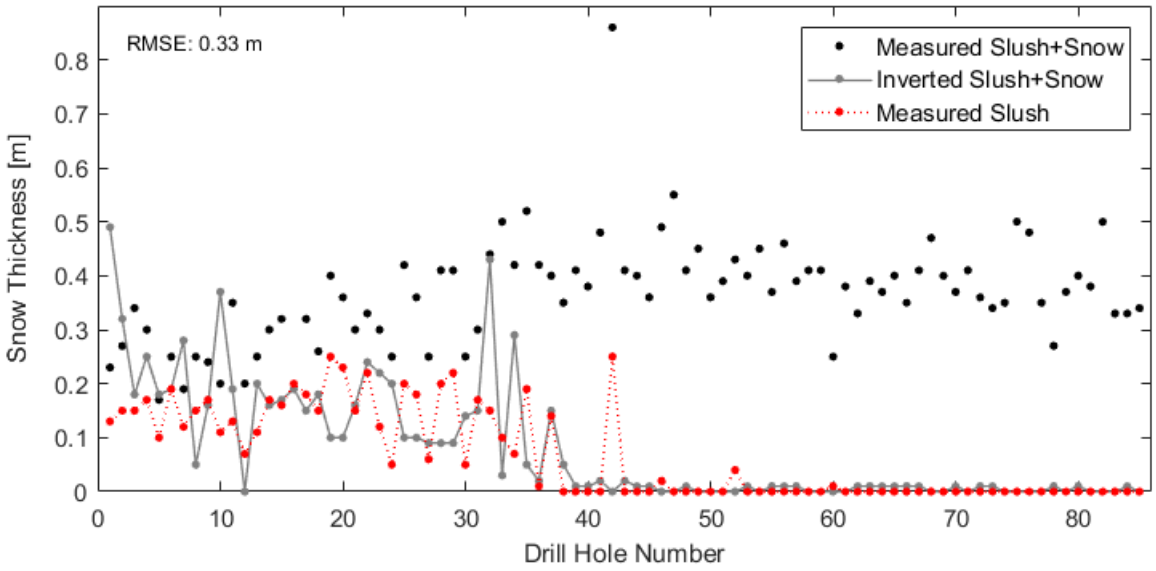

Figure 5.4.3.: Slush plus snow thickness results of four-layer-model inversion using only Q of 5 kHz, 10 kHz and 15 kHz Qikiqtarjuaq data compared to drill hole snow and slush measurements. Model parameters include an instrument height of 10 cm, water conductivity of 2500 mS/m and ice conductivity of 50mS/m and a snow plus slush conductivity of 900 mS/m at a resolution of 1 cm

5.4.2. Five-Layer-Model Results

The slush layer can be sufficiently resolved using a five-layer-model for the thickness inversion of snow, slush and sea ice. The five-layer-model chosen to resolve slush and snow thickness, as well as slush conductivity, is displayed in Figure 5.4.4. They constitute an air layer on top whose thickness is set by instrument height, a snow layer on top of a slush layer, followed by a sea ice layer, and finally a layer for sea water.

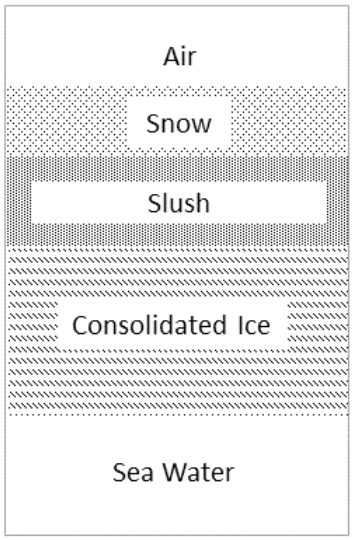

Figure 5.4.4.: Five-layer 1D model with the 5 layers air, snow,slush,sea ice and water. Slush is regarded as part of the snow layer. Within ODFEM the air layer is set as instrument height. The snow layer, slush layer and the consolidated ice layer are changing in thickness within this model.

5.4.2.1. Results

For the inversion of snow, slush, and ice thickness a five-layer-model set with 10 cm instrument height, sea water conductivity of 2500 mS/m, and a resolution of 2 cm was calculated for the frequencies 5 kHz, 10kHz and 15 kHz. To determine the slush conductivity the inversion was applied on model sets with changing slush conductivities of 800 - 2500 mS/m. Validation of the inverted snow, slush, and ice thicknesses was done determining the RMSE with Equation 4.3.5 using 85 drill hole measurements of

which 41 had a slush layer and 44 had no slush.

The Inphase calibration of the Qikiqtarjuaq data set described in Section 5.2.2 is based on a three-layer-model with a sea ice plus snow conductivity of 50 mS/m. This calibration might not be valid for the fice-layer case anymore, where snow and slush conductivities can lead to different bulk conductivities than assumed in the three-layer-model. The inversion based on Quadrature for a five-layer-model with a snow conductivity of 0 mS/m and a sea ice conductivity of 50 mS/m shows the overall best RMSE results displayed in Table 5.4.2. The following results have been produced using an inversion based only on the Quadrature components using Equation 4.3.4 described in Chapter 4.

RMSE results for using both Inphase (calibrated with the three-layer-model) and Quadrature for the same model set, as well as RMSE results for models with a snow conductivity of 50 mS/m and models with a sea ice conductivity of 0 mS/m can be found in Appendix C.3.

σ_{Slush} [mS/m]	RMSE TT [m]	RMSE Slush [m]	RMSE Snow [m]	RMSE Ice [m]
800	0.1792	0.0678	0.2117	0.2579
900	0.1811	0.0822	0.2075	0.2537
1000	0.1776	0.0745	0.2077	0.2507
1100	0.1766	0.0776	0.2066	0.2457
1200	0.1704	0.0724	0.1989	0.2399
1300	0.1736	0.0822	0.1969	0.2415
1400	**0.1659**	**0.0617**	**0.1968**	**0.2391**
1500	0.1751	0.0823	0.1987	0.2443
1600	0.1807	0.0820	0.2027	0.2575
1700	0.1746	0.0814	0.1985	0.2439
1800	0.1759	0.0702	0.2075	0.2499
1900	0.1780	0.0766	0.2037	0.2537
2000	0.1816	0.0765	0.2106	0.2578
2100	0.1813	0.0783	0.2103	0.2552
2200	0.1747	0.0717	0.2003	0.2520
2300	0.1736	0.0700	0.1977	0.2531
2400	0.1735	0.0615	0.2055	0.2534
2500	0.1815	0.0790	0.2062	0.2593

Table 5.4.2.: RMSE results for inversions with five-layer-models with changing snow plus slush layer conductivity σ_{Slush} of Qikiqtarjuaq drill hole EM data using only Q of 5 kHz, 10 kHz and 15 kHz data. Model parameters include an instrument height of 10 cm, water conductivity of 2500 mS/m and ice conductivity of 50 mS/m and snow conductivity of 0 mS/m at a resolution of 2 cm.

Table 5.4.2 shows that the model with a slush conductivity of 1400 mS/m has the best average RMSE of 0.1659 m for the total thickness (TT) of snow, slush and sea ice. Figure 5.4.5 shows the inverted total thickness results using only Quadrature for the model set resulting in the best RMSE with a snow conductivity of 0mS/m, slush conductivity of 1400 mS/m, and a sea water conductivity of 2500 mS/m in comparison to the in situ drill hole thickness measurements.

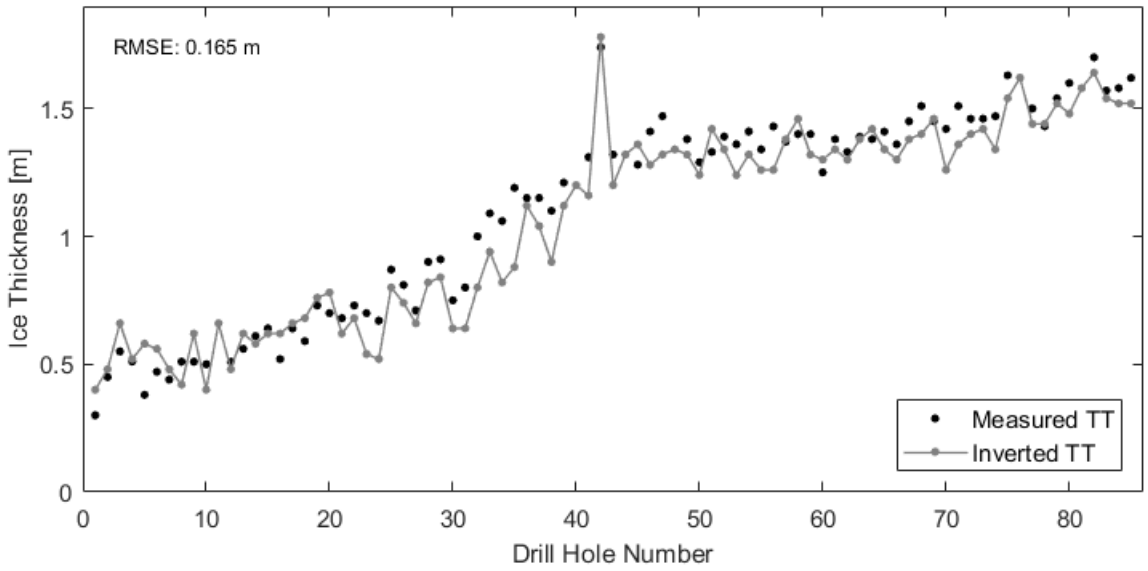

Figure 5.4.5.: Total ice thickness (TT) results of five-layer-model inversion using only Q of 5 kHz, 10 kHz and 15 kHz Qikiqtarjuaq data compared to drill hole total ice thickness measurements. Model parameters include an instrument height of 10 cm, water conductivity of 2500 mS/m and ice conductivity of 50 mS/m and snow conductivity of 0 mS/m at a resolution of 2 cm.

The total thickness results show an overall good agreement with the drill hole measurements over the whole thickness range observed. The results for the inverted thicknesses of the slush layer in comparison to the measurements at the drill sites are displayed in Figure 5.4.6. The slush thickness can be resolved very well with an RMSE of 0.0617 m. Finally, the results of snow thickness in comparison to the drill hole measurements are displayed in Figure 5.4.7. The snow layer on top (in the model on top of the slush but can also be zero) can not be resolved very well, with the RMSE being very high for the layer thickness at 0.1968 m.

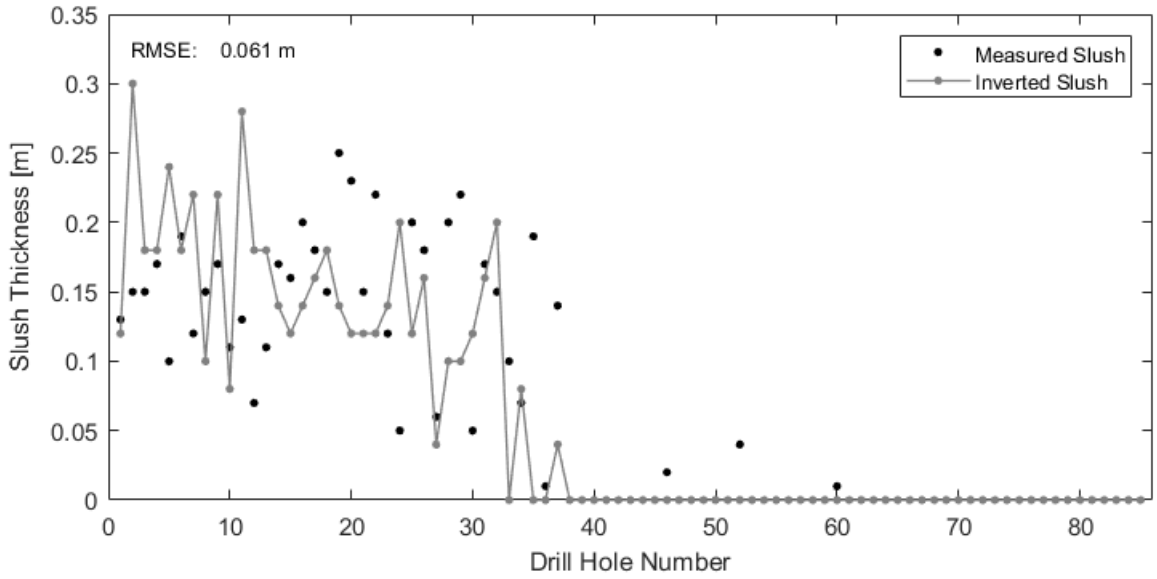

Figure 5.4.6.: Slush thickness results of five-layer-model inversion using only Q of 5 kHz, 10 kHz and 15 kHz Qikiqtarjuaq data compared to drill hole slush measurements. Model parameters include an instrument height of 10 cm, water conductivity of 2500 mS/m and ice conductivity of 50 mS/m and snow conductivity of 0 mS/m at a resolution of 2 cm.

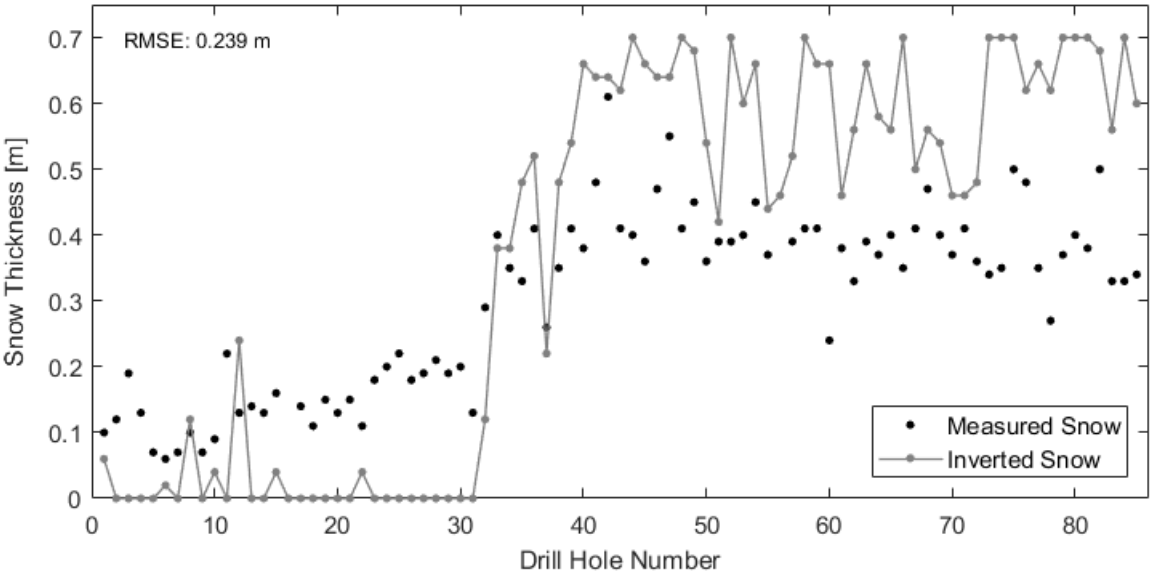

Figure 5.4.7.: Snow thickness results of five-layer-model inversion using only Q of 5 kHz, 10 kHz and 15 kHz Qikiqtarjuaq data compared to drill hole snow measurements. Model parameters include an instrument height of 10 cm, water conductivity of 2500 mS/m and ice conductivity of 50 mS/m and snow conductivity of 0 mS/m at a resolution of 2 cm.

Using a five-layer-model in combination with the brute force inversion provides good results overall for determining the total thickness of the ice as well as the thickness of the slush layer on top of the sea ice. However, this method does not resolve the snow layer on the surface very well. This is due to the slush layer affecting the electromagnetic field much more than the snow layer resulting in a reduced sensitivity to changes in the thickness of the snow layer.

5.4.2.2. Model Error study

To demonstrate the capabilities and limitations of the inversion for resolving the thickness of each layer in the five-layer-model, an error study was conducted for the model set, which provided the best inversion results for the Qikiqtarjuaq data.

The error study was performed using a model set with a snow conductivity of 0mS/m, slush conductivity of 50mS/m, sea ice conductivity of 50 mS/m, and sea water conductivity of 2500 mS/m. The models had an instrument height of 10 cm and a resolution of 2 cm and were calculated for measurement frequencies of 5 kHz, 10 kHz and 15 kHz. For the error study, an artificial noise of 5% was added to 10,000 randomly chosen modelled Quadrature values and inverted to snow slush and sea ice thicknesses. Then the average errors over 10 cm windows were calculated between modelled and inverted thickness values. Figure 5.4.8 shows the absolute and relative differences between the expected and inverted total ice thicknesses and the consolidated ice thicknesses.

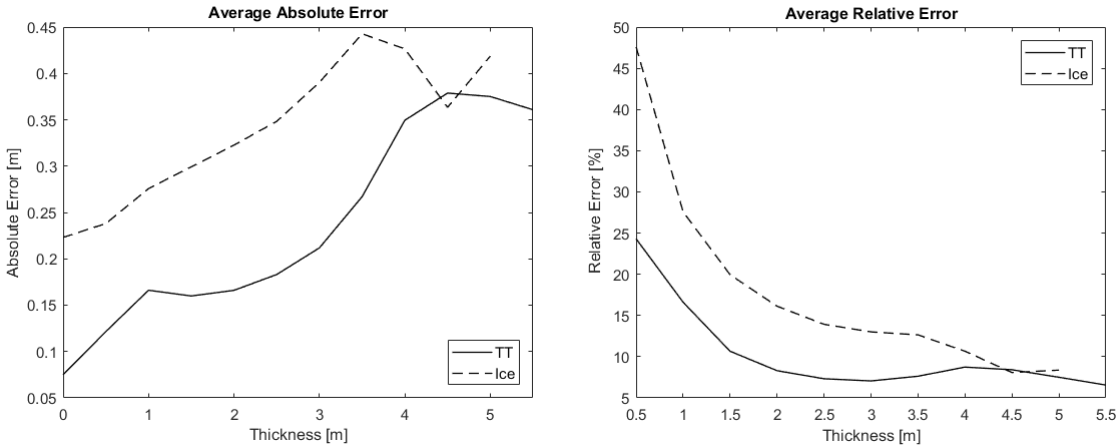

Figure 5.4.8.: Error study on five-layer-model inversion results of 10,000 modelled Quadrature values with 5% noise applied. Displayed are the average differences over 0.1 m increments between modelled and inverted total ice thicknesses (TT) and consolidated ice thicknesses for inversions with different input parameters for the 3 frequencies 5 kHz, 10 kHz and 15 kHz. Left: absolute errors, Right: relative errors. Input model parameters include an instrument height of 10 cm, water conductivity of 2500 mS/m and ice conductivity of 50 mS/m, slush conductivity of 1400 mS/m and snow conductivity of 0 mS/m at a resolution of 2 cm.

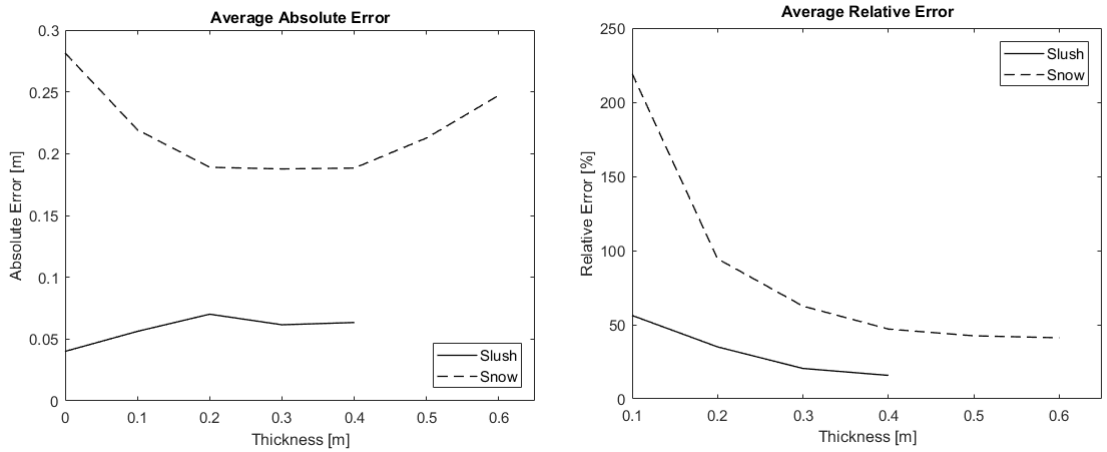

Figure 5.4.9.: Error study on five-layer-model inversion results of 10,000 modelled Quadrature values with 5% noise applied. Displayed are the average differences over 0.1 m increments between modelled and inverted slush and snow thicknesses (TT) for inversions with different input parameters for the 3 frequencies 5 kHz, 10 kHz and 15 kHz. Left: absolute errors, Right: relative errors. Input model parameters include an instrument height of 10 cm, water conductivity of 2500 mS/m and ice conductivity of 50 mS/m, slush conductivity of 1400 mS/m and snow conductivity of 0 mS/m at a resolution of 2 cm.

The error for the consolidated thickness is consistently higher by around 20 cm than the error for the total ice thickness of snow slush and ice. This means that an over or underestimation of the consolidated ice thickness is being corrected by the inverted thickness of slush and snow. Figure 5.4.9 shows the absolute and relative differences between the expected and inverted slush and snow thicknesses. While the slush thickness can be determined very well and errors lie around 5 cm, the snow thickness shows high absolute errors of 20 cm or more. Although the snow depth can not be determined very well, it can be seen that the error in snow thickness seems to offset the deviation in consolidated ice thickness resulting in overall good total thickness estimation with a relative error of under 10% at total ice thicknesses of over 1.5 m (see Figure 5.4.8).

5.5. Conclusion

Slush is a saline saturated moist basal snow layer on top of the ice that plays a significant ecological role as a habitat for ice algea and can pose a traveling hazard to native communities in the Arctic. It can significantly alter the remote sensing signature of snow and hence make satellite remote sensing of ice thickness more difficult.

In this chapter it was shown how to jointly invert EM data of up to 3 frequencies to calculate snow, slush, and sea ice thickness using a brute force inversion algorithm. The methods described include a calibration approach for the Inphase return of the EM instrument EMP-400 from GSSI for a three-layer 1D model case. The calibration method is dependent on the instrument as well as the model chosen. Results and expected noise performance of the multi-frequency inversion are presented for two ice types including thin level FYI and thick rough MYI. Furthermore, it was demonstrated how a slush layer can be resolved with mutli-frequency EM measurements, using a 1D five-layer-model inversion based on only the Quadrature output of the instrument. Results show a very good resolution of the slush layer and the total ice thickness. However, the quality of the resolution of the top snow layer is poor with an absolute error of around 20 cm. Additionally, using in situ drill hole measurements the conductivity of the slush layer in the sea ice region near Qikiqtarjuaq was determined to be 1400 mS/m.

Inverted ice thickness results from a multi-frequency inversion using only Quadrature (RMSE = 0.22 m) for the Alert data set as described in this chapter have been used in a study about algea growth under multi-year ice by Lange et al. (2017). The study was able to show that ice algea growth is more prominent under multi-year ice than previously assumed. Further outlining the impact of sea ice and its thickness on Earths biomass and with it Earths ecosystem.

The approaches demonstrated in this study could be further improved by adapting the

method to more than 3 frequencies. Higher frequencies could possibly lead to a higher resolution of the thickness of the snow and sea ice layers. A higher number of frequencies would lead to an over-determined system and therefore, a more stable solution to the inversion problem of a multiple-layer sea ice model.

6. Mapping of Sea Ice and Sub-Ice-Platelet Layer Thickness with Single-Frequency EM Sounding in McMurdo Sound Antarctica

Near the coast of Antarctica, landfast sea ice forms thermodynamically by congelation growth. In the vicinity of ice shelves, which make up 44% of the Antarctic coastline [Le Brocq et al., 2010], this consolidated layer of ice is often underlain by a porous, unconsolidated layer of platelet ice, the so-called Sub-Ice Platelet Layer (SIPL). The SIPL forms from supercooled Ice Shelf Water (ISW) which originates from the basal melt of ice shelves. It is fresher and less dense than the surrounding ocean water and can therefore rise to the water surface and spread under the landfast ice to form an SIPL. For example, in McMurdo Sound in the southern Ross Sea the SIPL can be thicker than 7 m [Price et al., 2014]. The SIPL is an important ingredient for sea ice formation and morphology near ice shelves which can lead to significantly thicker sea ice in close proximity to ice shelves [Hughes et al., 2014; Hoppmann et al., 2015; Gough et al., 2012]. It plays an important role in the heat and mass balance of the adjacent sea

ice and presents a unique biological habitat for primary producers, and is host to some of the highest sea ice algae concentrations in the world [Arrigo et al., 2010]. The volume and distribution of the SIPL are direct indicators for the presence of ISW [Hughes et al., 2014] and have been used for the derivation of an index for ocean ice shelf heat flux [Langhorne et al., 2015].

Despite its importance the regional coverage and inter annual variability of the SIPL are not well known. Thus far, the majority of information about the SIPL comes from in-situ measurements like drill-hole thickness measurements, ice cores, and hydrographic surveys [Mahoney et al., 2011; Hughes et al., 2014; Gough et al., 2012].

The layers of snow and consolidated sea ice, SIPL, and the sea water underneath (Figure 6.1.1) present an ideal target for electromagnetic induction (EM) sounding as their electrical conductivities are very different. While sea ice and snow are highly resistive and cannot be electromagnetically distinguished, sea water is a good conductor [Haas et al., 1997]. In the absence of an SIPL, induction takes place mostly in the seawater, and the distance between the instrument and the surface of the seawater which coincides with the bottom of the sea ice can be accurately measured. The porous, unconsolidated SIPL has a conductivity somewhere between that of sea ice and sea water, and therefore induction takes place in it as well, complicating ice thickness retrievals. Recently Hunkeler et al.(2015; 2016) have shown that it is possible to jointly determine both, consolidated ice and SIPL thickness and conductivity by means of EM sounding. This was accomplished using a ground-based, multi-frequency EM induction device with 5 signal frequencies in the range of 450 Hz to 93090 Hz. They used a small instrument with a transmitter-receiver coil spacing of only 1.66 m, and therefore results are very sensitive to accurate instrument calibration. In addition, the limited depth penetration compromises the accuracy of results over thicker ice [Hunkeler et al., 2016]. Application of that method is limited to mutli-frequency EM devices and not applicable single-frequency instruments that are commonly used for sea ice thickness

measurements.

This study demonstrates how the thickness of consolidated ice and the thickness of the SIPL can be derived by single-frequency EM measurements using one of the most commonly used ground-based EM ice thickness sensors. The instrument has a large coil spacing of 3.66 m which provides for better depth penetration. The method described uses the Inphase (I) and Quadrature (Q) components of the induced secondary field. With these two observables for one operating frequency only two parameters can be derived at the same time, e.g. consolidated ice and SIPL thickness. Therefore, the conductivities of ice, SIPL, and seawater must be known or assumed. However, this study will show that the mean conductivity of the SIPL can be obtained by comparing EM measurements with observed consolidated ice and SIPL thicknesses at drill-sites. Regional EM surveys can then be carried out using the determined mean SIPL conductivity. Drill-holes are also used to confirm the calibration of the EM instrument. This new approach can be applied to a variety of single-frequency EM devices including airborne instruments [Rack et al., 2013].

6.1. Methods and Measurements

The data used for this study were collected during two field campaigns in November 2011 and 2013 staged from New Zealand's Antarctic research station, Scott Base. EM surveys and drill-hole measurements were carried out on landfast sea ice in McMurdo Sound, part of the Western Ross Sea in Antarctica. Measurements included drilling for snow thickness, consolidated ice thickness, and thickness of the SIPL; as well as collocated and regional EM measurements. At each drill site snow, ice, and SIPL thickness were measured with thickness tapes [see e.g. Gough et al. 2012; Price et al. 2014] with typical relative errors for CI and SIPL being ±2% and ±5% respectively [see Hughes et al. 2014; Price et al. 2014 for further details]. In total, 102 coincident drill-hole and EM measurements were carried out in 2011, and 20 in 2013. In addition, 242 km and 45 km of regional surveys were performed in both years.

6.1.1. EM measurements

The EM instrument used for this study was a Geonics EM31-MK2 conductivity sounder ["Geonics EM31-MK2 | EM31-SH".,2013], a single-frequency device with a signal frequency of 9.8 kHz and a coil spacing of 3.66 m (see further details in Chapter 3). This instrument has extensively been used for sea ice thickness measurements in the Arctic and Antarctic under summer and winter conditions [Kovacs and Morey, 1991; Haas et al., 1997, 2008]. The EM instrument was operated in Horizontal Co-Planar (HCP) coil orientation and mounted at a height of 0.4 m above the snow surface on a sledge towed by a snowmobile. In contrast to the commonly used Vertical Co-Planar (VCP) mode the instrument was used in HCP mode because it provides better sensitivity at larger thicknesses. Furthermore, in November the ice in McMurdo Sound is generally thicker than 0.8 m, at which thickness the EM response in HCP mode possesses a local maximum rendering measurements near that thickness ambiguous (see Figure 3.2.4 for

more details) [McNeill, 1980].

Calibration measurements were taken with the EM instrument on the sledge positioned over the drill holes. During the regional surveys, data were continuously logged every second while driving and georeferenced with GPS.

While the instrument's Quadrature measurements are well calibrated by the manufacturer and very stable, the Inphase is not properly calibrated and subject to unknown offset and gain, depending on the setup of the instrument as well as the setting of the instruments configuration dials. Since it is not possible to achieve a universally applicable calibration of the Inphase measurements, a method was developed to calibrate them based on comparison with drill-hole data outlined in section 2.4. Inphase is measured in parts per thousand (ppt) by the instrument ["Geonics EM31-MK2".,2013] and with calibration transferred into ppm for consistency with the model. Only once the Inphase measurement had been properly calibrated by this method can the final inversion of consolidated ice and SIPL thickness be carried out.

6.1.2. 1D EM model

To invert the thicknesses of consolidated ice and SIPL, the measured Inphase and Quadrature are compared with expected responses calculated with a 1D, 4-layer forward model [e.g., Ward and Hohmann.,1988]. The forward model outputs expected values of Inphase and Quadrature that would be measured over any combination of thicknesses and conductivities of two layers overlying a homogeneous half-space of any conductivity. Here, the three layers are the snow and ice layer, the SIPL, and the seawater underneath (Figure 6.1.1). For the purpose of this study snow and ice layers are combined due to their low, indistinguishable conductivities and jointly called the Consolidated Ice (CI) layer with an assumed conductivity of 0 mS/m [Haas, 1997]. The conductivity of the SIPL will be derived in section 6.1.5 by means of comparisons with drill-hole data. The

conductivity of seawater is assumed to be 2700 mS/m, in agreement with Conductivity, Temperature, and Depth (CTD) measurements in McMurdo Sound [Mahoney et al. 2011; Hughes et al. 2014; Leonard et al. 2006]. With these conductivities, the thickness of CI and SIPL are the only two free parameters in the model, and can be unambiguously inverted from measurements of Inphase and Quadrature.

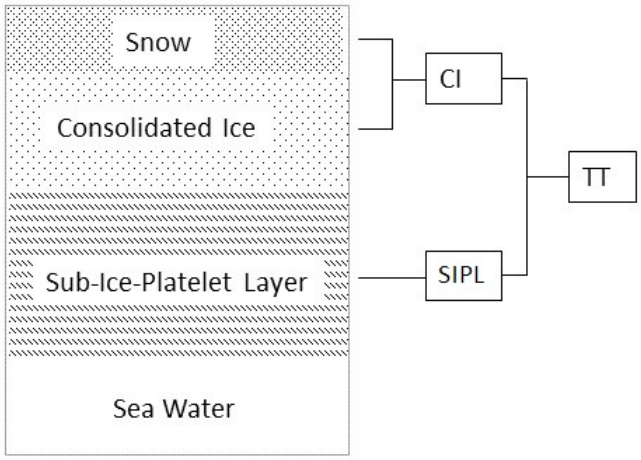

Figure 6.1.1.: Illustration of different ice layers in McMurdo Sound showing layers of snow, consolidated sea ice, the sub-ice platelet layer (SIPL), and the deep seawater underneath. For the purpose of this study the consolidated ice (CI) layer includes snow and consolidated ice. The sum of CI and SIPL thickness is referred to as total thickness (TT).

Using the forward modelling code ODFEM (see Chapter 4) Inphase and Quadrature responses were calculated based on combinations of variable CI and SIPL thicknesses and SIPL conductivities and stored for later inversion. CI thickness was varied from 0.5 m to 6 m and the SIPL thickness was varied from 0 m to 10 m, in 0.1 m increments. For all these thicknesses, SIPL conductivities were varied from 300 to 900 mS/m with steps of 100 mS/m. All model calculations were carried out for an instrument height of 0.4 m above the snow, in agreement with the measurement set up.

As an example, Figure 6.1.2 shows the results of the forward model for a set of varying

CI and SIPL thicknesses and their respective Inphase and Quadrature values, for a constant SIPL conductivity of 500 mS/m. It can be seen that every measured pair of Inphase and Quadrature values can be uniquely assigned to one corresponding, specific pair of CI and SIPL thicknesses.

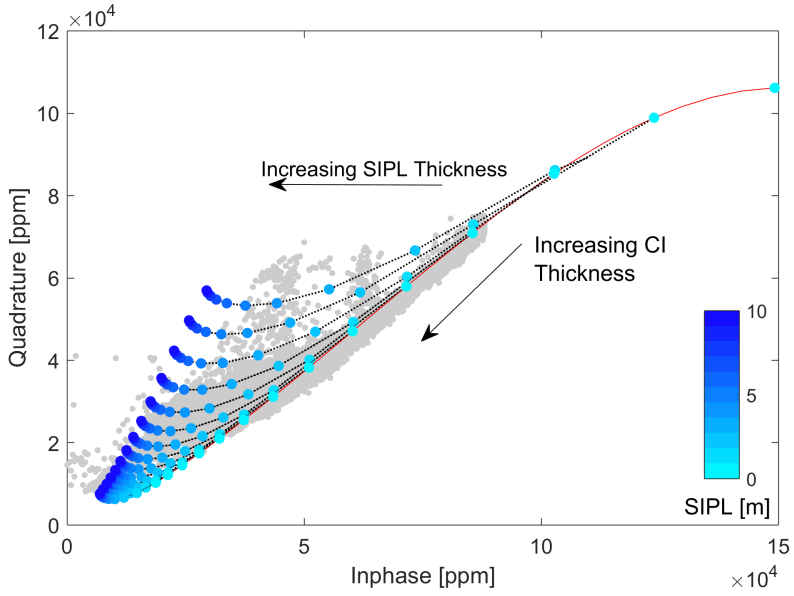

Figure 6.1.2.: Model curves of Quadrature vs. Inphase values of a 3 layer sea ice model, with CI varying from 0.5-6 m (0.5 m increments, each indicated by a black line) and SIPL from 0-10 m (1 m increments) at an SIPL conductivity of 500 mS/m and a water conductivity of 2700 mS/m. The red line indicates results for 0 m SIPL thickness. Gray dots show all EM measurements from the 2011 campaign after calibration.

Figure 6.1.2 also shows that thinner ice results in larger Inphase and Quadrature responses and vice versa. For constant CI thickness, SIPL thickness increases lead to a reduction of Inphase, more strongly than to reductions of Quadrature. It can also be seen that responses to changing CI and SIPL thicknesses are non-linear, with larger responses for thin CI and SIPL and smaller responses for thick layers. These affect the detectability of thickness changes and the expected signal to noise ratio of the measurement, which will generally be lower over thicker CI and SIPL. Figure 6.1.2 also

indicates that an increase in SIPL thickness results in a local minimum for the Quadrature component. Within an isolated analysis of only the Quadrature this would lead to ambiguities which can be mitigated by using both the Inphase and Quadrature in the inversion.

6.1.3. Ice Thickness Inversion

As described in Chapter 4, ice thicknesses are jointly inverted by searching the output of the forward model for the pair of computed Inphase and Quadrature values that most closely agree with the measured values. The complete model space of pre-computed instrument responses is being searched to find the Inphase Quadrature pair with the minimum distance d between model and observations according to Equation 4.3.1.

This allows for the determination of CI and SIPL thicknesses with a resolution of 0.1 m, the resolution chosen in the forward modeling. Using a higher resolution did not lead to significantly different results therefore 0.1 m was chosen to optimize computing time of the inversion.

For a better understanding of the limitations of the method and the instrument sensitivity, the inversion was tested against randomly generated thickness profiles of synthetic data. The inversion can reproduce SIPL and CI thicknesses perfectly for synthetic Inphase and Quadrature values. However observed data, which commonly includes instrument noise and possible noise due to measurement conditions, can only be approximated to the closest fit. Therefore, the inversion was tested on a randomly generated synthetic data set of 10,000 data points for each parameter with 5% noise applied to the Inphase and Quadrature values. Figure 6.1.3 shows the resulting differences between expected CI and SIPL thickness values and the thicknesses estimated by the inversion. The results are displayed as running averages of the absolute and relative differences, which were calculated in 0.5 m increments.

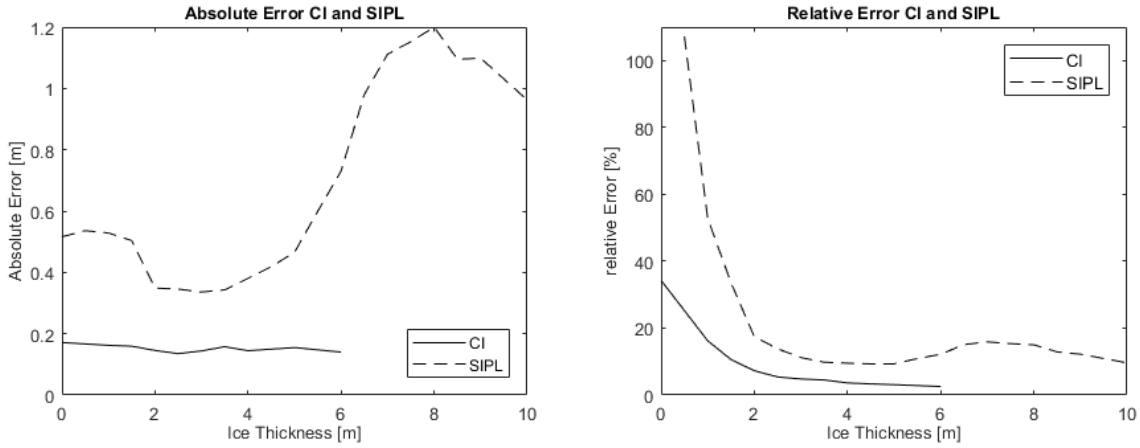

Figure 6.1.3.: Error study on inversion results of Inphase and Quadrature values with 5% noise. Displayed are the average differences over 0.5 m increments between modelled and inverted ice thicknesses for CI and SIPL. Left: absolute errors, Right: relative errors.

Although CI and SIPL thickness errors are displayed separately here, it is important to remember that the SIPL forms underneath the consolidated ice and therefore errors develop as a result of combined thicknesses. An absolute error of 0.5 m for an SIPL thickness of under 2 m can therefore be explained by the effect of the overlying CI layer. While the strong conductivity contrast between consolidated ice and SIPL leads to very consistent CI thickness estimates with absolute errors under 20 cm for all thickness ranges, a thickness change in SIPL, and with it the boundary between SIPL and seawater, cannot be resolved at the same level. However, the total thickness results of both layers can be reliably determined with average relative error values consistently in the range of 10% or lower. For single point measurements, errors might be slightly higher than the average and due to effects that could be introduced by a change in single point conditions like uneven terrain or thick snow affecting the sled with the EM instrument.

6.1.4. Inphase Calibration

Before the model curves shown in Figure 6.1.2 can be inverted for the correct CI and SIPL thicknesses, the EM31 Inphase measurements have to be calibrated and the appropriate SIPL conductivity has to be identified. This is done by means of the collocated EM and drill-hole measurements. As the Inphase measurements of the EM31 are not strictly calibrated, their offset and gain have to be corrected before they can be compared with modelled Inphase values (see Figure 6.1.2), according to:

$$I_{cal} = (I_{obs} + o) \cdot g, \tag{6.1.1}$$

with g as the gain and o as the offset chosen .

Here, the offset is corrected by means of measurements carried out over land before entering the sea ice. Because the ground near Scott Base is solidly frozen in November, the assumption is that the Inphase response is close to 0 ppm. All Inphase data were shifted accordingly, which corresponds to a horizontal shift of data points in Figure 6.1.2. The effect of the offset not being determined perfectly and the signal not reaching 0 ppm is negligible here compared to the amplification of the signal due to gain. A change in offset doesn't change the overall results of thicknesses and conductivities.

To determine the gain a series of inversions is done with varying gains applied to the Inphase. The gain applied on the Inphase is being changed and the inversion repeated as well as the Root-Mean-Square Error (RMSE) calculated (see equation 6.1.2) to determine the fit between measured and inverted ice thickness for each gain used. Then the minimum RMSE is determined and the according gain chosen as the final gain for the calibration of the Inphase. Figure 6.1.4 shows an overview in the steps taken for the calibration. To calibrate the Inphase, the applied gain is being changed, and the inversion applied until the RMSE between expected and measured ice thicknesses is

minimal. The result is an optimal gain for the Inphase in relation to the model as well as the RMSE for the used model.

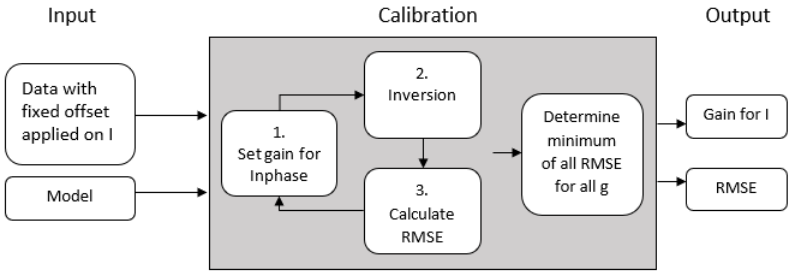

Figure 6.1.4.: Flowchart displaying the steps involved in the calibration of the Inphase. EM data from the drill sites and a model are input into the calibration loop with an offset already applied in the Inphase. Within the loop the gain g applied on the Inphase is changed, ice thickness values inverted and the RMSE calculated for each g applied. Then the minimum RMSE between data and model is determined, resulting in the output of the optimal gain and the RMSE between modelled and measured thickness values..

In this study the RMSE between modelled and drilled ice thickness values is calculated using:

$$RMSE = \frac{1}{2}\left\{\sqrt{\frac{1}{N}\sum_{i=1}^{N}\left(SPL_{m,i} - SPL_{d,i}\right)^2} + \sqrt{\frac{1}{N}\sum\left(CI_{m,i} - CI_{d,i}\right)^2}\right\}, \quad (6.1.2)$$

where SPL_m and SPL_d being modelled (m) and drilled (d) SIPL thicknesses , CT_m and CT_d are respectively CI thicknesses and N being the number of points . The RMSE is an average of the equally weighted RMSEs for the SIPL and CI layers. Since the RMSE varies with the variability in magnitude of errors [Willmott and Matsuura, 2005], this approach was chosen to reduce possible bias from larger magnitudes in error of SIPL

thicknesses. The SIPL can be up to 3-4 times thicker than the CI and therefore can have larger deviations between inverted and measured thickness values. Equal weighting of both SIPL and CI was chosen because it consistently brought the best results.

Once the calibration factor is found it can be applied to the Inphase values of the entire EM data set. Figure (6.1.2) shows the resulting fit of the calibrated drill hole data within the model space as well as the entire calibrated EM data set for 2011. The inverted thickness values can be compared with the thickness results at the drill sites. Figure 6.1.5 shows a comparison of the resulting inverted TT and SIPL thicknesses with the drill hole measurements for the 2011 datta set. With observed values of over 7 m [Price et al., 2014], the SIPL can get much thicker than the thermodynamically grown CI layer at 1-3 m thickness.

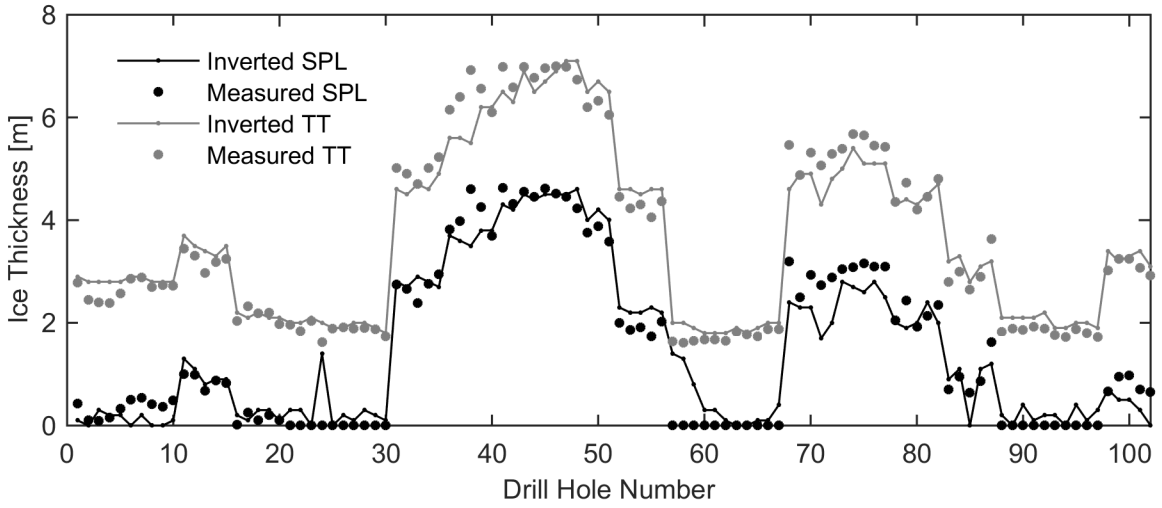

Figure 6.1.5.: Comparison of drill hole data with inverted ice thicknesses for the 2011 data set for a water conductivity of 2700 mS/m and SIPL conductivity of 500 mS/m. Sub-Ice Platelet Layer (SIPL) thickness in black and Total Thickness (TT) in gray. Displayed drill hole data points are not spatially related but rather, are in chronological order of data points taken.

As previously mentioned, the thicker the ice is the smaller the measured instrument return (see Figure 6.1.2) and a higher sensitivity to noise. This has the effect that

measurement noise can lead to larger deviations of the inverted thicknesses from the drill hole results over thicker ice (see section 2.3 for further detail). This can for example be observed in Figure(6.1.5) at drill holes 35-40.

6.1.5. Determining SIPL Conductivity

With the calibrated Inphase it is possible to determine the CI and SIPL thicknesses from the EM data sets. Since the SIPL conductivity is initially unknown, the agreement between measured and inverted ice thickness data is determined by calculating the RMSE for a range of 1D model sets and drill hole data.

To determine the SIPL conductivity the model sets vary in SIPL conductivity from 300 mS/m to 900 mS/m, and ocean water conductivity from 2600 mS/m to 2800 mS/m, in 100 mS/m steps. Figure (6.1.6) shows the RMSE values between drill-hole and inverted data for different SIPL and seawater conductivities for the 2013 and 2011 data. The seawater conductivity in the study area is 2700 mS/m [Mahoney et al. 2011; Hughes et al. 2014; Leonard et al. 2006]. According to Figure (6.1.6) the optimal SIPL conductivity for the 2011 data set is around 500 mS/m with a minimum RMSE = 0.37, while the optimum for the 2013 data set is 700 mS/m with a minimum RMSE = 0.24 at a seawater conductivity of 2700 mS/m.

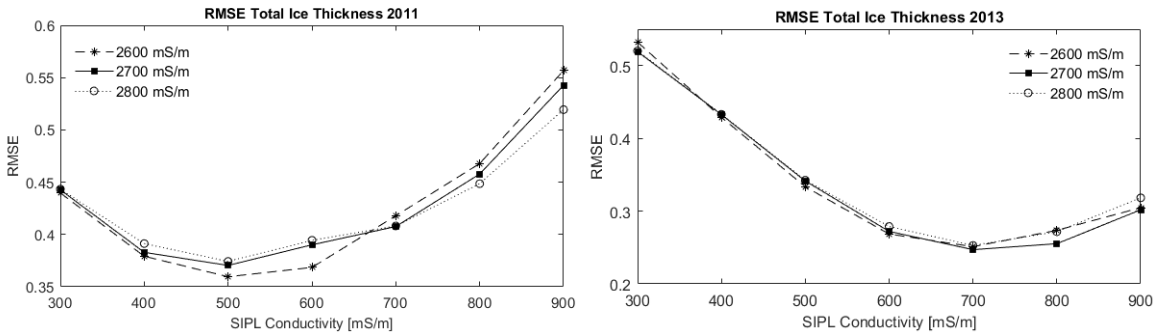

Figure 6.1.6.: RMSE values calculated according to equation (6.1.2) for different conductivity models.

Figure 6.1.6 shows that the minimum RMSE for the 2011 data set is obtained for a

seawater conductivity of 2600 mS/m rather than at 2700 mS/m indicating 2600 mS/m could be close to the real seawater conductivity. However the lowest RMSE values for all seawater conductivities consistently lie at an SIPL conductivity of 500 mS/m for 2011 and 700 mS/m for 2013, which gives confidence in the resulting SIPL conductivities.

6.2. Ice Thickness Results

6.2.1. Regional Ice Thickness Distribution

Figure 6.2.1 shows the inverted ice thicknesses along all EM tracks superimposed on mosaics of Synthetic Aperture Radar (SAR) images of landfast ice in McMurdo Sound. SAR images show the different back scatter properties of the ice and can show local changes in the ice types.

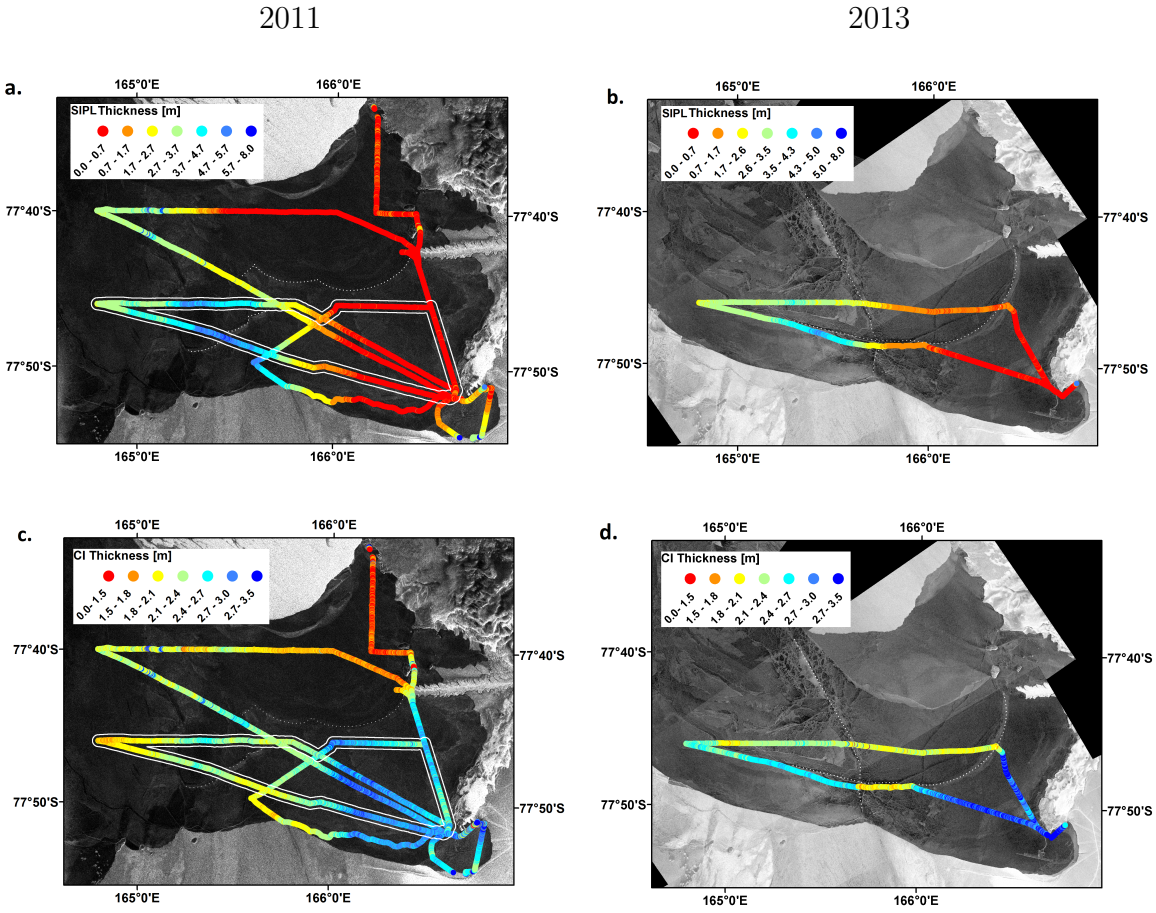

Figure 6.2.1.: SIPL (a.,b.) and CI (c.,d.) thicknesses from the inversion of the EM measurements in McMurdo Sound in 2011 (a.,c.) and 2013 (b.,d.) superimposed on SAR images of the respective years. The data marked with a white frame in the 2011 data are compared to the 2013 data set in Figure 6.2.3 and Figure 6.2.4. Dotted lines indicate boundaries between different ice types and ice ages.

The dotted lines in Figure 6.2.1 mark boundaries of previous winter break out events, which resulted in the presence of younger and thinner ice in the affected areas. The thicknesses of the CI layer as shown in Figure 6.2.1 lay mostly in the range of 2 -3 m, with an average of 2.41 m for 2011 and 2.38 m for 2013. This relatively thick thermodynamically grown ice is twice as thick as sea ice in drifting pack ice areas of the Antarctic [Price et al., 2014].

The plume-like SIPL distribution, with the platelets originating underneath the ice shelf in McMurdo Sound shown in Figure 6.2.2 is very similar to the observations by Barry, 1988; Dempsey et al., 2010; Lewis and Perkin, 2013 and Langhorne et al. (2015). However, EM measurements of the SIPL allow for a much higher resolution in the regional mapping of its ice thickness distribution. Results are also in accordance with the presence of a supercooled ISW plume described by Hughes et al. (2014). The northward extension of the SIPL plume supports previous observations of northward flow of supercooled ISW in winter in western McMurdo Sound [Robinson et al., 2014]. The results of both years are in close agreement with the mean negative ocean heat flux observed in winter throughout McMurdo Sound [Langhorne et al., 2015] .

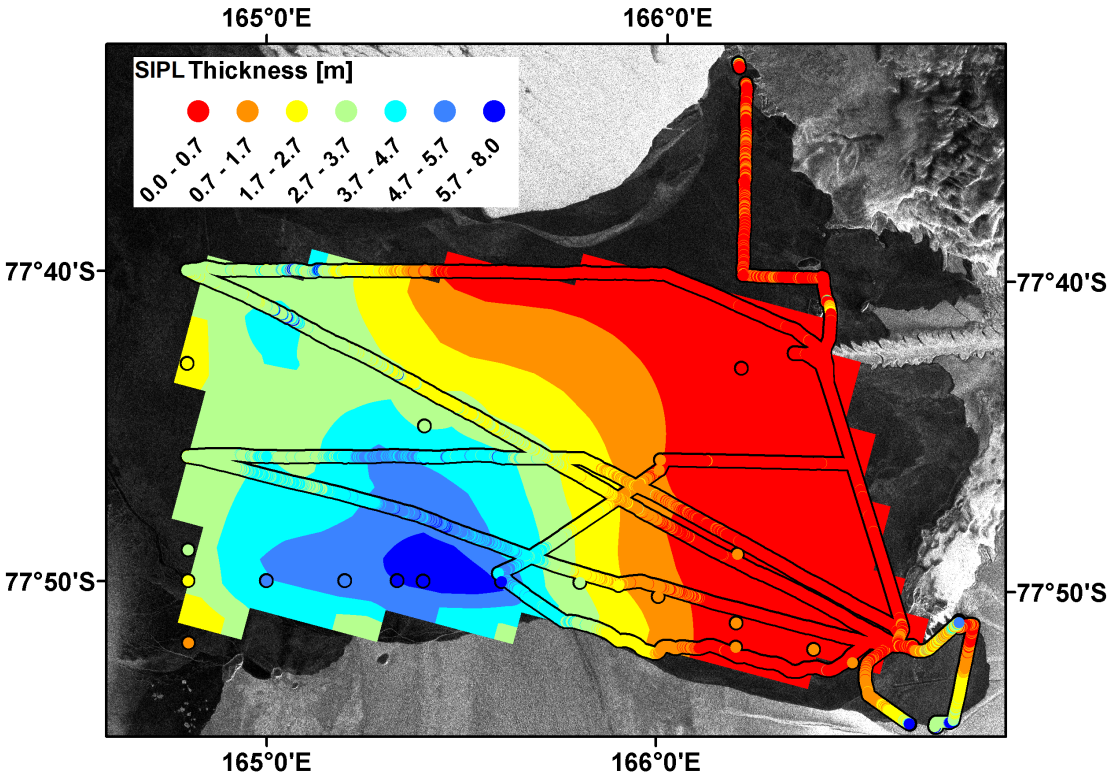

Figure 6.2.2.: Contour map of SIPL thickness in McMurdo Sound 2011 based on drill hole and EM data superimposed on a SAR image .

6.2.2. Inter Annual Comparison

As indicated with white borders in Figure 6.2.1, some part of the EM track from 2011 overlaps with the EM track of 2013, allowing for a more detailed inter annual comparison of the two data sets. Figure 6.2.3 and Figure 6.2.4 show 45 km long SIPL and CI thickness profiles as 50 m averages in comparison to drill hole results. Unfortunately no drill hole data were obtained on the southern transect in 2013. SIPL thickness values can be noisy due to instrument movement while being towed behind the snowmobile. To remove noise and because SIPL thickness is only changing slowly the EM data was smoothed using 50 m averages.

Figure 6.2.3 shows a noticeable difference in SIPL thicknesses between the two years

with average thicknesses in 2011 consistently being 1-2 m higher than in 2013. However, the plume like thickness distribution is evident in both years with good agreement for the location of the center of the plume at 165.3°E for the northern profiles and 165.4°E for the southern profiles. The consistency in thickness distribution along the profiles speaks for the quality and reliability of the thickness inversion.

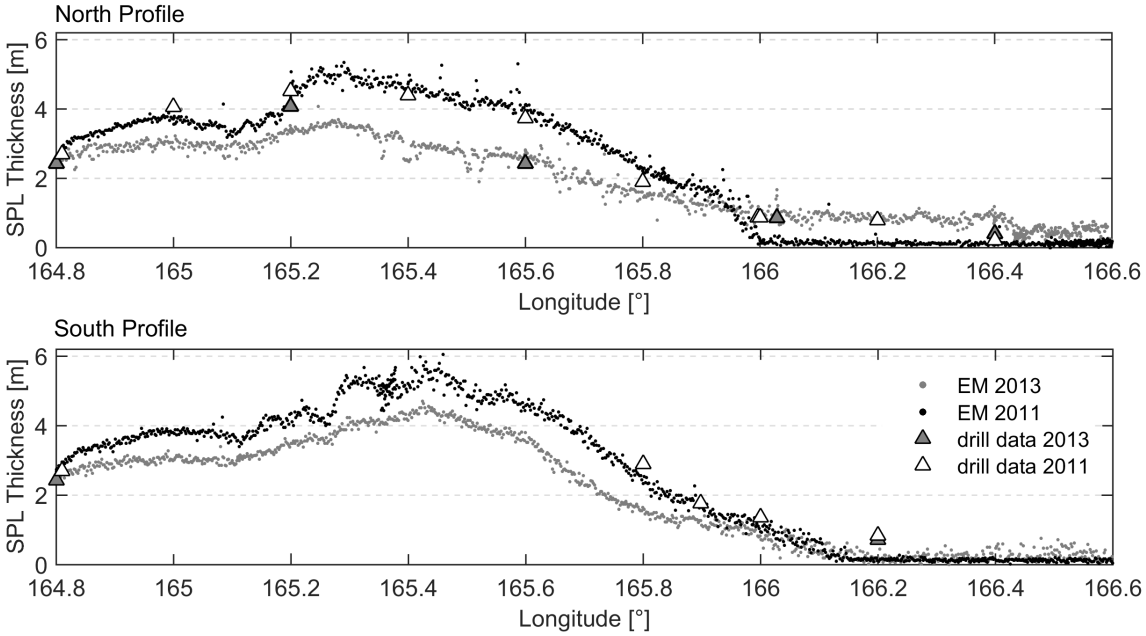

Figure 6.2.3.: Comparison of inverted SIPL thicknesses for 2011 (black) and 2013 (gray) EM data as 50 m averages in comparison to drill hole (triangles) results along two 45 km profiles indicated in Figure 6.2.1.

The CI thickness profiles for both years in Figure 6.2.4 show the regional variability in sea ice conditions and ice types. Steep changes coincide with the break up events visible in Figure 6.2.1. Those changes account for sudden jumps in CI thicknesses along the profile as indicated by arrows in Figure 6.2.4 at 166°E and 166.4°E in the northern profile and 165.6°E in the southern profile. The drill hole results for SIPL and CI thicknesses agree well with the inverted EM measurements. Resulting in RMSE values between drilled and inverted SIPL and CI thicknesses for 2011 of $RMSE_{CI} = 0.32=$ and $RMSE_{SPL} = 0.42$ and $RMSE_{CI} = 0.096$ and $RMSE_{SPL} = 0.397$ respectively

for the 2013 data set. However, drill hole results, which are point measurements, may differ along the profiles in Figure 6.2.3 and Figure 6.2.4 due to the data presentation in 50 m averages and the high local variability of sea ice thicknesses.

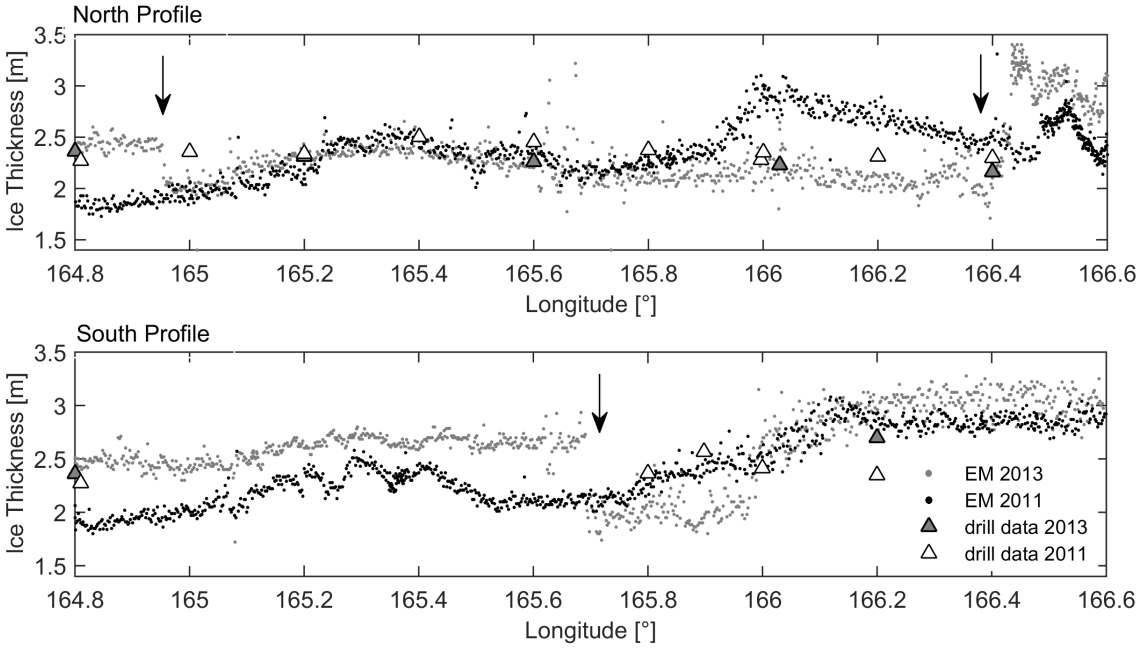

Figure 6.2.4.: Comparison of inverted CI thicknesses for 2011 (black) and 2013 (gray) EM data as 50 m averages in comparison to drill hole (triangles) results along two 45 km profiles indicated in Figure 6.2.1. Arrows indicate locations of ice type change.

6.2.3. Conclusions

The Sub-Ice Platelet Layer and its incorporation into the sea ice cover in the vicinity of ice shelves is an indicator for supercooled Ice Shelf Water and negative ocean heat flux [Langhorne et al., 2015]. Because of direct in-situ methods, like drilling and underwater sonar, used to measure thickness and extent of the Sub-Ice Platelet Layer, still little is known about its distribution around Antarctica.

The approach presented in this chapter provides a method to measure the sub-ice platelet layer thickness and conductivity using a single-frequency EM device. For this study extensive data sets of two field campaign within McMurdo Sound in November 2011 and 2013 were used, which include several EM surveys in combination with drill hole results. In this study it was demonstrated how to calculate consolidated ice thickness plus snow as well as the thickness of the sub-ice platelet layer by means of a brute force inversion using the EM instrument returns of Inphase and Quadrature in combination with the drill hole results, with inverted total thickness values expected to have an average realtive error of 10% or less.

Inverted thicknesses correlate well with the ice conditions in McMurdo Sound as well as supporting evidence of an Ice Shelf Water plume [Hughes et al., 2014] and negative ocean heat flux in the area [Langhorne et al., 2015] during winter. The approach shown in this study can be applied any single-frequency EM devices including application on airborne EM instruments and therefore will enable more extensive and faster mapping of the sub-ice platelet layer around Antarctica.

7. Summary and Outlook

Sea ice is a crucial parameter in climate research as it plays an important role in the interaction between oceans and the atmosphere in polar regions. The vast area covered by sea ice in the cryosphere can only be observed by using a combination of different remote sensing techniques, including satellites, and ground based and airborne surveys. To better understand the role of sea ice cover in the climate system, continued observations of sea ice properties are imperative. While sea ice extent provides a picture of the surface conditions of the ice, ice thickness information is needed to fully understand the overall sea ice conditions. Ice thickness generally tends to respond more slowly to variations in climate forcing than sea ice extent and is therefore considered a more 'stable' climate indicator [Meier, 2017].

The goal of this thesis is to advance the analysis of airborne and ground based sea ice thickness measurements with frequency domain Electromagnetic (EM) sounding. This has been achieved through improving ice thickness retrievals by concurrent use of Inphase and Quadrature components in a numerical inversion for multi- and single-frequency devices.

The forward modelling code and GUI ODFEM (One Dimensional Frequency domain Electromagnetic Model) was successfully developed with MATLAB© to simulate the EM instrument responses for Inphase and Quadrature for different instrument and model settings. Furthermore, a brute force inversion method was established which can be used in combination with the 1D forward models created with ODFEM to

invert single- and multi-frequency EM data into multi-layer ice thicknesses and ice conductivities.

In Chapter 5 a processing scheme was presented to use a brute force inversion for jointly inverting EM measurements of up to 3 frequencies. As part of this analysis, a calibration approach for the Inphase output of the EMP-400 from GSSI was developed. Results and expected noise performance of the inversion are presented for two ice types including thin level FYI and thick rough MYI. Furthermore, a method was presented to resolve layer thicknesses of snow, slush, and sea ice using the brute force inversion on multi-frequency data including 3 frequencies. Slush is a saline saturated moist basal snow layer on top of the ice that plays a significant ecological role as a habitat for ice algea and can pose a traveling hazard to native communities in the arctic. It can significantly alter the remote sensing signature of snow and hence make satellite remote sensing of ice thickness more difficult. It was shown that to resolve the slush layer thickness successfully, a 1D five-layer-model is needed with different layer conductivities for the 5 layers: air, snow, slush, ice, and sea water. Results show a very good resolution of the slush layer and the total ice thickness. However, the quality of the resolution of the top snow layer is not good with an absolute error of around 20 cm.

Lastly, this thesis has demonstrated how a brute force inversion in combination with in situ drill hole measurements can be applied to a single-frequency EM data set to resolve a Sub-Ice-Platelet-Layer (SIPL) prominent under consolidated ice in regions near ice shelves in Antarctica. As part of the analysis a calibration algorithm for the Inphase return of the EM31 from Geonics has been developed, demonstrating that the calibration method for the Inphase of an EM instrument depends on the instrument itself. The used calibration method is also dependent on the model chosen and was verified by comparing inverted ice thickness results with in situ drill hole data. Results show that inverted thicknesses correlate well with the ice conditions in McMurdo Sound and support evidence of an Ice Shelf Water plume [Hughes et al., 2014] and negative

ocean heat flux in the area [Langhorne et al., 2015] during winter. The approach chosen can be applied to any single-frequency EM device. Further work has to be done for adaptation and application of the demonstrated method on airborne devices. Airborne EM measurements would have to be substituted by ground based in situ drill hole measurements to determine SIPL conductivities first. Furthermore, limitation in point resolution due to footprint size as well as other instrument characteristics unique to airborne applications, like the effect of pitch and roll as well as noise from static discharges, have to be considered for the use of Airborne EM SIPL measurements. However, airborne EM measurements would enable more extensive and faster mapping of the sub-ice platelet-layer around Antarctica and with it a better understanding of heat transfer and ISW plume development in those regions.

The resulting methods provide new and more extended applications for a variety of EM devices for ground based and airborne ice thickness surveys. Future work should involve joint inversion of instrument returns of more than 3 frequencies and adapting it to a variety of EM instruments, increasing the accuracy of the snow layer in a five-layer-model inversion in a slush thickness analysis. To be able to resolve more than 5 layers with the optimal case of an over-determined system, the calibration of the Inphase needs to be improved and adjusted to the multi-layer case.

To adapt the presented methods to airborne applications, a change in model setup is needed to account for changing instrument heights. Since the instrument height is commonly measured by the airborne device it would have to be included in the inversion as a known input parameter like Quadrature and Inphase. For an analysis of the platelet layer thickness with a single-frequency airborne device, ground based EM measurements could be used instead of drill holes to validate the inversion results assuming the platelet bulk conductivity is known.

All the mentioned applications would further improve remote sensing applications of sea ice and snow thickness measurement and could greatly improve research of sea ice

conditions and their effect on the climate system.

Bibliography

Ackley, S. F., Lewis, M. J., Fritsen, C. H., and Xie, H., 2008. Internal melting in Antarctic sea ice: Development of "gap layers". *Geophysical Research Letters*, 35(11): 1583. ISSN 00948276. doi: 10.1029/2008GL033644.

Anderson, W. L., 1979. Numerical integration of related Hankel transforms of orders 0 and 1 by adaptive digital filtering. *GEOPHYSICS*, 44(7):1287–1305. ISSN 0016-8033. doi: 10.1190/1.1441007.

Arrigo, K. R., Mock, T., and Lizotte, M. P., 2010. Primary Producers and Sea Ice. In Thomas, D. N., Dieckmann, G. S., and Dieckmann, G., editors, *Sea ice*, pages 283–325. Wiley-Blackwell, Oxford. ISBN 9781444317145. doi: 10.1002/9781444317145.ch8.

Aster, R. C., Borchers, B., and Thurber, C. H. 2013, *Parameter estimation and inverse problems*. Academic Press, Waltham, MA, 2nd ed. edition. ISBN 0123850487.

Barnston, A. G., 1992. Correspondence among the Correlation, RMSE, and Heidke Forecast Verification Measures; Refinement of the Heidke Score. *Weather and Forecasting*, 7(4):699–709. ISSN 0882-8156. doi: 10.1175/1520-0434(1992)007{\textless}0699:CATCRA{\textgreater}2.0.CO;2.

Barry, J. P., 1988. Hydrographic patterns in McMurdo Sound, Antarctica and their relationship to local benthic communities. *Polar Biology*, 8(5):377–391. ISSN 0722-4060. doi: 10.1007/BF00442029.

Coachman, L. K. and Aagaard, K., 1974. Physical Oceanography of Arctic and Subarctic Seas. In Herman, Y., editor, *Marine Geology and Oceanography of the Arctic Seas*, pages 1–72. Springer Berlin Heidelberg, Berlin, Heidelberg. ISBN 978-3-642-87413-0. doi: 10.1007/978-3-642-87411-6$\backslash$textunderscore.

Comiso, J. C., 2012. Large Decadal Decline of the Arctic Multiyear Ice Cover. *Journal of Climate*, 25(4):1176–1193. ISSN 0894-8755. doi: 10.1175/JCLI-D-11-00113.1.

Comiso, J. C. and Parkinson, C. L., 2004. Satellite-Observed Changes in the Arctic. *Physics Today*, 57(8):38–44. ISSN 0031-9228. doi: 10.1063/1.1801866.

Cox, G. F. and Weeks, W. F. 1974, *Salinity Variations in Sea Ice*, volume J. Glaciol., 13, 109–120, 1974.

Curry, J. A., Schramm, J. L., and Ebert, E. E., 1995. Sea Ice-Albedo Climate Feedback Mechanism. *Journal of Climate*, 8(2):240–247. ISSN 0894-8755. doi: 10.1175/1520-0442(1995)008{\textless}0240:SIACFM{\textgreater}2.0.CO;2.

Dempsey, D. E., Langhorne, P. J., Robinson, N. J., Williams, M. J. M., Haskell, T. G., and Frew, R. D., 2010. Observation and modeling of platelet ice fabric in McMurdo Sound, Antarctica. *Journal of Geophysical Research: Solid Earth*, 115(C1). ISSN 2156-2202. doi: 10.1029/2008JC005264. URL `http://onlinelibrary.wiley.com/doi/10.1029/2008JC005264/full`.

Drewry, D. J., Jordan, S. R., and Jankowski, E., 1982. Measured Properties of the Antarctic Ice Sheet: Surface Configuration, Ice Thickness, Volume and Bedrock Characteristics. *Annals of Glaciology*, 3:83–91. ISSN 0260-3055. doi: 10.1017/S0260305500002573.

Eicken, H. 2009, *Field techniques for sea ice research*. University of Alaska Press, Fairbanks. ISBN 9781602230590.

Eicken, H. and Lange, M. A., 1989. Development and properties of sea ice in the coastal

regime of the southeastern Weddell Sea. *Journal of Geophysical Research*, 94(C6): 8193. ISSN 0148-0227. doi: 10.1029/JC094iC06p08193.

Foldvik, A. and Kvinge, T., 1974. Conditional instability of sea water at the freezing point. *Deep Sea Research and Oceanographic Abstracts*, 21(3):169–174. ISSN 00117471. doi: 10.1016/0011-7471(74)90056-4.

Frischknecht, F. C., Labson, V. F., Spies, B. R., and Anderson, W. L., 1991. 3. Profiling Methods Using Small Sources. In Nabighian, M. N., editor, *Electromagnetic methods in applied geophysics*, Investigations in geophysics, pages 105–270. Society of Exploration Geophysicists, Tulsa, Okla. ISBN 978-1-56080-022-4. doi: 10.1190/1.9781560802686.ch3.

Fritsen, C. H., Lytle, V. I., Ackley, S. F., and Sullivan, C. W., 1994. Autumn bloom of antarctic pack-ice algae. *Science*, 266(5186):782–784. ISSN 0036-8075. doi: 10.1126/science.266.5186.782.

Fritsen, C. H., Coale, S. L., Neenan, D. R., Gibson, A. H., and Garrison, D. L., 2001. Biomass, production and microhabitat characteristics near the freeboard of ice floes in the Ross Sea, Antarctica, during the austral summer. *Annals of Glaciology*, 33: 280–286. ISSN 0260-3055. doi: 10.3189/172756401781818653.

Geonics Ltd, editor. 2013, *Geonics EM31-MK2 | EM31-SH*. Geonics Limited - Geophysical Electromagnetic Instruments. URL `http://geonics.com/html/em31-mk2.html`.

Golden, K. M., Ackley, S. F., and Lytle, V. I., 1998. The Percolation Phase Transition in Sea Ice. *Science*, 282(5397):2238–2241. ISSN 0036-8075. doi: 10.1126/science.282.5397.2238.

Gough, A. J., Mahoney, A. R., Langhorne, P. J., Williams, M. J., Robinson, N. J., and Haskell, T. G., 2012. Signatures of supercooling: McMurdo Sound platelet ice. *Journal of Glaciology*, 58(207):38–50. ISSN 00221430. doi: 10.3189/2012JoG10J218.

Gow, A. J., Ackley, S. F., Govoni, J. W., and Weeks, W. F. 1998, *Physical and Structural Properties of Land-Fast Sea Ice in Mcmurdo Sound, Antarctica, in Antarctic Sea Ice: Physical Processes, Interactions and Variability (ed M. O. Jeffries)*, volume v. 74 of *Antarctic research series*. American Geophysical Union, Washington, D.C.

Grant, F. S. and West, G. F. 1965, *Interpretation theory in applied geophysics*. International series in the earth sciences. McGraw-Hill, New York. ISBN 9780070241008.

GSSI, editor. 2017, *Profiler TM EMP-400 Manual*. URL `https://www.geophysical.com/wp-content/uploads/2017/10/GSSI-Profiler-Manual.pdf`.

Guptasarma, D. and Singh, B., 1997. New digital linear filters for Hankel J0 and J1 transforms. *Geophysical Prospecting*, 45(5):745–762. ISSN 0016-8025. doi: 10.1046/j.1365-2478.1997.500292.x.

Haas, C. 1997, *Bestimmung der Meereisdicke mit seismischen und elektromagnetisch-induktiven Verfahren*. Berichte zur Polarforschung. Alfred-Wegener-Inst. für Polar- u. Meeresforschung.

Haas, C., Gerland, S., Eicken, H., and Miller, H., 1997. Comparison of sea–ice thickness measurements under summer and winter conditions in the Arctic using a small electromagnetic induction device. *GEOPHYSICS*, 62(3):749–757. ISSN 0016-8033. doi: 10.1190/1.1444184.

Haas, C., Lobach, J., Hendricks, S., Rabenstein, L., and Pfaffling, A., 2009. Helicopter-borne measurements of sea ice thickness, using a small and lightweight, digital EM system. *Journal of Applied Geophysics*, 67(3):234–241. ISSN 09269851. doi: 10.1016/j.jappgeo.2008.05.005.

Haas, C., 2017. Sea ice thickness distribution. In Thomas, D. N., editor, *Sea ice*, pages 42–64. John Wiley & Sons, Chichester, UK and Hoboken, NJ. ISBN 1118778359. doi: 10.1002/9781118778371.ch2.

Haas, C., Pfaffling, A., Hendricks, S., Rabenstein, L., Etienne, J.-L., and Rigor, I., 2008.

Reduced ice thickness in Arctic Transpolar Drift favors rapid ice retreat. *Geophysical Research Letters*, 35(17):22697. ISSN 00948276. doi: 10.1029/2008GL034457.

Hall, A., 2004. The Role of Surface Albedo Feedback in Climate. *Journal of Climate*, 17(7):1550–1568. ISSN 0894-8755. doi: 10.1175/1520-0442(2004)017{\textless}1550:TROSAF{\textgreater}2.0.CO;2.

Hoppmann, M., Nicolaus, M., Paul, S., Hunkeler, P. A., Heinemann, G., Willmes, S., Timmermann, R., Boebel, O., Schmidt, T., Kühnel, M., König-Langlo, G., and Gerdes, R., 2015. Ice platelets below Weddell Sea landfast sea ice. *Annals of Glaciology*, 56(69):175–190. ISSN 02603055. doi: 10.3189/2015AoG69A678.

Hughes, K. G., Langhorne, P. J., Leonard, G. H., and Stevens, C. L., 2014. Extension of an Ice Shelf Water plume model beneath sea ice with application in McMurdo Sound, Antarctica. *Journal of Geophysical Research: Oceans*, 119(12):8662–8687. ISSN 21699275. doi: 10.1002/2013JC009411.

Hunkeler, P. A., Hoppmann, M., Hendricks, S., Kalscheuer, T., and Gerdes, R., 2016. A glimpse beneath Antarctic sea ice: Platelet layer volume from multifrequency electromagnetic induction sounding. *Geophysical Research Letters*, 43(1):222–231. ISSN 00948276. doi: 10.1002/2015GL065074. URL `http://onlinelibrary.wiley.com/doi/10.1002/2015GL065074/full`.

Hunkeler, P. A., Hendricks, S., Hoppmann, M., Paul, S., and Gerdes, R., 2015. Towards an estimation of sub-sea-ice platelet-layer volume with multi-frequency electromagnetic induction sounding. *Annals of Glaciology*, 56(69):137–146. ISSN 02603055. doi: 10.3189/2015AoG69A705.

Jeffries, M. O., Weeks, W. F., Shaw, R., and Morris, K., 1993. Structural characteristics of congelation and platelet ice and their role in the development of antarctic landfast sea ice. *Journal of Glaciology*, 39(132):223–238. ISSN 0022-1430. doi: 10.3189/S0022143000015884.

Kern, S. and Spreen, G., 2015. Uncertainties in Antarctic sea-ice thickness retrieval from ICESat. *Annals of Glaciology*, 56(69):107–119. ISSN 0260-3055. doi: 10.3189/2015AoG69A736.

Kohnen, H., 1976. Glaciological research relevant to the construction of ice-going ships. *Ocean Engineering*, 3(5):343–360. ISSN 00298018. doi: 10.1016/0029-8018(76)90009-3.

Kovacs, A. and Holladay, J. S., 1990. Sea–ice thickness measurement using a small airborne electromagnetic sounding system. *GEOPHYSICS*, 55(10):1327–1337. ISSN 0016-8033. doi: 10.1190/1.1442780.

Kovacs, A., Valleau, N. C., and Holladay, J. S., 1987. Airborne electromagnetic sounding of sea ice thickness and sub-ice bathymetry. *Cold Regions Science and Technology*, 14(3):289–311. doi: 10.1016/0165-232X(87)90021-8.

Kovacs, A. and Morey, R. M., 1991. Sounding sea ice thickness using a portable electromagnetic induction instrument. *GEOPHYSICS*, 56(12):1992–1998. ISSN 0016-8033. doi: 10.1190/1.1443011.

Krishfield, R. A., Proshutinsky, A., Tateyama, K., Williams, W. J., Carmack, E. C., McLaughlin, F. A., and Timmermans, M.-L., 2014. Deterioration of perennial sea ice in the Beaufort Gyre from 2003 to 2012 and its impact on the oceanic freshwater cycle. *Journal of Geophysical Research: Oceans*, 119(2):1271–1305. ISSN 21699275. doi: 10.1002/2013JC008999.

Kwok, R. and Rothrock, D. A., 2009. Decline in Arctic sea ice thickness from submarine and ICESat records: 1958-2008. *Geophysical Research Letters*, 36(15):n/a–n/a. ISSN 00948276. doi: 10.1029/2009GL039035.

Kwok, R., 2004. ICESat observations of Arctic sea ice: A first look. *Geophysical Research Letters*, 31(16):25,747. ISSN 00948276. doi: 10.1029/2004GL020309.

Laine, V., 2004. Arctic sea ice regional albedo variability and trends, 1982–1998. *Journal of Geophysical Research*, 109(C6):994. ISSN 0148-0227. doi: 10.1029/2003JC001818.

Lange, B. A., Flores, H., Michel, C., Beckers, J. F., Bublitz, A., Casey, J. A., Castellani, G., Hatam, I., Reppchen, A., Rudolph, S. A., and Haas, C., 2017. Pan-Arctic sea ice-algal chl a biomass and suitable habitat are largely underestimated for multiyear ice. *Global change biology*, 23(11):4581–4597. ISSN 1365-2486. doi: 10.1111/gcb.13742.

Langhorne, P. J., Hughes, K. G., Gough, A. J., Smith, I. J., Williams, M. J. M., Robinson, N. J., Stevens, C. L., Rack, W., Price, D., Leonard, G. H., Mahoney, A. R., Haas, C., and Haskell, T. G., 2015. Observed platelet ice distributions in Antarctic sea ice: An index for ocean-ice shelf heat flux. *Geophysical Research Letters*, 42(13): 5442–5451. ISSN 00948276. doi: 10.1002/2015GL064508.

Laxon, S. W., Giles, K. A., Ridout, A. L., Wingham, D. J., Willatt, R., Cullen, R., Kwok, R., Schweiger, A., Zhang, J., Haas, C., Hendricks, S., Krishfield, R., Kurtz, N., Farrell, S., and Davidson, M., 2013. CryoSat-2 estimates of Arctic sea ice thickness and volume. *Geophysical Research Letters*, 40(4):732–737. ISSN 00948276. doi: 10.1002/grl.50193.

Le Brocq, A. M., Payne, A. J., and Vieli, A., 2010. An improved Antarctic dataset for high resolution numerical ice sheet models (ALBMAP v1). *Earth System Science Data*, 2(2):247–260. ISSN 1866-3516. doi: 10.5194/essd-2-247-2010.

Leonard, G. H., Purdie, C. R., Langhorne, P. J., Haskell, T. G., Williams, M. J. M., and Frew, R. D., 2006. Observations of platelet ice growth and oceanographic conditions during the winter of 2003 in McMurdo Sound, Antarctica. *Journal of Geophysical Research*, 111(C4):255. ISSN 0148-0227. doi: 10.1029/2005JC002952.

Lewis, E. L. and Perkin, R. G., 2013. The Winter Oceanography of McMurdo Sound, Antarctica. In *Oceanology of the Antarctic Continental Shelf*, pages 145–165. Amer-

ican Geophysical Union. ISBN 9781118665206. doi: 10.1029/AR043p0145. URL http://dx.doi.org/10.1029/AR043p0145.

Lowrie, W. 2007, *Fundamentals of geophysics*. Cambridge University Press, Cambridge, 2nd ed. edition. ISBN 0521675960.

Lusilier. Sea Ice Drawing General Features: [Electronic Resource], license: CC BY-SA 3.0, 2012. URL <https://commons.wikimedia.org/wiki/File:Sea_ice_Drawing_General_features.svg>.

Lytle, V. I. and Ackley, S. F., 1996. Heat flux through sea ice in the western Weddell Sea: Convective and conductive transfer processes. *Journal of Geophysical Research: Oceans*, 101(C4):8853–8868. ISSN 21699275. doi: 10.1029/95JC03675.

Mahoney, A. R., Gough, A. J., Langhorne, P. J., Robinson, N. J., Stevens, C. L., Williams, M. M. J., and Haskell, T. G., 2011. The seasonal appearance of ice shelf water in coastal Antarctica and its effect on sea ice growth. *Journal of Geophysical Research*, 116(C11):L24606. ISSN 0148-0227. doi: 10.1029/2011JC007060.

Maslanik, J., Stroeve, J., Fowler, C., and Emery, W., 2011. Distribution and trends in Arctic sea ice age through spring 2011. *Geophysical Research Letters*, 38(13):n/a–n/a. ISSN 00948276. doi: 10.1029/2011GL047735.

Massom, R. A., Lytle, V. I., Worby, A. P., and Allison, I., 1998. Winter snow cover variability on East Antarctic sea ice. *Journal of Geophysical Research: Oceans*, 103 (C11):24837–24855. ISSN 21699275. doi: 10.1029/98JC01617.

Massom, R. A., Eicken, H., Hass, C., Jeffries, M. O., Drinkwater, M. R., Sturm, M., Worby, A. P., Wu, X., Lytle, V. I., Ushio, S., Morris, K., Reid, P. A., Warren, S. G., and Allison, I., 2001. Snow on Antarctic sea ice. *Reviews of Geophysics*, 39(3): 413–445. ISSN 87551209. doi: 10.1029/2000RG000085.

Massom, R. A., Giles, A. B., Fricker, H. A., Warner, R. C., Legrésy, B., Hyland, G., Young, N., and Fraser, A. D., 2010. Examining the interaction between multi-year

landfast sea ice and the Mertz Glacier Tongue, East Antarctica: Another factor in ice sheet stability? *Journal of Geophysical Research*, 115(C12):L21S02. ISSN 0148-0227. doi: 10.1029/2009JC006083.

McNeill, J. D., 1980. Electromagnetic Terrain Conductivity Measurement at Low Induction Numbers. Technical Note TN-6.

Meier, W. N., 2017. Losing Arctic sea ice: observations of the recent decline and the long–term context. In Thomas, D. N., editor, *Sea ice*, pages 290–303. John Wiley & Sons, Chichester, UK and Hoboken, NJ. ISBN 1118778359. doi: 10.1002/9781118778371.ch11.

Meier, W. N., Stroeve, J., and Fetterer, F., 2007. Whither Arctic sea ice? A clear signal of decline regionally, seasonally and extending beyond the satellite record. *Annals of Glaciology*, 46:428–434. ISSN 0260-3055. doi: 10.3189/172756407782871170.

Multala, J., Hautaniemi, H., Oksama, M., Leppäranta, M., Haapala, J., Herlevi, A., Riska, K., and Lensu, M., 1996. An airborne electromagnetic system on a fixed wing aircraft for sea ice thickness mapping. *Cold Regions Science and Technology*, 24(4): 355–373. doi: 10.1016/S0165-232X(96)00006-7.

Mundry, E., 1984. On the interpretation of airborne electromagnetic data for the two-layer case*. *Geophysical Prospecting*, 32(2):336–346. ISSN 0016-8025. doi: 10.1111/j.1365-2478.1984.tb00735.x.

Murphy, A. H. and Epstein, E. S., 1989. Skill Scores and Correlation Coefficients in Model Verification. *Monthly Weather Review*, 117(3):572–582. ISSN 0027-0644. doi: 10.1175/1520-0493(1989)117{\textless}0572:SSACCI{\textgreater}2.0.CO;2.

Nandan, V., Geldsetzer, T., Yackel, J., Mahmud, M., Scharien, R., Howell, S., King, J., Ricker, R., and Else, B., 2017. Effect of Snow Salinity on CryoSat-2 Arctic First-Year Sea Ice Freeboard Measurements. *Geophysical Research Letters*, 44(20): 10,419–10,426. ISSN 00948276. doi: 10.1002/2017GL074506.

NSIDC. State of the Cryosphere: is the cryosphere sending signals about climate change?, 2017.

Penrose, J. D., Conde, M., and Pauly, T. J., 1994. Acoustic detection of ice crystals in Antarctic waters. *Journal of Geophysical Research*, 99(C6):12573. ISSN 0148-0227. doi: 10.1029/93JC03507.

Perovich, D. K., 1996. The Optical Properties of Sea Ice. 96:31.

Perovich, D. K. and Polashenski, C., 2012. Albedo evolution of seasonal Arctic sea ice. *Geophysical Research Letters*, 39(8):n/a–n/a. ISSN 00948276. doi: 10.1029/2012GL051432.

Petrich, C. and Eicken, H., 2010. Growth, Structure and Properties of Sea Ice. In Thomas, D. N., editor, *Sea ice*, pages 23–77. Wiley-Blackwell, Oxford. ISBN 9781444317145. doi: 10.1002/9781444317145.ch2.

Price, D., Rack, W., Langhorne, P. J., Haas, C., Leonard, G., and Barnsdale, K., 2014. The sub-ice platelet layer and its influence on freeboard to thickness conversion of Antarctic sea ice. *The Cryosphere*, 8(3):1031–1039. ISSN 1994-0424. doi: 10.5194/tc-8-1031-2014.

Przybylak, R., 2007. Recent air-temperature changes in the Arctic. *Annals of Glaciology*, 46:316–324. ISSN 02603055. doi: 10.3189/172756407782871666.

Rack, W., Haas, C., and Langhorne, P. J., 2013. Airborne thickness and freeboard measurements over the McMurdo Ice Shelf, Antarctica, and implications for ice density. *Journal of Geophysical Research: Oceans*, 118(11):5899–5907. ISSN 21699275. doi: 10.1002/2013JC009084.

Reid, J. E., Pfaffling, A., Worby, A. P., and Bishop, J. R., 2006. In situ measurements of the direct-current conductivity of Antarctic sea ice: Implications for airborne electromagnetic sounding of sea-ice thickness. *Annals of Glaciology*, 44(1):217–223. ISSN 0260-3055. doi: 10.3189/172756406781811772.

Reid, J. E., Pfaffling, A., and Vrbancich, J., 2006b. Airborne electromagnetic footprints in 1D earths. *GEOPHYSICS*, 71(2):G63–G72. ISSN 0016-8033. doi: 10.1190/1.2187756.

Robinson, N. J., Williams, M. J. M., Stevens, C. L., Langhorne, P. J., and Haskell, T. G., 2014. Evolution of a supercooled Ice Shelf Water plume with an actively growing subice platelet matrix. *Journal of Geophysical Research: Oceans*, 119(6):3425–3446. ISSN 21699275. doi: 10.1002/2013JC009399.

Saenz, B. T. and Arrigo, K. R., 2012. Simulation of a sea ice ecosystem using a hybrid model for slush layer desalination. *Journal of Geophysical Research: Oceans*, 117 (C5):n/a–n/a. ISSN 21699275. doi: 10.1029/2011JC007544.

Sen, M. K. and Stoffa, P. L. 2013, *Global Optimization Methods in Geophysical Inversion*. Cambridge University Press, Cambridge. ISBN 129925764X.

Smedsrud, L. H. and Jenkins, A., 2004. Frazil ice formation in an ice shelf water plume. *Journal of Geophysical Research: Oceans*, 109(C3):257. ISSN 21699275. doi: 10.1029/2003JC001851.

Smith, I. J., Langhorne, P. J., Haskell, T. G., Joe Trodahl, H., Frew, R., and Ross Vennell, M., 2001. Platelet ice and the land-fast sea ice of McMurdo Sound, Antarctica. *Annals of Glaciology*, 33:21–27. ISSN 0260-3055. doi: 10.3189/172756401781818365.

Stammerjohn, S. and Maksym, T., 2017. Gaining (and losing) Antarctic sea ice: variability, trends and mechanisms. In Thomas, D. N., editor, *Sea ice*, pages 261–289. John Wiley & Sons, Chichester, UK and Hoboken, NJ. ISBN 1118778359. doi: 10.1002/9781118778371.ch10.

Steele, M., Zhang, J., and Ermold, W., 2010. Mechanisms of summertime upper Arctic Ocean warming and the effect on sea ice melt. *Journal of Geophysical Research*, 115 (C11):529. ISSN 0148-0227. doi: 10.1029/2009JC005849.

Stocker, T. 2014, *Climate change 2013: The physical science basis : Working Group I*

contribution to the Fifth assessment report of the Intergovernmental Panel on Climate Change / edited by Thomas F. Stocker, Working Group I co-chair, University of Bern [and nine others]. Cambridge University Press, New York. ISBN 9781107661820.

Stroeve, J., Holland, M. M., Meier, W., Scambos, T., and Serreze, M., 2007. Arctic sea ice decline: Faster than forecast. *Geophysical Research Letters*, 34(9). ISSN 00948276. doi: 10.1029/2007GL029703.

Stroeve, J. C., Kattsov, V., Barrett, A., Serreze, M., Pavlova, T., Holland, M., and Meier, W. N., 2012. Trends in Arctic sea ice extent from CMIP5, CMIP3 and observations. *Geophysical Research Letters*, 39(16):n/a. ISSN 00948276. doi: 10.1029/2012GL052676.

Strub-Klein, L. and Sudom, D., 2012. A comprehensive analysis of the morphology of first-year sea ice ridges. *Cold Regions Science and Technology*, 82:94–109. doi: 10.1016/j.coldregions.2012.05.014.

Thomas, D. N. and Dieckmann, G. 2003, *Sea ice: An introduction to its physics, chemistry, biology, and geology.* Blackwell Science, Oxford, UK and Malden, MA, USA. ISBN 0470757167.

Timco, G. W., 1979. An Analysis of the In-Situ Resistivity of Sea Ice in Terms of its Microstructure. *Journal of Glaciology Journal of Glaciology*, 22(88):461–471. ISSN 0022-1430. doi: 10.1017/S0022143000014465.

Tison, J.-L., Lorrain, R. D., Bouzette, A., Dini, M., Bondesan, A., and StiéVenard, M., 2013. Linking Landfast Sea Ice Variability to Marine Ice Accretion at Hells Gate Ice Shelf, Ross Sea. In Jeffries, M. O., editor, *Antarctic Sea Ice: Physical Processes, Interactions and Variability*, pages 375–407. American Geophysical Union. ISBN 9781118668245. doi: 10.1029/AR074p0375. URL `http://dx.doi.org/10.1029/AR074p0375`.

Tschudi, M., Fowler, C., Maslanik, J., Stewart, J. S., and Meier, W. N. 2016, *EASE*

Grid Sea Ice Age, Version 3. Boulder, Colorado USA. NASA National Snow and Ice Data Center Distributed Active Archive Center. doi: 10.5067/PFSVFZA9Y85G.

Wadhams, P. 2000, *Ice in the ocean*. Gordon and Breach, Australia. ISBN 9056992961.

Wadhams, P., Lange, M. A., and Ackley, S. F., 1987. The ice thickness distribution across the Atlantic sector of the Antarctic Ocean in midwinter. *Journal of Geophysical Research*, 92(C13):14535. ISSN 0148-0227. doi: 10.1029/JC092iC13p14535.

Ward, S. H. and Hohmann, G. W., 1988 (1989 printing)-1991. 4. Electromagnetic Theory for Geophysical Applications. In Nabighian, M. N., editor, *Electromagnetic methods in applied geophysics*, Investigations in geophysics, pages 130–311. Society of Exploration Geophysicists, Tulsa, Okla. ISBN 978-0-931830-51-8. doi: 10.1190/1.9781560802631.ch4.

Weeks, W. F. 2010, *On sea ice*. University of Alaska Press, Fairbanks. ISBN 9781602230798.

Weissling, B. P., Lewis, M. J., and Ackley, S. F., 2011. Sea-ice thickness and mass at Ice Station Belgica, Bellingshausen Sea, Antarctica. *Deep Sea Research Part II: Topical Studies in Oceanography*, 58(9-10):1112–1124. ISSN 09670645. doi: 10.1016/j.dsr2.2010.10.032.

Willmott, C. J. and Matsuura, K., 2005. Advantages of the mean absolute error (MAE) over the root mean square error (RMSE) in assessing average model performance. *Climate Research*, 30:79–82. doi: 10.3354/cr030079.

Zhdanov, M. S. 2002, *Geophysical inverse theory and regularization problems*, volume 36 of *Methods in geochemistry and geophysics*. Elsevier Science, Amsterdam and Oxford. ISBN 0080532500.

List of Abbreviations

Abbreviation	Description
EM	electromagnetic induction sounding
FYI	first-year ice
MYI	multi-year ice
TT	total ice thickness of all ice and snow layers
CI	consolidated ice including snow
SIPL	sub-ice-platelet-layer
I	Inphase
Q	Quadrature
RMSE	root-mean-square error
GUI	graphic user interface
ODFEM	One Dimensional Frequency domain Electromagnetic Model
ISW	ice-shelf -water
SAR	Synthetic Aperture Radar
VCP	vertical co-planar coil orientation
HCP	horizontal co-planar coil orientation

List of Physical Variables and Symbols

Symbol	Description	Unit
σ	conductivity	S/m
σ_a	apparent conductivity	S/m
ω	angular frequency	rad/s
ε	dielectric constant	
μ	magnetic permeability	H/m
μ_0	magnetic permeability of free space	$4\pi \cdot 10^{-7}$H/m
$\mathbf{E}$	electric field	V/m
$\mathbf{H}$	magnetic field	A/m
f	frequency	Hz
h_0	instrument height	m
δ	skin depth	m
r	coil distance	m
H_p	primary magnetic field	A/m
H_s	secondary magnetic field	A/m

A. ODFEM Output File Format

A.1. ASCII-File

Files are saved as with the timestamp as the filename as timestamp.dat unless another filename is chosen. The .dat file is tab delimited and provides all the model and instrument parameters chosen in the header of the data file. Data is output in the units given when parameters are input in the ODFEM GUI. Inphase and Quadrature are output in ppm. The printing format of the model output within the file is also given in the header. Since the model can be calculated for more than one frequency each, the data for each frequency is written into separate sections in form of:

Frequency: f1

d1 d2 d3 d4

Frequency: f2

d1 d2 d3 d4

Figure A.1.1 shows an example of ODFEM .dat file data output for 3 layer model including header.

```
ODFEM model parameters used
Mode:      VCP
Coil Distance:  3.66
Number of Frequencies:     1
Frequency: 9800
Number of Layers:     3
Model Resolution:     0.10
Layer 2 - Thickness Min, Thickness Max, Conductivity:  0     8     0
Printing Format:      Layer 2    Q     I
Frequency:      9800
0.00  2.801076e+05     1.702328e+05
0.10  2.592438e+05     1.589868e+05
0.20  2.396396e+05     1.486017e+05
0.30  2.212984e+05     1.390101e+05
0.40  2.042059e+05     1.301489e+05
0.50  1.883329e+05     1.219592e+05
0.60  1.736377e+05     1.143866e+05
0.70  1.600688e+05     1.073804e+05
0.80  1.475680e+05     1.008940e+05
```

Figure A.1.1.: Example of ODFEM .dat file data output for 3 layer model including header.

A.2. MATLAB-File

Files are saved as with the timestamp as the filename as timestamp.mat unless another filename is chosen. Within the structure variables instr_par and model_par include all the input parameters for the instrument and model settings respectively. Additionally modelled Inphase and Quadrature results as well as the Layer thicknesses are saved as vector variables. Table A.2.1 gives an overview of all the variable names and their meanings.

Variables	Description	Comments
I1	Inphase values for the 1st frequency [ppm]	I2, I3 for the second and third frequency
Q1	Quadrature values for the 1st frequency [ppm]	Q2, Q3 for the second and third frequency
L2T	Layer 2 thickness values from min to max [m]	L3T, L4T thickness values for 3rd and 4th layer
model_par.layN	Number of layers chosen	
model_par.LRes	Layer Resolution [m]	
model_par.LTmin	Layer thickness minimum for all layers [m]	Values are given in input order
model_par.LTmax	Layer thickness maximum for all layers [m]	Values are given in input order
model_par.LCond	Conductivity for all layers [mS/m]	Values are given in input order
instr_par.f	Frequencies chosen [Hz]	Values are given in input order
instr_par.nf	Number of frequencies	
instr_par.mode	Measurement mode	
instr_par.r	Instrument radius [m]	

Table A.2.1.: ODFEM .mat file variable descriptions.

B. In Situ Drill Hole Measurement Data

B.1. Qikiqtarjuaq 2017

B.1.1. Drill Hole Thickness Measurements

Point ID	Latitude [°]	Longitude [°]	Snow [cm]	Slush [cm]	Ice [cm]	TT [cm]
1	67.4080033	-63.9033700	10	7	13	30
2	67.3210833	-63.8601950	12	18	15	45
3	67.3830650	-63.9153950	19	21	15	55
4	67.3841417	-63.9125083	13	21	17	51
5	67.3203333	-63.8610667	7	21	10	38
6	67.4097900	-63.9016633	6	22	19	47
7	67.4082467	-63.9033717	7	25	12	44
8	67.4087033	-63.9036800	10	26	15	51
9	67.3832467	-63.9125750	7	27	17	51
10	67.4087300	-63.9037067	9	30	11	50
11	67.4101833	-63.9018000	22	31	13	66
12	67.4097483	-63.9019817	13	31	7	51
13	67.4098767	-63.9028167	14	31	11	56
14	67.3830500	-63.9141800	13	31	17	61
15	67.4099650	-63.9047800	16	32	16	64
16	67.3830400	-63.9146983	0	32	20	52
17	67.3844050	-63.9126450	14	32	18	64
18	67.3855067	-63.9104117	11	33	15	59
19	67.3199833	-63.8618117	15	33	25	73
20	67.3839183	-63.9175900	13	34	23	70

Table B.1.1.: Used ice and snow thickness values measured at drill sites of Qikiqtarjuaq 2017 campaign part 1.

Point ID	Latitude [°]	Longitude [°]	Snow [cm]	Slush [cm]	Ice [cm]	TT [cm]
21	67.3831233	-63.9133617	15	38	15	68
22	67.4111683	-63.9035083	11	40	22	73
23	67.3206167	-63.8612117	18	40	12	70
24	67.3210417	-63.8606317	20	42	5	67
25	67.3907450	-63.9351150	22	45	20	87
26	67.3835167	-63.9166050	18	45	18	81
27	67.4096783	-63.9049000	19	46	6	71
28	67.3841250	-63.9180783	21	49	20	90
29	67.3896650	-63.9324433	19	50	22	91
30	67.3202333	-63.8650183	20	50	5	75
31	67.3208250	-63.8609150	13	50	17	80
32	67.4164733	-63.9183433	29	56	15	100
33	67.3846433	-63.9194883	40	59	10	109
34	67.4202833	-63.9280733	35	64	7	106
35	67.4244417	-63.9372283	33	67	19	119
36	67.5570067	-64.0690233	41	73	1	115
37	67.4264400	-63.9423183	26	75	14	115
38	67.3890383	-63.9307617	35	75	0	110
39	67.5533717	-64.0744883	41	80	0	121
40	67.5597933	-64.0694683	38	82	0	120
41	67.5533133	-64.0747883	48	83	0	131
42	67.4519467	-63.6668517	61	88	25	174
43	67.5536017	-64.0731700	41	91	0	132
44	67.5492233	-64.1010117	40	92	0	132
45	67.5529533	-64.0769317	36	92	0	128
46	67.5563367	-64.0574217	47	92	2	141
47	67.5609783	-64.0406550	55	92	0	147
48	67.5600117	-64.0437700	41	93	0	134
49	67.5507650	-64.0966083	45	93	0	138
50	67.5489533	-64.1026667	36	93	0	129
51	67.5607017	-64.0446600	39	94	0	133
52	67.5521283	-64.0944067	39	96	4	139
53	67.5488767	-64.1031467	40	96	0	136
54	67.5603167	-64.0573667	45	96	0	141
55	67.5559167	-64.0935933	37	97	0	134

Table B.1.2.: Used ice and snow thickness values measured at drill sites of Qikiqtarjuaq 2017 campaign part 2.

Point ID	Latitude [°]	Longitude [°]	Snow [cm]	Slush [cm]	Ice [cm]	TT [cm]
56	67.5602017	-64.0605167	46	97	0	143
57	67.5595550	-64.0977167	39	98	0	137
58	67.5595100	-64.0387450	41	99	0	140
59	67.5601500	-64.0615500	41	99	0	140
60	67.5634233	-64.0570683	24	100	1	125
61	67.5473333	-64.1015683	38	100	0	138
62	67.5585133	-64.0453667	33	100	0	133
63	67.5530983	-64.0760883	39	100	0	139
64	67.5589150	-64.0969850	37	101	0	138
65	67.5523817	-64.0803733	40	101	0	141
66	67.5537817	-64.0721250	35	101	0	136
67	67.5600300	-64.0735900	41	104	0	145
68	67.5535617	-64.0912233	47	104	0	151
69	67.5611367	-64.0378517	40	105	0	145
70	67.5488483	-64.1032783	37	105	0	142
71	67.5577200	-64.0493800	41	110	0	151
72	67.5493733	-64.1001283	36	110	0	146
73	67.5470850	-64.1032683	34	112	0	146
74	67.5488250	-64.1034633	35	112	0	147
75	67.5602367	-64.0349083	50	113	0	163
76	67.5623700	-64.0968833	48	114	0	162
77	67.5603083	-64.0762667	35	115	0	150
78	67.5615733	-64.0695100	27	116	0	143
79	67.5625750	-64.0988283	37	117	0	154
80	67.5603750	-64.0769517	40	120	0	160
81	67.5584550	-64.0372717	38	120	0	158
82	67.5624750	-64.0978950	50	120	0	170
83	67.5613817	-64.0869267	33	124	0	157
84	67.5615900	-64.0336033	33	125	0	158
85	67.5626950	-64.1002783	34	128	0	162

Table B.1.3.: Used ice and snow thickness values measured at drill sites of Qikiqtarjuaq 2017 campaign part 3.

B.1.2. Drill Hole EMP Measurements

Point ID	5 kHz		10 kHz		15 kHz	
	I [ppm]	Q [ppm]	I [ppm]	Q [ppm]	I [ppm]	Q [ppm]
1	7365	20200	17054	34477	27394	45673
2	8490	20465	20558	34566	34597	45383
3	6782	16025	16514	26760	27838	34786
4	7326	18234	17855	30936	29997	40656
5	7798	17953	18593	30115	31332	39461
6	6818	17699	15779	29832	25210	39258
7	8435	19530	17964	32920	27964	43425
8	7256	19742	16921	33681	27200	44678
9	7226	17031	17460	28622	29302	37361
10	7257	19745	16862	33713	27163	44620
11	6465	16996	15064	28545	24080	37546
12	7017	19545	16472	33394	26677	44359
13	7707	16540	16073	27738	24763	36419
14	7028	16886	17175	28380	29016	36956
15	7517	16165	15501	27075	24002	35597
16	6710	16175	16411	27169	27781	35407
17	6805	15835	16468	26436	27529	34326
18	6790	15671	16244	26171	27164	34045
19	7036	14328	16343	23456	27139	30143
20	6062	13693	14825	22631	24945	29199
21	6901	16093	16764	26866	28129	34849
22	6101	15175	13770	25407	21849	33272
23	7842	17809	18815	29706	31532	38625
24	8092	18733	19380	31362	32423	40989
25	6061	13433	14659	22160	24596	28561
26	6367	14596	15558	24215	26188	31374
27	5938	14774	13451	24609	21212	32127
28	5976	13008	14309	21390	23916	27487
29	5999	12732	14332	20880	23978	26839
30	7215	15961	17142	26379	28568	34098

Table B.1.4.: Measured EMP-400 instrument Inphase (I) and Quadrature (Q) values for an instrument height of 10 cm at drill sites of Qikiqtarjuaq 2017 campaign part 1.

Point ID	5 kHz		10 kHz		15 kHz	
	I [ppm]	Q [ppm]	I [ppm]	Q [ppm]	I [ppm]	Q [ppm]
31	7488	16264	17609	27004	29332	35143
32	5845	14593	13361	24481	21319	32154
33	5590	10841	13264	17535	22224	22232
34	5437	13028	12383	21590	19706	28138
35	6312	11499	12752	18559	19322	23854
36	5093	9119	11096	14344	17742	17851
37	4542	10221	10406	16570	16470	21265
38	5591	11285	13329	18241	22374	23216
39	4742	9017	10082	14295	15509	17886
40	4629	8587	10649	13188	17093	16070
41	4665	8595	9813	13638	15185	17027
42	3454	4978	9093	7549	16702	9085
43	4626	8303	9753	13069	14932	16326
44	4075	7422	8579	11510	13065	14177
45	4262	7186	8779	11173	13276	13600
46	4450	7737	9207	12058	14175	14874
47	4260	7513	9058	11622	13734	14207
48	4668	7402	10084	11366	16075	13793
49	4274	7440	8798	11553	13351	14241
50	4108	8002	8550	12557	12891	15716
51	3656	6791	7431	10584	11024	13144
52	4191	7281	8734	11270	13212	13907
53	3965	8106	8634	12587	12910	15565
54	4108	7464	8535	11593	12906	14206
55	4365	7900	8836	12413	13112	15457
56	4088	7880	8395	12406	12538	15449
57	4067	7035	8134	10936	12185	13561
58	4396	6661	9531	10051	15375	12128
59	4034	7418	8283	11517	12389	14279
60	4810	7783	10486	11878	16778	14415

Table B.1.5.: Measured EMP-400 instrument Inphase (I) and Quadrature (Q) values for an instrument height of 10 cm at drill sites of Qikiqtarjuaq 2017 campaign part 2.

Point ID	5 kHz		10 kHz		15 kHz	
	I [ppm]	Q [ppm]	I [ppm]	Q [ppm]	I [ppm]	Q [ppm]
60	4810	7783	10486	11878	16778	14415
61	3915	7354	8230	11452	12405	14185
62	4438	7626	9127	11858	13764	14641
63	4218	7035	8685	10865	13178	13383
64	3937	6760	7815	10491	11601	12952
65	4292	7368	8999	11423	13560	14006
66	4360	7554	9130	11778	13961	14475
67	3986	7223	8425	11011	12674	13495
68	4022	6952	8313	10741	12598	13200
69	3837	6689	8157	10202	12508	12383
70	3728	7938	8244	12371	12368	15438
71	4245	7242	8696	11224	13089	13868
72	4039	7024	8373	10808	12513	13247
73	3164	6881	7506	10492	11488	12639
74	3289	7315	7684	11288	11647	13805
75	3440	6438	7817	9362	11943	10989
76	3459	5832	7301	8763	11055	10458
77	3998	6738	8143	10319	12240	12516
78	3434	6750	8898	10460	14892	12479
79	3592	6295	7725	9541	11844	11431
80	3902	6490	7968	9917	11955	11974
81	3511	6163	7386	9007	11809	10603
82	3442	5742	7269	8587	10941	10181
83	3776	6219	7653	9435	11355	11429
84	3842	6360	7644	9486	11180	11409
85	3533	6321	7410	9552	11067	11612

Table B.1.6.: Measured EMP-400 instrument Inphase (I) and Quadrature (Q) values for an instrument height of 10 cm at drill sites of Qikiqtarjuaq 2017 campaign part 3.

B.2. Alert 2013

B.2.1. Drill Hole Thickness Measurements

Point ID	Latitude [°]	Longitude [°]	TT [m]
1	82.543846	-62.403996	3.80
2	82.544266	-62.403267	2.80
3	82.54377	-62.400616	2.42
4	82.543922	-62.40757	3.56
5	82.533035	-62.42292	1.91
6	82.532608	-62.422844	1.94
7	82.532158	-62.422756	1.83
8	82.532677	-62.426292	1.77
9	82.532562	-62.419498	1.89
10	82.546875	-62.549919	2.06
11	82.547234	-62.547867	1.87
12	82.547592	-62.545937	2.35
13	82.54702	-62.544876	1.70
14	82.54744	-62.550694	1.81
15	82.549416	-62.524086	3.15

Table B.2.1.: Measured total ice and snow thickness values at drill sites of Alert 2013 campaign part 1.

Point ID	Latitude [°]	Longitude [°]	TT [m]
16	82.549858	-62.524509	2.33
17	82.550301	-62.524639	3.42
18	82.547585	-62.637547	3.50
19	82.547729	-62.63406	3.52
20	82.548157	-62.635212	4.81
21	82.547852	-62.630737	3.71
22	82.54731	-62.632885	3.52
23	82.521477	-62.086605	4.06
24	82.521927	-62.086437	2.64
25	82.522354	-62.086128	2.40
26	82.521896	-62.089951	3.09
27	82.52195	-62.083042	3.38
28	82.602425	-62.362461	3.73
29	82.602867	-62.361515	2.90
30	82.603287	-62.360504	3.56
31	82.602768	-62.358109	3.55
32	82.602966	-62.364944	2.67
33	83.812569	-63.879189	2.17
34	83.813019	-63.878712	1.98
35	83.813461	-63.87812	3.45
36	83.812958	-63.874626	3.57
37	83.813057	-63.882942	2.29

Table B.2.2.: Measured total ice and snow thickness values at drill sites of Alert 2013 campaign part 2.

B.2.2. Drill Hole EMP Measurements

Point ID	4 kHz		9 kHz		15 kHz	
	I [ppm]	Q [ppm]	I [ppm]	Q [ppm]	I [ppm]	Q [ppm]
1	1294	1151	1231	1540	426	1803
2	1549	1857	2011	2690	1855	3242
3	1776	2525	2576	3769	2670	4624
4	1382	1352	1498	1825	908	2115
5	2463	3865	4159	6141	5448	7746
6	2612	3784	4176	5791	5136	7197
7	2416	3894	3894	6154	4669	7753
8	2240	3718	3590	5877	4206	7454
9	2446	4131	4069	6620	5053	8445
10	2202	3446	3705	5368	4764	6702
11	2363	3923	4013	6232	5166	7904
12	1967	2768	3036	4213	3587	5202
13	2378	4254	4152	6980	5550	9042
14	2241	3816	3717	6096	4599	7775
15	1467	1730	1731	2441	1208	2903

Table B.2.3.: Measured EMP instrument Inphase (I) and Quadrature (Q) values at drill sites of Alert 2013 campaign part 1.

Point ID	4 kHz		9 kHz		15 kHz	
	I [ppm]	Q [ppm]	I [ppm]	Q [ppm]	I [ppm]	Q [ppm]
16	1604	2304	2152	3500	1947	4367
17	1284	1435	1359	1947	609	2270
18	1277	1168	1366	1611	893	1902
19	1302	1379	1548	1903	1218	2241
20	980	683	675	864	-250	1030
21	970	760	738	1020	-60	1246
22	1232	1069	1197	1467	551	1775
23	1154	1149	1399	1443	1243	1611
24	1376	1986	2111	2857	2451	3425
25	1565	2479	2586	3680	3214	4470
26	1266	1594	1772	2135	1796	2450
27	1378	1793	2023	2500	2252	2917
28	1417	1361	1832	1763	1894	1969
29	1645	1931	2416	2721	2911	3241
30	1476	1653	2087	2288	2423	2691
31	1494	1471	1980	2001	2167	2357
32	1652	2073	2493	3002	3031	3626
33	1856	3035	2975	4732	3564	5948
34	1964	3407	3386	5389	4405	6847
35	1508	2081	2128	3072	2179	3767
36	1227	1335	1377	1821	930	2134
37	1745	2691	2765	4119	3283	5098

Table B.2.4.: Measured EMP instrument Inphase (I) and Quadrature (Q) values at drill sites of Alert 2013 campaign part 2.

B.3. Scotts Base 2011 & 2013

B.3.1. 2011 Drill Hole Thickness & EM Measurements

Point ID	Snow [cm]	Ice [cm]	SIPL [cm]	TT [cm]	I [ppt]	σ_a [mS/m]
1	30	205	43	278	5.16	151
2	34	201	10	245	5.95	157
3	33	198	9	240	6.15	169
4	33	191	15	239	6.64	161
5	39	185	33	257	5.66	167
6	42	194	50	286	4.72	147
7	35	199	54	288	5.78	152
8	30	199	41	270	6.05	154
9	29	207	37	273	5.52	161
10	32	191	49	272	6.43	157
11	35	209	100	344	-0.43	127
12	25	207	99	331	0.62	135
13	20	209	68	297	1.03	136
14	12	218	88	318	1.98	144
15	27	215	83	325	0.22	130
16	40	162	2	204	14.6	219
17	33	174	25	232	15.7	229
18	25	182	11	218	15	222
19	31	169	20	220	16.5	235
20	26	162	10	198	15.6	229
21	41	155	0	196	17.5	248
22	41	143	0	184	17.3	253
23	58	145	0	203	14.9	232
24	18	145	0	163	20.4	302
25	24	165	0	189	17.8	254
26	23	168	0	191	19.6	252
27	35	154	0	189	17.6	237
28	36	154	0	190	18.4	244
29	31	156	0	187	19.4	253
30	20	154	0	502	20.48	270

Table B.3.1.: Measured total ice and snow thickness values and EM measurements at drill sites of Scotts Base 2011 campaign part 1. Inphase outputs are as given by Geonics datalogger (EM31).

Point ID	Snow [cm]	Ice [cm]	SIPL [cm]	TT [cm]	I [ppm]	σ_a [mS/m]
31	3	224	275	490	1374	-536
32	2	222	266	470	1300	-544
33	8	223	239	502	1500	-528
34	7.5	218.5	276	523	1398	-536
35	5	223	295	615	2180	-448
36	10	223	382	640	2748	-490
37	11	231	398	692	2870	-472
38	7	225	460	656	2820	-476
39	9	222	425	610	3680	-390
40	12	229	369	698	3688	-392
41	8	227	463	659	3790	-420
42	8	219	432	699	3576	-444
43	17	226	456	677	4155	-378
44	5	226	446	696	3712	-432
45	7	227	462	700	3880	-412
46	7	241	452	698	4188	-380
47	20	233	445	673	4427	-360
48	14	236	423	620	4315	-372
49	11.5	232.5	376	633	4023	-364
50	6	239	388	605	4116	-360
51	10	237	358	446	4008	-361
52	23.5	222.5	200	423	1816	-444
53	19	218	186	430	1908	-436
54	15	224	191	405	1695	-448
55	19	212	174	437	1824	-448
56	21.5	213.5	202	164	1862	-436
57	0	164	0	161	-8191	-1212
58	14	147	0	165	-8191	-1191
59	18	147	0	168	-8191	-1141
60	19.5	148.5	0	168	-8191	-1135
61	24	144	0	165	-8191	-1128
62	19	146	0	182	-7893	-1097
63	44.5	137.5	0	178	-7106	-1044
64	51	127	0	174	-7730	-1078
65	55	119	0	187	-7296	-1048
66	41	146	0	187	-6690	-993

Table B.3.2.: Measured total ice and snow thickness values and EM measurements at drill sites of Scotts Base 2011 campaign part 2. Inphase outputs are as given by Archer data logger (EM31).

Point ID	Snow [cm]	Ice [cm]	SIPL [cm]	TT [cm]	I [ppm]	σ_a [mS/m]
67	45	142	0	546	-6976	-1022
68	9	217	320	488	1832	-464
69	9.5	228.5	250	531	2508	-384
70	10	228	293	506	2480	-392
71	6	227	273	529	1520	-424
72	16.5	224.5	288	539	2436	-368
73	5.5	229.5	304	567	2359	-436
74	20	239	308	565	3156	-350
75	9.5	239.5	316	545	2711	-390
76	6	230	309	543	2606	-421
77	13	221	309	435	2700	-376
78	6	224	205	473	1368	-460
79	8	221	244	420	1700	-432
80	7.5	220.5	192	445	1352	-468
81	10	221	214	480	1504	-480
82	29	216	235	280	2328	-382
83	23	187	70	300	-1150	-606
84	26.5	178.5	95	265	-1100	-600
85	9	192	64	290	-2208	-652
86	15	188	87	363	-1868	-660
87	18	183	162	183	-1600	-648
88	11	172	0	189	-6080	-948
89	20.5	168.5	0	186	-5820	-914
90	9.5	176.5	0	193	-6330	-968
91	18	175	0	189	-6400	-905
92	13	176	0	176	-5535	-904
93	21	155	0	172	-7668	-1020
94	18	154	0	188	-7112	-1028
95	15	173	0	180	-6965	-1020
96	23	157	0	172	-6554	-988
97	13.5	158.5	0	302	-7461	-1060
98	19.5	215.5	67	324	-392	-528
99	14	215	95	325	-948	-563
100	20.5	206.5	98	307	-584	-536
101	29.5	207.5	70	292	-112	-496
102	14	213	65	322	-916	-561

Table B.3.3.: Measured total ice and snow thickness values and EM measurements at drill sites of Scotts Base 2011 campaign part 3. Inphase outputs as given by Archer data logger (EM31).

B.3.2. 2013 Drill Hole Thickness & EM Measurements

Point ID	Ice [m]	SIPL [m]	TT [m]	I [ppm]	σ_a [mS/m]
1	2.16	0.38	2.54	-4160	170
2	2.15	0.35	2.50	-4396	175
3	2.16	0.31	2.47	-4372	174
4	2.19	0.45	2.64	-4320	173
5	2.14	0.50	2.64	-4284	173.25
6	2.01	0.86	3.09	-2360	146
7	2.23	2.39	4.62	544	128
8	2.24	2.36	4.60	606	125.75
9	2.29	2.67	4.96	663	126
10	2.28	2.39	4.67	484	130
11	2.24	2.32	4.56	452	129
12	2.28	4.20	6.48	1253	128
13	2.36	3.75	6.11	1544	120
14	2.31	4.33	6.64	1744	117
15	2.34	3.99	6.33	1444	122
16	2.37	2.62	4.99	644	118
17	2.37	2.37	4.74	672	116
18	2.34	2.07	4.41	684	116
19	2.33	2.47	4.80	772	116
20	2.37	2.60	4.97	972	111

Table B.3.4.: Measured total ice and snow thickness values and EM measurements at drill sites of Scotts Base 2011 campaign part 1. Inphase outputs as given by Archer data logger (EM31).

C. EMP Inversion RMSE Results Chapter 5

C.1. 3-Layer Model Calibration using 0.5 as weights on Q

Frequency	I_f(1.42 m) [ppm]	Q_f(1.42 m) [ppm]	$w = \frac{I_f}{Q_f}$	RMSE [m]	g for I_f
5 kHz	3094	6973	0.5	0.0716	0.68
10 kHz	6261	10850	0.5	0.0701	0.70
15 kHz	9113	13580	0.5	0.0705	0.71

Table C.1.1.: RMSE results and gain as well as weights applied for Inphase calibration of Qikiqtarjuaq 2017 data set.Weights applied on Q during Inphase calibration are ste to 0.5 for frequencies of 5 kHz ,10 kHz and 15 kHz.

C.2. 4-Layer Slush Inversion RMSE Results using Inphase and Quadrature

σ_{Slush} [mS/m]	RMSE TT [m]	RMSE Snow+Slush [m]	RMSE Ice[m]
500	0.3063	0.2987	0.3139
600	0.3125	0.3042	0.3207
700	0.3199	0.3119	0.3279
800	0.3237	0.3154	0.3320
900	0.3275	0.3209	0.3342
1000	0.3229	0.3229	0.3229
1100	0.3220	0.3220	0.3220
1200	0.3183	0.3183	0.3183
1300	0.3167	0.3167	0.3167
1400	0.3163	0.3163	0.3163
1500	0.3209	0.3209	0.3209
1600	0.3155	0.3155	0.3155
1700	0.3142	0.3142	0.3142
1800	0.3354	0.3354	0.3354
1900	0.3348	0.3348	0.3348

Table C.2.1.: RMSE results for inversions with 4-layer models with changing snow plus slush layer conductivity σ_{Slush} of Qikiqtarjuaq drill hole EM data using both I and Q. Model parameters include an instrument height of 10 cm, water conductivity of 2500 mS/m and ice conductivity of 50 mS/m at a resolution of 1 cm. The used Inphase values were calibrated using a 3 layer model with an ice plus snow conductivity of 50 mS/m as described in Chapter 5.2.2.

C.3. 5-Layer Slush Inversion RMSE Results

C.3.1. RMSE of Inversion using I & Q at 0 mS/m Snow and 50 mS/m Ice Conductivity

σ_{Slush} [mS/m]	RMSE TT [m]	RMSE Slush [m]	RMSE Snow [m]	RMSE Ice [m]
800	0.2104	0.1581	0.2146	0.2587
900	0.2054	0.1526	0.2143	0.2494
1000	0.1953	0.1451	0.2064	0.2344
1100	0.2057	0.1382	0.2276	0.2513
1200	0.1980	0.1319	0.2205	0.2416
1300	0.1923	0.1382	0.2170	0.2216
1400	0.1880	0.1331	0.2074	0.2235
1500	0.1941	0.1275	0.2250	0.2298
1600	0.1954	0.1260	0.2256	0.2346
1700	0.1855	0.1265	0.2097	0.2203
1800	0.1862	0.1188	0.2113	0.2285
1900	0.1794	0.1218	0.2118	0.2046
2000	0.1741	0.1156	0.1998	0.2069
2100	0.1915	0.1190	0.2219	0.2336
2200	0.1911	0.1152	0.2261	0.2319
2300	0.1823	0.1109	0.2159	0.2201
2400	0.1872	0.1112	0.2269	0.2236
2500	0.2013	0.1109	0.2334	0.2596

Table C.3.1.: RMSE results for inversions with 5-layer models with changing snow plus slush layer conductivity σ_{Slush} of Qikiqtarjuaq drill hole EM data using both I and Q. Model parameters include an instrument height of 10 cm, water conductivity of 2500 mS/m, ice conductivity of 50mS/m and snow conductivity of 0 mS/m at a resolution of 1 cm. The used Inphase values were calibrated using a 3 layer model with an ice plus snow conductivity of 50 mS/m as described in Chapter 5.2.2.

C.3.2. RMSE of Inversion using Q at Snow and Ice Conductivity of 50 mS/m

σ_{Slush} [mS/m]	RMSE TT [m]	RMSE Slush [m]	RMSE Snow [m]	RMSE Ice [m]
800	0.2089	0.0652	0.2803	0.2813
900	0.2142	0.0824	0.2815	0.2787
1000	0.2184	0.0748	0.2905	0.2899
1100	0.2182	0.0781	0.2907	0.2859
1200	0.2094	0.0698	0.2788	0.2797
1300	0.2285	0.0851	0.2972	0.3031
1400	0.2281	0.0758	0.3007	0.3078
1500	0.2277	0.0827	0.2920	0.3084
1600	0.2132	0.0807	0.2744	0.2846
1700	0.2169	0.0873	0.2764	0.2870
1800	0.2210	0.0693	0.2903	0.3034
1900	0.2184	0.0772	0.2803	0.2978
2000	0.2185	0.0800	0.2782	0.2973

Table C.3.2.: RMSE results for inversions with 5-layer models with changing snow plus slush layer conductivity σ_{Slush} of Qikiqtarjuaq drill hole EM data using only Q. Model parameters include an instrument height of 10 cm, water conductivity of 2500 mS/m and ice and snow conductivity of 50 mS/m at a resolution of 2 cm. The used Inphase values were calibrated using a 3 layer model with an ice plus snow conductivity of 50 mS/m as described in Chapter 5.2.2.

C.3.3. RMSE of Inversion using I & Q at Snow and Ice Conductivity of 50 mS/m

σ_{Slush} [mS/m]	RMSE TT [m]	RMSE Slush [m]	RMSE Snow [m]	RMSE Ice [m]
800	0.2034	0.1434	0.2221	0.2446
900	0.2161	0.1422	0.2456	0.2606
1000	0.2229	0.1341	0.2564	0.2783
1100	0.2274	0.1294	0.2697	0.2830
1200	0.2051	0.1232	0.2432	0.2489
1300	0.2239	0.1248	0.2635	0.2835
1400	0.2240	0.1212	0.2674	0.2835
1500	0.2197	0.1259	0.2546	0.2784
1600	0.2157	0.1270	0.2566	0.2635
1700	0.2175	0.1216	0.2600	0.2710
1800	0.2256	0.1185	0.2699	0.2883
1900	0.2173	0.1153	0.2625	0.2741
2000	0.2201	0.1102	0.2641	0.2859

Table C.3.3.: RMSE results for inversions with 5-layer models with changing snow plus slush layer conductivity σ_{Slush} of Qikiqtarjuaq drill hole EM data using both I & Q. Model parameters include an instrument height of 10 cm, water conductivity of 2500 mS/m and ice and snow conductivity of 50 mS/m at a resolution of 2 cm. The used Inphase values were calibrated using a 3 layer model with an ice plus snow conductivity of 50 mS/m as described in Chapter 5.2.2.

C.3.4. RMSE of Inversion using Q at Snow and Ice Conductivity of 0 mS/m

σ_{Slush} [mS/m]	RMSE TT [m]	RMSE Slush [m]	RMSE Snow [m]	RMSE Ice [m]
800	0.1839	0.0749	0.2564	0.2204
900	0.1936	0.0725	0.2743	0.2338
1000	0.1978	0.0800	0.2694	0.2440
1100	0.2069	0.0684	0.2899	0.2625
1200	0.1990	0.0830	0.2726	0.2414
1300	0.2013	0.0776	0.2725	0.2538
1400	0.1919	0.0741	0.2624	0.2394
1500	0.2060	0.0754	0.2896	0.2531
1600	0.2061	0.0765	0.2820	0.2598
1700	0.2011	0.0745	0.2817	0.2472
1800	0.1955	0.0704	0.2749	0.2413
1900	0.2003	0.0717	0.2790	0.2501
2000	0.2065	0.0731	0.2879	0.2587

Table C.3.4.: RMSE results for inversions with 5-layer models with changing snow plus slush layer conductivity σ_{Slush} of Qikiqtarjuaq drill hole EM data using only Q. Model parameters include an instrument height of 10 cm, water conductivity of 2500 mS/m and ice and snow conductivity of 0 mS/m at a resolution of 2 cm. The used Inphase values were calibrated using a 3 layer model with an ice plus snow conductivity of 50 mS/m as described in Chapter 5.2.2.

C.3.5. RMSE of Inversion using I & Q at Snow and Ice Conductivity of 0 mS/m

σ_{Slush} [mS/m]	RMSE TT [m]	RMSE Slush [m]	RMSE Snow [m]	RMSE Ice [m]
800	0.3277	0.3325	0.1830	0.4677
900	0.3567	0.3303	0.1777	0.5620
1000	0.3815	0.3278	0.1706	0.6462
1100	0.3973	0.3224	0.1568	0.7128
1200	0.4044	0.3126	0.1425	0.7582
1300	0.4036	0.3038	0.1259	0.7811
1400	0.4062	0.2918	0.1224	0.8044
1500	0.4031	0.2794	0.1156	0.8144
1600	0.4002	0.2701	0.1029	0.8274
1700	0.3985	0.2602	0.1003	0.8350
1800	0.3992	0.2519	0.0959	0.8498
1900	0.4009	0.2448	0.0959	0.8620
2000	0.3981	0.2397	0.0866	0.8679

Table C.3.5.: RMSE results for inversions with 5-layer models with changing snow plus slush layer conductivity σ_{Slush} of Qikiqtarjuaq drill hole EM data using both I & Q. Model parameters include an instrument height of 10 cm, water conductivity of 2500 mS/m and ice and snow conductivity of 0 mS/m at a resolution of 2 cm. The used Inphase values were calibrated using a 3 layer model with an ice plus snow conductivity of 50 mS/m as described in Chapter 5.2.2.